Using Monte-Carlo Simulations to Determine Nuclear-Weapon Related Passive Radiation Signatures and Their Uniqueness in Verification

Von der Fakultät für Mathematik, Informatik und Naturwissenschaften der RWTH Aachen University zur Erlangung des akademischen Grades eines Doktors der Naturwissenschaften genehmigte Dissertation

vorgelegt von

M.Sc.
Christopher Fichtlscherer
aus
Freiburg im Breisgau

Berichter:	Universitätsprofessor Dr. rer. nat. Malte Göttsche Universitätsprofessor Dr. rer. nat. Achim Stahl
Tag der mündlichen Prüfung:	26.08.2025

Diese Dissertation ist auf den Internetseiten der Universitätsbibliothek online verfügbar.

Eidesstattliche Erklärung

Declaration of Academic Integrity

Christopher Fichtlscherer

erklärt hiermit, dass diese Dissertation und die darin dargelegten Inhalte die eigenen sind und selbstständig, als Ergebnis der eigenen originären Forschung, generiert wurden.

Hiermit erkläre ich an Eides statt

1. Diese Arbeit wurde vollständig oder größtenteils in der Phase als Doktorand dieser Fakultät und Universität angefertigt;

2. Sofern irgendein Bestandteil dieser Dissertation zuvor für einen akademischen Abschluss oder eine andere Qualifikation an dieser oder einer anderen Institution verwendet wurde, wurde dies klar angezeigt;

3. Wenn immer andere eigene- oder Veröffentlichungen Dritter herangezogen wurden, wurden diese klar benannt;

4. Wenn aus anderen eigenen- oder Veröffentlichungen Dritter zitiert wurde, wurde stets die Quelle hierfür angegeben. Diese Dissertation ist vollständig meine eigene Arbeit, mit der Ausnahme solcher Zitate;

5. Alle wesentlichen Quellen von Unterstützung wurden benannt;

6. Wenn immer ein Teil dieser Dissertation auf der Zusammenarbeit mit anderen basiert, wurde von mir klar gekennzeichnet, was von anderen und was von mir selbst erarbeitet wurde;

7. Ein Teil oder Teile dieser Arbeit wurden zuvor veröffentlicht und zwar in:

   C. Fichtlscherer et al. “Modeling gamma detectors in OpenMC: Validation of a newly implemented pulse-height tally”. In: *Progress in Nuclear Energy* 172 (2024). DOI: 10.1016/j.pnucene.2024.105186

C. Fichtlscherer, M. Kütt. "Uniqueness, Reproducibility and Discrimination of Nuclear Warhead Gamma Signatures". In: *Science & Global Security* 32.1–3 (2024). DOI: 10.1080/08929882.2024.2387966

C. Fichtlscherer, M. Göttsche, M. Kütt. "Can We Fake Gamma Emissions of Nuclear Warheads? An Exploratory Study". In: *Institute of Nuclear Materials Management (INMM) and European Safeguards Research and Development Association (ESARDA) Joint Annual Meeting*. 2021. URL: https://resources.inmm.org/sites/default/files/2021-09/a337.pdf (visited on 02/25/2025)

M. Kütt, J. Elfes, **C. Fichtlscherer**. "Fetter Model Revisited: Detecting Nuclear Weapons 30 Years Later". In: *Institute of Nuclear Materials Management (INMM) and European Safeguards Research and Development Association (ESARDA) Joint Annual Meeting*. 2021. URL: https://resources.inmm.org/sites/default/files/2021-09/a215.pdf (visited on 02/25/2025)

C. Fichtlscherer et al. "Implementation and Validation of the Pulse-Height Tally in OpenMC". in: *Institute of Nuclear Materials Management (INMM) and European Safeguards Research and Development Association (ESARDA) Joint Annual Meeting*. 2021. URL: https://resources.inmm.org/sites/default/files/2021-09/a267.pdf (visited on 02/25/2025)

M. Kütt, **C. Fichtlscherer**. "Hoax or Real? On the Uniqueness of Nuclear Radiation Signatures". In: *Alva Myrdal Centre for Nuclear Disarmament (AMC) Annual Conference*. 2022

C. Fichtlscherer, M. Kütt. "Improving Warhead Authentication using Gamma Spectroscopy". In: *65th Annual Meeting of the Institute of Nuclear Materials Management (INMM)*. 2024. URL: https://cdn.fourwaves.com/static/media/formdata/b12613f9-28b7-4568-a069-5c7cfeff3c8e/21b15233-1c7f-4a44-a2e5-bf980042b9e5.pdf (visited on 02/25/2025)

C. Fichtlscherer, M. Kütt. "On the Uniqueness of Nuclear Warhead Signatures". In: *65th Annual Meeting of the Institute of Nuclear Materials Management (INMM)*. 2024. URL: https://cdn.fourwaves.com/static/media/formdata/b12613f9-28b7-4568-a069-5c7cfeff3c8e/ed30cb5f-3b30-4f83-a82c-d252987db431.pdf (visited on 02/25/2025)

C. Fichtlscherer et al. "Modeling Spontaneous Fission-Driven Isotopic Change in Subcritical Nuclear Systems". In: *66th Annual Meeting of the Institute of Nuclear Materials Management (INMM) (Submitted)*. 2025

April 22, 2025

Christopher Fichtlscherer

Abstract

Systems designed to confirm the authenticity of a nuclear warhead could play a crucial role in verifying international disarmament processes. Although never deployed, various confirmation systems have been developed for potential future verification procedures. Most of these systems rely on measuring the warhead's passive photon and/or neutron emissions under inspection.

In a treaty context, the measured emissions serve as signatures. Inspectors use these signatures to verify the authenticity of the object under inspection or to identify potential attempts at fraud. For signatures to be effectively used, they must enable inspectors to confirm authentic warheads and distinguish them from hoax objects reliably. However, the reliability of such signatures has been repeatedly questioned.

This work analyzes the reliability of radiation signatures of four warhead confirmation systems, focusing on their ability to confirm actual warheads and their vulnerability to be imitated by hoax objects. To do so, I introduce eight different theoretical emission models. My results demonstrate that these signatures often fail to confirm the authenticity of warheads of different ages. Further, I show that four different types of hoax objects, in many cases, can successfully mimic the signature of the emission model.

Two of the analyzed systems utilize a low-resolution gamma spectroscopy approach to ensure that no confidential information is revealed during the measurement. Even though they assure privacy, the signatures produced by these systems are particularly vulnerable to hoaxes that use optimized combinations of photon-emitting nuclides. I developed a genetic algorithm to determine more reliable low-resolution gamma spectroscopy bin structures. The optimized bin structure confirms warheads of different ages while detecting hoax objects from optimized combinations of photon-emitting nuclides.

To conduct this analysis, I have developed multiple computational tools. One is a validated pulse-height tally for OpenMC; another is a decay tool that accounts for attenuating fission chains induced by spontaneous fission in subcritical systems with non-negligible criticality.

This page intentionally blank

Acknowledgements

During my dissertation, I had the honor of working with two outstanding research groups — the Nuclear Verification and Disarmament Group at RWTH Aachen and the Arms Control and Emerging Technologies project at the Institute for Peace Research and Security Policy at the University of Hamburg (IFSH). I am deeply grateful for the stimulating environment that fostered countless enriching discussions — and of course, for the lunch and coffee breaks.

I express my heartfelt gratitude to my supervisor at IFSH, Dr. Moritz Kütt, who introduced me to the field of scientific peace research long before I began my dissertation. His visionary approach in developing this research project, along with his meticulous guidance kept me on track while he always remained open to new ideas. I have been profoundly impressed by his unwavering moral and academic standards, and I cannot even describe how much I learned under his mentorship. Taking the journey of my dissertation under his mentorship was a profound privilege. I am proud of the professional relationship we have developed during the past years — a bond robust enough to embrace and overcome differences of opinion.

I also thank my supervisor at RWTH Aachen, Prof. Dr. Malte Göttsche. Your valuable feedback and insightful perspective on my work were instrumental in organizing my thoughts and inspiring innovative approaches. I am also grateful to my second supervisor at RWTH Aachen, Prof. Dr. Achim Stahl, whose profound understanding of physics has been both impressive and inspiring.

While working on my dissertation, I spent seven months at the Department of Nuclear Science and Engineering at the Massachusetts Institute of Technology, under the supervision of Prof. Dr. Scott Kemp, to whom I am incredibly grateful for everything he has taught me. This period was immensely formative, offering the opportunity to work with a diverse group of inspiring and supportive colleagues. I am incredibly thankful to my office mate, Lucas, whose insightful discussions on physics enriched my experience significantly. Further, I want to thank Dr. David Wright and Dr. Lisbeth Gronlund. In the past, I benefited enormously from being invited twice to the International Summer School on Science and World Affairs that they organized. Having the opportunity to see and engage with them regularly at MIT was truly wonderful. Additionally, they are among the most hospitable individuals I have ever

had the pleasure of knowing.

I thank the Center for Strategic and International Studies for inviting me to a workshop on Warhead Verification Negotiations in Washington. I also thank the U.S. Department of Energy's National Nuclear Security Administration for inviting me to the Nevada National Security Site for a transparency demonstration.

I feel privileged to have collaborated with Prof. Dr. Frank von Hippel, whose dedication, patience, and kindness have been a role model throughout my academic endeavors. I was also thrilled to collaborate with Prof. Dr. Julien de Troullioud de Lanversin, an exceptionally bright and creative scientist and, moreover, one of my closest friends. We got to know each other on a squash court; however, given Julien's ambition, playing squash together over the years proved very frustrating for me and rather boring for him. What endures is our friendship: Julien is someone with whom I can discuss all my doubts and problems, and his advice is immensely valuable to me.

I want to acknowledge the OpenMC developer team for their support and guidance, with special thanks to Gavin Ridley and Paul Romano for their advice on implementing key features, particularly the pulse-height tally.

My gratitude extends to Prof. Dr. Götz Neuneck, Dr. Matthias Englert, and Dr. Alexander Graef for their motivation and the many thought-provoking discussions, as well as my good friend Robert Wenzl, who has helped me so often with his great understanding of texts, words, and language. I met Niklas Heim on my first day of studying physics; despite the many years that have passed, he still always listens to my code ideas and provides valuable feedback. I also thank Cécile Huber for the many hours spent together in the Freiburg library during the final stages of this work.

I thank Milon Miah for helping validate the pulse-height tally, and Lukas Rademacher for discussing compiler errors. I thank especially the "physics" subgroup in Arms Control and Emerging Technologies at IFSH: Dr. Timur Kadyshev for exciting discussions on missiles, Zahra Bagheri and Alexandra Datz for discussing simulations, Annika Simon for helping me to research cheating attempts in past verification processes, and Emma Lucke for working on the next steps in my research project.

I am thankful to Dr. Olaf Schuman, Benjamin Jung, Max Schalz, Dr. Friederike Frieß, Franziska Stärk, and Dr. Sophie Kretzschmar, who spent a lot of time reviewing drafts of my dissertation and provided valuable feedback. I would also like to thank the project coordinator, Marten Ennen, at IFSH for helping me navigate various organizational challenges throughout my research.

I am a member of FONAS ("Forschungsverbund Naturwissenschaft, Abrüstung und internationale Sicherheit") and the working group Physics and Disarmament of the German Physical Society, I enjoy discussing ideas, learning, and getting inspired at their annual meetings.

This work was initially financed by an Exposé-stipend and then a full German Academic Scholarship Foundation doctoral scholarship. In addition, my position at the IFSH was financed by the research project "Nuclear Warhead Authentication Based on Gamma and Neutron Emissions — How to Discourage Cheating?" by the German Foundation for Peace Research. I am incredibly grateful to both of these foundations for giving me the opportunity and freedom to work intensively on this research topic.

Simulations were performed using computing resources granted by RWTH Aachen University, Germany, under project rwth0572; and a server at IFSH.

Finally, I offer my deepest thanks to my parents, whose unwavering support allowed me to pursue my interests confidently. They taught me the need to be committed to one's ideals and the value of seeking out and following what inspires you. A special word of thanks goes to my sister, Anna, who shaped me just as my parents did and is my lifelong best friend I can always count on. I thank Antonia for sharing our lives and everything in between; I could not imagine a better way to start my day than enjoying a morning coffee with you, nor a better way to end it than by reflecting on our day together.

This page intentionally blank

Contents

Eidesstattliche Erklärung Declaration of Academic Integrity i
Abstract iii
Acknowledgements v
List of Figures xii
List of Tables xiii

1 Introduction 1

2 Passive Radiation Signatures in Nuclear Verification 5
2.1 Nuclear Verification and Warhead Confirmation 5

3 Nuclear Verification Physics 13
3.1 Radioactive Decay and Nuclear Emissions 13
3.2 Warhead Confirmation Systems 19
3.3 Monte Carlo Particle Transport Codes 23

4 Development and Validation of Simulation Tools 27
4.1 Material Depletion Module 27
4.2 Pulse-Height Tally Functionality in OpenMC 31

5 Defining Weapon Baseline Emissions 45
5.1 Nuclear Weapon Materials and Components 45
5.1.1 Fissile Material of the Primary — Plutonium 45
5.1.2 Uranium Components 49
5.1.3 Reflector, Tamper and Pusher 50
5.1.4 Chemical Explosives 51
5.1.5 Deuterium-Tritium Boosting 52
5.1.6 Second Stage 53
5.1.7 Reentry Vehicle 54
5.2 Photon Emissions and Shielding Factors 55
5.3 Baseline Signatures of Nuclear Weapons 58

5.3.1 Fissile Material Models 58
5.3.2 Three Notional Weapon Models 60

6 Vulnerabilities of Weapon Signatures 71
6.1 Nuclear Signatures of Warheads 71
6.2 Completeness of the Nuclear Signatures 73
6.3 Soundness of the Nuclear Signatures 74
6.3.1 Replacing the Warhead with Radioactive Nuclides 76
6.3.2 Replacing Plutonium with an (α, n)-(n, γ)-Source 81
6.3.3 Substituting Weapon-Grade with Reactor-Grade Plutonium . . . 83
6.3.4 Replacing Parts of the Plutonium with Californium-252 85
6.4 Overview of Cheating Possibilities 88

7 Adapting Measurement Systems 91
7.1 Optimizing Bin Structures 91
7.1.1 Using a Genetic Algorithm to Find Improved Bin Structures . . . 94
7.2 Potential Treaty Implementation and Information Content 103

8 Conclusion and Outlook 107

Bibliography 110

List of Figures

2.1 Passive Gamma Spectrum of the Soviet SS-N-12 8
2.2 Declassified Hoaxes of Field Test 34 and a French Weapon Design 10

3.1 Binding Energy Curve 15
3.2 Detection Process in a Scintillation Detector 20
3.3 Warhead Confirmation Systems 23

4.1 Illustrative Particle Histories for the Pulse-Height Tally 32
4.2 Two-Region Detector for Analytical Pulse-Height Tally Validation 34
4.3 Comparison of OpenMC-simulated and Analytical PHT Results 36
4.4 Model of the "802 Scintillation Detector" by Mirion Technology 37
4.5 Pulse-Height Tally Results in OpenMC and MCNP for a Caesium-137 Source 38
4.6 Comprehensive Pulse-Height Tally Comparisons in OpenMC and MCNP 39
4.7 Determination of the Detector Resolution 41
4.8 Comparison of Experimental and Simulated Gamma Spectra 42

5.1 Prompt Criticality of a Bare Plutonium Sphere 49
5.2 Photon Absorption Fractions for Warhead-Related Materials 57
5.3 Photon Emission Spectra of Plutonium Pits 59
5.4 Photon and Neutron Emission Spectra of the BeRP Ball 60
5.5 Theoretical Warhead Emission Models 61
5.6 Photon and Neutron Emissions of the FPS Model 62
5.7 Photon and Neutron Emissions of the W78-RV Model 63
5.8 Photon and Neutron Emissions of the W87-RV Model 64

6.1 Detector Response Function 2x2 Inch NaI Scintillation Detector 72
6.2 Confirming the Pit and the W78-RV Model in IBX, IBX II, and TRIS . . . 74
6.3 Photon Emission Rates and Half-Life of all Photon-Emitting Nuclide States 77
6.4 Nuclide Hoax of a 30-year-old W87-RV Warhead 79
6.5 Simulated Template Measurements for Nuclide Hoaxes 81
6.6 Neutron Energy Spectra: WGPu Spontaneous Fission, (α, n)-Source 83
6.7 Photon and Neutron Emissions of RGPu in the W78-RV 85

6.8 Neutron Emissions and Gamma Spectrum of a Californium-252 Hoax . . 86
6.9 MCTM-Measured Spectrum of a Californium-252 Hoax 87

7.1 Best Hoax Chi-Square-Test Results vs. Energy Bins 93
7.2 Non-Completeness of Gamma Signatures with Increased Resolution . . . 94
7.3 Structure of the Genetic Algorithm for Bin Structure Optimization 99
7.4 Fitness Trajectories Across Generations 100
7.5 Exemplary Found Bin Structures 101
7.6 Stability Analysis for the W87-RV New Bin Structure 103

List of Tables

3.1 Relevant Nuclides Watt Parameters and Multiplicities 17
3.2 Energy Bin Structures of IBX II and TRIS 22

4.1 Analytic Determined Pulse-Height Tally Results for Validation 35

5.1 Plutonium Isotopes Photon- and Neutron Production Rates 47
5.2 WGPu's Composition, Photon- and Neutron Production Rates 48
5.3 Uranium Isotopes Photon- and Neutron Production Rates 50
5.4 Uranium's Photon- and Neutron Production Rates 50
5.5 Nuclear Weapon Related Photon Decay Emission 56
5.6 Nuclear Weapon Related Neutron Capture Photon Emission 56
5.7 Comparison of the BeRP Ball's Composition in the Literature 60
5.8 Overview of Model's Photon and Neutron Emissions 65

6.1 Chi-Square Values for Removing Specific Nuclides 80
6.2 RGPu's Composition, Photon- and Neutron Production Rates 84
6.3 Total Neutron and Photon Emissions of Modified BeRP Ball 88
6.4 Summary of Cheating Vulnerabilities 89

This page intentionally blank

Chapter 1

Introduction

The dismantlement of every U.S. nuclear weapon begins with an administrative decision: The U.S. Department of Energy authorizes its retirement. Then it is transported to the Pantex Plant in Texas — the United States' sole facility for nuclear weapons assembly and disassembly. Within 72 hours of arrival, each warhead undergoes technical safeguards inspections through gamma spectroscopy and/or neutron detection conducted by the Safeguard Confirmation Measurement Section [10]. Next, the warhead is disassembled into thousands of individual parts and components — a process that, depending on the warhead type, takes between 5 and 21 days [11]. The plutonium pits are housed in AL-R8 steel containers, cushioned with Celotex packing material, and stored in earth-covered concrete bunkers within Zone 4 — the most heavily guarded area of Pantex [12, 13]. Although initially conceived as a temporary solution, this storage method has persisted due to ongoing challenges in long-term plutonium disposition [14]. Other components are sent to specialized facilities for further processing: uranium parts and lithium deuteride are dismantled at the Y-12 National Security Complex in Tennessee [15], while tritium is recycled at the Savannah River Site in South Carolina [16].
Thus, between 1989 and 2023, 18,970 nuclear warheads were dismantled in the US [10, 17]. These massive reductions in U.S. and Union of Soviet Socialist Republics (USSR) nuclear weapon stocks were made possible by a series of arms-control treaties that emerged in response to the threat of nuclear weapons, including the Strategic Arms Limitation Talks (SALT) and the Strategic Arms Reduction Treaties (START), which built on improved U.S.-Soviet relations starting in the mid-1980s.
Verification procedures, often based on technical measurements, have been established to increase mutual trust and assure compliance with such treaties. However, while previous treaties primarily regulated the number of deployed warheads and confirmed their transition to a non-deployed status by verifying the dismantlement of their delivery systems, such as aircraft or missiles, achieving Global Zero — a world without nuclear weapons, as envisioned by the Treaty on the Prohibition of Nuclear Weapons (TPNW) — requires the complete dismantlement of the warheads. The confirmation of the nuclear warhead — assuring that the object to be dismantled is an actual nuclear warhead — is an essential step. It is often suggested

that warhead confirmation be based on measuring passive photon and neutron emissions. In the verification context, these measurement results are considered the warhead's signature. In the past, various systems have been proposed to confirm nuclear warheads based on their passive radiation signatures, with a primary focus on preventing the leakage of confidential information during the confirmation process (e.g. [18–21]).

This thesis centers around the robustness of passive radiation signatures in nuclear warhead confirmation by addressing concerns that have been raised in the literature multiple times:

1. As the radioactive material in the warhead decays with time, the nuclear warhead's signature changes [22]. Will this lead to false negatives in the verification procedure?

2. To confirm warheads based on their passive radiation signature, the signature must be unique, which is still an open question [10, 23]. Otherwise, a malicious actor could cheat a disarmament process by presenting hoax objects instead of actual warheads.

3. Are there improved signatures that overcome these vulnerabilities?

In **Chapter 2**, I present a political perspective on nuclear disarmament verification, focusing on warhead confirmation. I examine the role of signatures and their uniqueness, analyzing past disarmament treaties and notable cases of espionage. Additionally, I provide insight into the Black Sea Experiment, a joint US-Russian series of measurements that included the only publicly available passive gamma spectrum of a nuclear weapon, and the Field Test 34, a U.S. nuclear verification exercise in which inspectors were deliberately misled using hoax objects.
In **Chapter 3**, I introduce the needed physical background, covering the liquid-drop model, radioactive decays, and scintillation detectors. I describe the four proposed warhead confirmation systems studied in this work: the Information Barrier eXperimental (IBX), the Information Barrier eXperimental II (IBX II), the Trusted Radiation Identification System (TRIS), and the Multi-Criteria Template-Matching (MCTM) approach [18–21]. Additionally, I introduce the concept of Monte Carlo particle transport codes using OpenMC as an example, which is employed to conduct all simulations in this work.
In **Chapter 4**, I describe the implementation and validation of my open-source code contributions required to analyze the passive gamma radiation signatures of nuclear warheads. These contributions include a tool to determine the compositional change of subcritical systems with non-negligible criticality, such as nuclear warheads; a tool for calculating photon, and neutron emissions from arbitrary material compositions using data from the Evaluated Nuclear Structure Data Files (ENSDF); and a pulse-height tally for OpenMC, enabling the determination of gamma detector responses.
In **Chapter 5**, I describe the key components and materials of nuclear warheads and introduce eight theoretical warhead emission models that serve as baselines. These models include a point source of weapons-grade plutonium, a weapons-grade plutonium pit, and the Beryllium Reflected Plutonium (BeRP) ball [24]. Additionally, I examine a single-stage nuclear warhead

model based on the Black Sea Experiment [25]. Building on extensive research of publicly available sources, I developed theoretical emission models for the U.S. W78 warhead, including the Mk12-A reentry vehicle, and the W87 warhead, including the Mk21 reentry vehicle.
In **Chapter 6**, I describe how nuclear signatures of the introduced weapon emission models emerge from measurements performed with the considered confirmation systems. I evaluate the completeness of these signatures — their ability to confirm authentic warheads — by assessing the systems' capability to verify warheads of varying ages using a template-based approach. Finally, adopting a red-teaming strategy, I examine the soundness of the signatures — their robustness against hoax objects — by analyzing the uniqueness of the signatures when confronted with four types of hoax objects.
In **Chapter 7**, I address the determined vulnerabilities of existing signatures. Using a genetic algorithm, I optimize complete and sound weighted low-resolution bin structures for warhead confirmation, which could be implemented in existing hardware to verify future disarmament treaties.
In **Chapter 8**, I summarize the key findings of this work and provide an outlook on potential directions for future research.

This page intentionally blank

Chapter 2

Passive Radiation Signatures in Nuclear Verification

This chapter explores the political and technical tensions between nuclear verification and nuclear secrecy. The core concepts behind warhead confirmation and important treaties reducing the number of warheads in the past are described. Further, I provide brief insights into the Black Sea Experiment and the Field Test 34.

2.1 Nuclear Verification and Warhead Confirmation

In June 1945, several scientists from the Manhattan Project, including James Franck, Leo Szilard, and Glenn T. Seaborg, realized that "*the development of nuclear power is fraught with infinitely greater dangers than were all the inventions of the past.*" In the so-called Franck Report sent to the U.S. Secretary of War, they advocated for an "*obligation of restraint*" on the use of nuclear weapons [28]. Further, they concluded that "*no paper agreement can be sufficient since neither this or any other nation can stake its whole existence on trust in other nations' signatures*" and thus "*any international agreement on prevention of nuclear armaments must be backed by actual and efficient controls*" — a call for verification only a month before the first-ever nuclear weapon explosion during the Trinity Test [28]. Another month later, the US dropped a device over Hiroshima — called Little Boy — that shot a projectile of highly enriched uranium into a target mass, resulting in a fast nuclear chain reaction in the so-assembled 64 kg of uranium that produced a yield of about 14 kt(TNT). In the face of these grim wartime realities, the scientists' dream of an agreement on the non-use of nuclear weapons in warfare remained unfulfilled. Yet, the principle they advocated — actual and efficient controls (verification) — would become central to the landscape of nuclear arms control and disarmament treaties in the decades to come.[1]

Nuclear Verification and Secrecy

Verification — following Alan Krass, "*can be taken to be the action of demonstrating compliance with treaty obligations by means of evidence or information gathered by a variety of technical and institutional means*" and has "*two fundamental purposes: to deter violations by posing a credible threat of discovery and to build confidence in a treaty by demonstrating compliance*" [29].

But another principle was central from the beginning: nuclear secrecy. Six years after the bombing of Hiroshima and Nagasaki, the U.S. government underscored its absolute determination to maintain this principle: "*It was a queer, sultry summer, the summer they electrocuted the Rosenbergs, and I didn't know what I was doing in New York*" writes Sylvia Plath in her novel The Bell Jar [30]. Julius and Ethel Rosenberg were convicted of passing nuclear secrets to the USSR and remain the only American civilians executed for espionage during the Cold War — requests for a presidential pardon were explicitly rejected.
Nuclear secrecy is motivated by the prevention of nuclear proliferation and the maintenance of a strategic advantage: Information on technical or engineering details regarding nuclear weapons could help a proliferator's weapons program substantially, for example, by sparing time and money and maybe by decreasing the likelihood of detection before the program reaches completion.[2] But, detailed information on nuclear weapons could also expose technological vulnerabilities that weaken a state's second-strike capabilities, erode technological superiority, and undermine a state's strategic ambiguity about intentions and capabilities [31].

The fundamental conflict between verification, which depends on transparency, and nuclear secrecy, which demands strict confidentiality, presents a persistent challenge in nuclear arms control and disarmament verification.

Verification of Past Treaties

As a result, only one treaty relating the disarmament of nuclear weapons incorporated direct warhead measurements for verification — and only for a very specific case. The Intermediate-Range Nuclear Forces (INF) Treaty, signed in 1987 between the US and the USSR, banned all land-based nuclear missiles ranging from 500 to 5,500 km. At the time, the Soviet arsenal included both the SS-20 (banned under the INF treaty) and SS-25 (not covered under the treaty's provisions) missile systems. The primary optical distinction between these missiles was the length of their second stage: 2.87 m for the SS-20 and 3.07 m for the SS-25 [32]. To verify compliance, technical discussions in 1988 led to the decision to use a helium-3 neutron count-rate detector, enabling inspectors to differentiate between the three warheads atop the SS-20 and the single warhead on the SS-25 [33]. These neutron measurements during inspections ended in 1996 (the last SS-20 was destroyed in 1991) [34].
In all the other treaties — including the Strategic Arms Limitation Talks (SALT I and II in 1972 and 1979), the Anti-Ballistic Missile Treaty (ABM) in 1972, the Strategic Arms Reduction

Treaties (START I in 1991 and START II in 1993), the Strategic Offensive Reductions Treaty (SORT) in 2002, and New START in 2011 — verification measurements were not performed on actual warheads.[3]

The START treaties focused solely on reducing the number of deployed warheads, and their number was verified through their delivery vehicles. However, even though the treaties did not address non-deployed warheads, they progressively lowered the nuclear arsenals of the US and the USSR/Russia. The agreed warhead limits were 6,000 under START I, 3,000–3,500 under START II, 1,700–2,200 under SORT, and 1,550 under New START [35]. Meanwhile, START III, which aimed to reduce deployed warheads further to 2,000–2,500 by 1997, was never ratified. Russian officials stated during the START III negotiations that they would consider going down to 1,500 strategic nuclear warheads [36]. Experts suggest that as warhead numbers decrease to certain levels — possibly below 1,000 — a more thorough warhead-based verification method — *warhead confirmation* — will become necessary [37]. This implies that, for future arms control and disarmament treaties, it may be beneficial — or even essential — to verify that an object claimed by the host to be a nuclear warhead and being designated for dismantlement is indeed a nuclear warhead. This would ensure compliance and prevent a malicious actor from circumventing the treaty by falsely claiming to dismantle nuclear weapons while secretly retaining them.

Nuclear Signatures

In 1989, Theodore B. Taylor proposed four different measurements for warhead confirmation: total weight measurements, isotopic composition measurements, passive radiation scanning analysis, and external neutron source for fission detection [38]. Already one year later, some of these measurements were performed during the Black Sea Experiment. The Black Sea Experiment was a joint U.S.-Soviet verification exercise, that built on the intensive verification cooperation between Soviet and American research institutions in the late 1980s. Soviet and U.S. scientists conducted several measurements aboard the Soviet cruiser Slava, anchored off Yalta, which was equipped with a single SS-N-12 submarine-launched cruise missile (SLCM).[4] Among other measurements, American scientists used a liquid nitrogen-cooled high-purity germanium detector placed on the missile launch tube to measure the high-resolution gamma spectrum of the weapon [207]. The spectrum was recorded during a 24 minute measurement between 30 and 2,670 keV with a resolution of 2 keV.[5] The measured spectrum, shown in Figure 2.1, is the only ever published gamma emission spectrum of an operational nuclear weapon.

In an agreement or a treaty, the measurement result — for example, the warhead's gamma spectrum — is considered a *signature*.[6] The signature depends on the type of measurement and the object under inspection. To reliably confirm warheads based on these signatures, the signature must allow to correctly accepting authentic warheads (*completeness*), reject hoax objects (*soundness*), and not reveal secret information (*privacy*) [40]. Today's most discussed signatures for warhead confirmation are photon and neutron emission signatures that arise

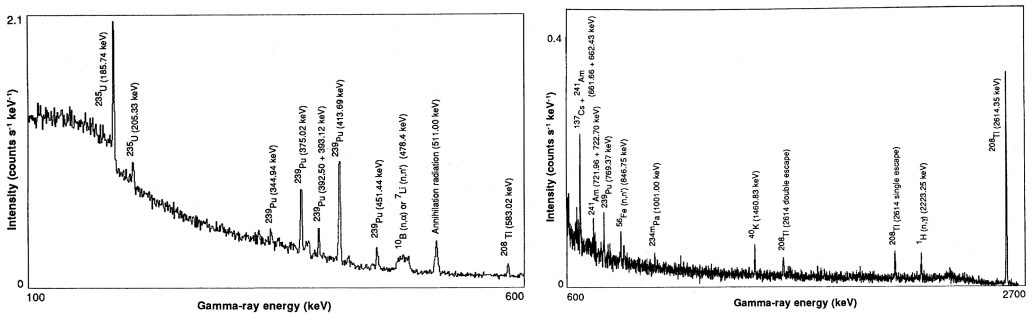

Figure 2.1: Passive Gamma Spectrum of the Soviet SS-N-12
The result of the 24 min HPGe measurement of the Soviet SS-N-12 SLCM. This Figure is copied from the original article from 1990 [39]. From the thallium-232 (a decay product of uranium-232) gamma peak, it can be determined that warhead components were made from uranium that was irradiated in a reactor before, as uranium-232 is not contained in natural uranium — a fact that was classified by the USSR [39].

from the natural decay of fissile materials (passive measurements) or are induced by external irradiation sources (active measurements). For warhead confirmation, the signature must either fulfill specific criteria (*attribute approach*) or be compared against the signatures of an object of assured authenticity, called *golden sample*, in a *template approach*.[7] The latter comes with the advantage that no specific knowledge of the warhead is needed and is typically seen as more resistant to cheating compared to the attribute method [41].

Already in his 1989 publication, Theodore B. Taylor questioned the completeness of the signatures: "*passive radiation scanning is not likely to produce a reliable fingerprint. The external fluxes of γ-rays or spontaneous fission neutrons from warheads of the same type but with uranium or plutonium of differing isotopic compositions show credible variations that might suggest significant differences in the contents of containers even if they contained what they were supposed to*" [38].

To assure soundness, it must be assured that there is no hoax object with the same signature, implying the signatures must be unique. However, the uniqueness of nuclear signatures is a topic of ongoing debate and has been questioned multiple times. In 1997, a study by the U.S. Office of Arms Control and Nonproliferation identified as one of the unresolved key issues that "*all of the signatures may not be unique*" [10]. In the 2017 report of the first phase of the International Partnership for Nuclear Disarmament Verification (IPNDV) called for an "*evaluation of potential nuclear weapon intrinsic signatures before and after dismantlement*" [23]. In 2000, however, a study by the British Atomic Weapons Establishment claimed — without further proof — that combined neutron-gamma signatures of warheads "*cannot be mimicked or synthesised by other means*" [26]. Additionally, in 2023, a report by the U.S. Governmen-

tal Accountability Office (GAO) stated that "*more intrusive technologies — such as devices to measure weapons' radiation signatures — would provide increased confidence in compliance and support longer-term treaty goals but may require 5 to 10 more years of development*" [42]. A study from 2023 analyses the possibility of imitating nuclear warhead's neutron emissions using a californium-252 source [43].[8]

Different methods have been developed to ensure privacy: In the mid-1990s, the US began research on information barriers (IBs) — computers that internal process measurement data and only return non-sensitive data (often only a binary signal) to assure privacy during verification measurements [44].[9] The challenge for these systems is to ensure the computers' trustworthiness to prevent backdoors and potential manipulation [45]. Therefore, other concepts have been developed that "*use physics, not computers, to protect their information*", such as zero-knowledge proofs, that are cryptographic protocols enabling one party to convince another of the truth of a statement (e.g., "the presented object is an actual nuclear weapon") without disclosing any information [46–50]. A related concept that assures privacy by the laws of physics is *low-resolution gamma spectroscopy*, in which the photon emissions are measured using only a very small number of wide-spanning spectral bins.

Field Test 34

Even though not much research has been published on the reliability of nuclear signatures, nuclear weapon states conduct classified and publicly inaccessible research on warhead confirmation. In red-teaming exercises, they analyze different cheating attempts and possibilities. In 2015, the U.S. Arms Control and Disarmament Agency (ACDA) declassified one such exercise from 1967: the *Field Test 34* as part of *Project Cloud Gap* (1963–1969) [51]. During this exercise, U.S. military officers tried to verify the dismantlement of five types of nuclear weapons ("Mk-25, AIR-2A configuration", "Mk-28 Y2, Mod 1 Ex Bomb", "Mk-30 Yl, Mod 2", "Mk-39 Yl, Mod-2 bomb", "Mk-56, Mod 1 warhead") [52]. Additionally, four hoaxes were analyzed to assess the inspectors' ability to identify them. The hoaxes included a B-57 dummy bomb with a 0.5 kg plutonium ball surrounded by foam plastic (Figure 2.2 top), a training version of the Hawk missile, altered to mimic an advanced fission nuclear warhead with two detonators (Figure 2.2 middle), an 8-inch artillery shell featuring a 1-inch bar split into two 1-kilogram uranium segments: one of uranium-235 and the other of uranium-238, and a discarded Mk-28 bomb where the secondary component was swapped for steel ballast [51, 52]. Inspectors conducted analyses with varying levels of intrusiveness, going from elementary external inspections that determined dimensions, weight, and center of gravity to the use of gamma spectrometry, X-rays, and neutron counters. Despite highly intrusive measurements, a team of inspectors trained for ten days identified on average, only 58% of the hoaxes. Since all weapon depictions in the Field Test 34 report remain classified, I have included an illustration of a French sea-launched ballistic missile (SLBM) from the same period for comparison (see Figure 2.2 bottom).

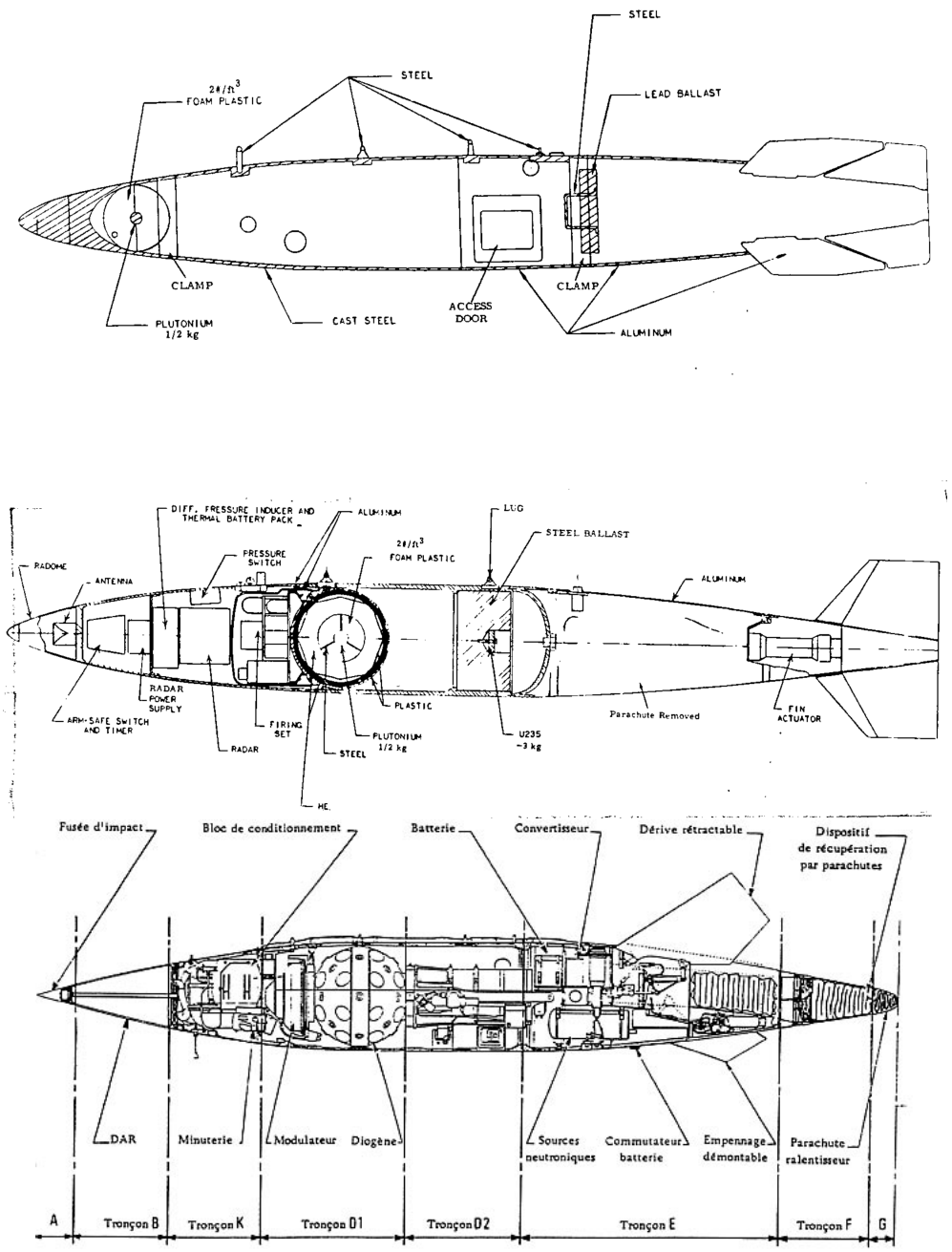

Figure 2.2: Declassified Hoaxes of Field Test 34 and a French Weapon Design
The two declassified hoaxes from the Field Test 34 (Annex D) at the top and middle. Since the Field Test 34 report only provides sketches of hoaxes but not the comparable authentic missiles, a depiction of a French missile from the 1960s is included at the bottom [53]. In the French missile, the fissile material is located in the same place as the plutonium in polyethylene in the second Field Test 34 hoax.

Notes

[1]The level of needed verification is often debated. For example, the U.S. Arms Control and Disarmament Agency called verification "*the critical element of arms control*". At the same time, the USSR stated that they "*are in favor of reasonable, balanced verification on the scale that is truly necessary*" [29].

[2]Most nuclear weapons programs benefited significantly from the assistance and information shared by nuclear-armed states and espionage activities. For example, Klaus Fuchs was a key figure in the Manhattan Project and a Soviet spy [54]. According to the Soviet intelligence officer Vladimir Barkovsky, there were, in addition, at least ten British spies who provided nuclear secrets to the USSR [55]. Resulting in the USSR's first nuclear weapon (RDS-1) was primarily based on the American Mark-3 (Fat Man). Also, the UK gained information on this weapon design via Klaus Fuchs, who served nine years in prison in the UK. In addition, the French first nuclear weapon relied on the American Mark-3 design [56]. Additional examples of nuclear espionage and knowledge transfer include Abdul Qadeer Khan's role in Pakistan's enrichment program, France's involvement in Israel's nuclear weapon program, and Israel's subsequent cooperation with South Africa, where the apartheid regime was even offered the opportunity to purchase nuclear weapons [57]. Similarly, it is believed that North Korea provided nuclear weapon instructions to Syria [58]. In 2006, the US declassified "*that the People's Republic of China obtained some Restricted Data information on the W88 warhead, and perhaps the complete W88 design*" [59]. However, it should be mentioned that there is a scholarly debate on the influence of nuclear knowledge on proliferation and other reasons of nuclear secrecy, as pointed out by Samuels 2008: "*the secrecy of the bomb is a theological construct, adopted in no small part to shield ourselves from the idea that someone might use an atomic bomb against us*" [60].

[3]Even though a trend toward more complex and intrusive verification mechanisms is evident: While the verification of SALT I and the ABM treaty relied mainly on satellite imagery, the INF treaty included on-site inspections and the exchange of telemetry information. During START and New START, neutron detectors similar to the ones used during INF inspections were established again, but solely to confirm the absence of nuclear warheads and material [34, 61]. SORT did not contain any specific verification or compliance provisions [62].

[4]Under operation, the Slava carried 16 of these SS-N-12 SLCMs [185].
The ship's history reflects global affairs after becoming a symbol of cooperative efforts to verify disarmament. In 1995, it was officially renamed "Moskva" and was eventually sunk during the Russian war of aggression against Ukraine.

[5]It was actually agreed with the Soviets to measure only 10 minutes as they were worried about longer measurement times [39].

[6]This concept dates back at least to 1967, as evidenced by the declassified reports from Field Test 34 [51].

[7]An often proposed method to ensure the golden sample's authenticity is randomly choosing a warhead from the active arsenal. This comes with further challenges. For example, many ICBM systems employ multiple independently targetable reentry vehicles (MIRV) that allow a single missile to carry multiple nuclear warheads, each capable of hitting different targets independently. However, it can be assumed that MIRV systems also contain decoys to confuse missile defense systems [63] or other "penetrating aid", for example, jam sensors [64]. It must, therefore, be ensured that no decoy or other penetrating aid is chosen as the golden sample.

[8]Throughout this thesis, I use the term "gamma signature" in alignment with the concept of "gamma spectroscopy," even though other photon sources, such as X-rays and annihilation photons, also contribute.

[9]Relying warhead confirmation on the high-resolution gamma spectrum without the IB, for example, the weapon-grade plutonium composition could be determined by comparing plutonium-peak intensities. That is an information the US is, but Russia is not willing to share [31, 65]. Sharing the exact fissile material composition may reveal information about the uranium enrichment or plutonium purification processes by analyzing the concentration of minor actinides. Different methods have been developed to separate isotopes of an element, such as electromagnetic isotope separation (EMIS), gaseous diffusion, ultracentrifugation, laser isotope separation (SILEX), and plasma-based isotope separation methods. For uranium enrichment these methods may result in varying concentrations of secondary uranium isotopes, such as uranium-233 and uranium-234, as described for

ultracentrifugation in [66]. From these, one could maybe infer the enrichment method. Another reason is that by comparing peaks from the same decay chain of isotopes, conclusions can be drawn about absorption factors of materials surrounding the fissile material, allowing conclusions about warhead design.

Chapter 3

Nuclear Verification Physics

This chapter explores the underlying physics of nuclear emissions and their measurement covering the liquid-drop model, radioactive decays, and scintillation detectors. Based on this the four warhead confirmation systems analyzed in this work are described. Finally, Monte Carlo particle transport codes are introduced, using OpenMC as an example, later used to simulate the measurement of warhead emissions within these systems.

3.1 Radioactive Decay and Nuclear Emissions*

The Liquid-Drop Model

Although the nucleus occupies less than a trillionth of an atom's volume, it contains nearly all its mass.[1] A balance between attractive and repulsive forces governs this concentrated assembly of protons and neutrons. This dynamic not only determines the stability of matter but also underlies the immense energy released in nuclear reactions. The liquid-drop model, introduced in the mid-1930s, offers a robust framework for describing nuclear properties by treating the nucleus as an incompressible fluid. In this model, the total binding energy between the nucleons is decomposed into five different terms:

$$E_{\mathrm{B}}(N,Z) = \overbrace{a_{\mathrm{V}}A}^{\text{Volume term}} - \overbrace{a_{\mathrm{S}}A^{2/3}}^{\text{Surface term}} - \overbrace{a_{\mathrm{C}}\frac{Z^2}{A^{1/3}}}^{\text{Coulomb term}} - \overbrace{a_{\mathrm{A}}\frac{(N-Z)^2}{A}}^{\text{Asymmetry term}} + \overbrace{a_{\mathrm{P}}\delta A^{-1/2}}^{\text{Pairing term}}, \tag{3.1}$$

with Z being the nucleus' number of protons, N its number of neutrons, and $A = Z + N$ representing its total number of nucleons Further, $\delta = 0$ for odd-A nuclides, $\delta = 1$ for even-Z, even-N nuclides, and $\delta = -1$ for odd-Z, odd-N nuclides.

*Main references for this section are:
- K. Bethge, G. Walter, B. Wiedemann. *Kernphysik*. 3rd ed. Springer, 2008
- T. Mayer-Kuckuk. *Kernphysik*. 7th ed. Wiesbaden: Teubner, 2002
- W. Demtröder. *Experimentalphysik 4, Kern-, Teilchen- und Astrophysik*. 5. Aufl. Springer, 2017

In this model, the *Volume term* reflects the dominant attractive strong nuclear force, which is due to its short-range nature proportional to the total number of nucleons A and nearly independent of nucleus size. The *Surface term* adjusts for the fact that nucleons on the surface experience fewer interactions. The $A^{2/3}$-dependency arises from the sphere's surface quadratic-dependency of the radius (which is in turn proportional to $A^{1/3}$). Meanwhile, the *Coulomb term* accounts for the electrostatic repulsion between protons, the scaling assumes a homogeneous charge distribution in a sphere. The *Asymmetry term* and the *Pairing term* further modify the binding energy by considering the quantum-mechanical distribution of nucleons and the stability conferred by paired nucleons, respectively.[2] Empirically determined constants [67] are:

$$a_{\mathrm{V}} = 15.5\,\mathrm{MeV},\quad a_{\mathrm{S}} = 16.8\,\mathrm{MeV},\quad a_{\mathrm{C}} = 0.715\,\mathrm{MeV},\quad a_{\mathrm{A}} = 23\,\mathrm{MeV},\quad a_{\mathrm{P}} = 11.3\,\mathrm{MeV}.$$

The liquid-drop model not only provides a framework for estimating the binding energy of a nucleus but also underpins the concept of the mass defect. Since a portion of a nucleus's mass is converted into binding energy E_{B}, the mass of the bound system is less than the sum of the individual masses of its constituent nucleons. This difference, known as the mass defect, is related to the binding energy by the equation $\Delta m = E_{\mathrm{B}}c^2$.

Figure 3.1 presents the experimentally determined average binding energy per nucleon as a function of A (based on data from the Nuclear Wallet Cards), along with the corresponding liquid-drop model predictions [71].[3] For each mass number A, the liquid-drop model binding energies computed for all viable proton numbers Z are indicated by a gray band spanning the range between the minimum and maximum values, assessing the validity of this model.

Notably, the model exhibits good agreement with the experimental data for heavier nuclei, a consequence of the reduced influence of quantum shell effects and the predominance of collective nuclear behavior.

At low mass numbers ($A < 20$), the binding energy per nucleon increases rapidly as nucleons are added, reflecting the increasing effectiveness of the strong nuclear force. The curve peaks at nickel-62, iron-58, and iron-56, where nuclei are most stable (≈8.7 MeV/nucleon). Here, the short-range nuclear attraction and long-range Coulomb repulsion between protons balance optimally. For heavy nuclei ($A > 60$), binding energy per nucleon decreases due to Coulomb repulsion overwhelming the strong force. Besides this smooth behavior, some nuclei like helium-4 show unusually high stability. This is the case as both their number of protons and neutrons are equal to "magic numbers", corresponding to filled nuclear shells.[4]

Not seen in the curve are two more observations: while for $Z < 20$, stability occurs for $N/Z \approx 1$ for greater Z, this quotient gradually increases; and there are no stable configurations with $Z \geq 82$ (lead).

The binding energy curve encapsulates the fundamental physics underlying the enormous energy release in nuclear weapons. In fission reactions, fissile nuclides such as uranium-235 or plutonium-239 — positioned on the right side of the curve where the binding energy per nucleon is relatively lower — are split into smaller fragments. This fission process decreases

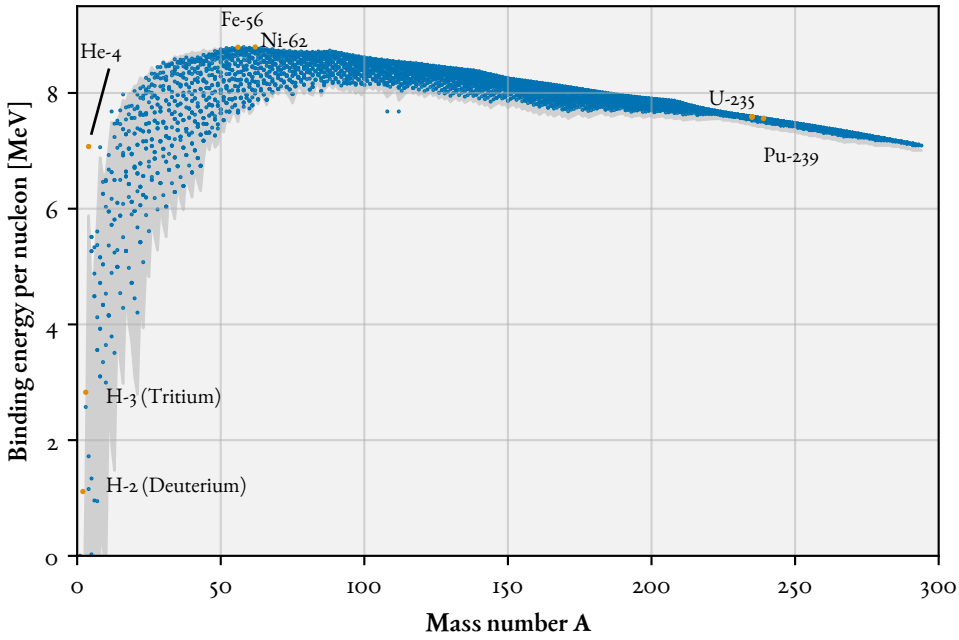

Figure 3.1: Binding Energy Curve
The average binding energy per nucleon in relation to the atomic mass A in the form of a scatter plot for all nuclides in the Nuclear Wallet Cards [71]. Liquid drop model binding energies per nucleon were computed for all nuclides in the Nuclear Wallet Cards. The grey band indicates the range between minimum and maximum values at each mass number.

the average binding energy per nucleon by about 0.85 MeV, releasing approximately 200 MeV per event as kinetic energy. In contrast, fusion reactions exploit the left side of the curve: light nuclei, typically deuterium and tritium, fuse to form a nucleus with a higher binding energy per nucleon, typically helium-4. This fusion increases the average binding energy by roughly 3.5 MeV, resulting in an energy release of about 17.6 MeV per fusion event.

Radioactivity

The balance between attractive and repulsive forces inside the nucleus yields a rich diversity in nuclear stability. To date, 254 stable nuclides have been identified, alongside 3,154 unstable nuclides [72, 73]. Unstable nuclides undergo radioactive decay, a process in which the nucleus transitions to a state of lower energy and increased stability by emitting particles or electromagnetic radiation. Each decay mode is characterized by the emission of particles or electromagnetic radiation with distinct energy. As discussed in Chapter 2, various methodologies for confirming nuclear warheads rely on detecting these primary emissions or the secondary particles they generate, thereby exploiting the unique properties these emissions.

The decay rate of a radioactive nuclide is governed by its decay constant λ, which defines the number of isotopes $N(t)$ at time t as

$$N(t) = N(0)\mathrm{e}^{-\lambda t}. \tag{3.2}$$

The half-life $T_{1,2}$ is defined as the time required for half of the initial amount of material to decay

$$T_{1,2} = \frac{\ln(2)}{\lambda}. \tag{3.3}$$

When a radioactive nuclide decays into another radioactive nuclide, a decay chain is formed. The Bateman equations describe the evolution of the nuclide concentrations in such a chain, which represent a system of coupled first-order differential equations. These equations can be expressed and solved using the matrix exponential. In cases where the half-life of the parent nuclide is significantly longer than that of its child, an equilibrium will be reached, in which the child nuclide decays at the same rate as it is produced, i.e. for the amounts of nuclides N_i and their decay constants λ_i, the following holds:

$$\lambda_1 N_1 = \lambda_2 N_2 \tag{3.4}$$

Such equilibria, which can extend over multiple subsequent decay steps, are effectively represented by the eigenvectors of the decay matrix derived from the Bateman equations. This general behavior of decay chains is referred to as transient equilibrium. In the limiting case where the parent's half-life is much longer than that of its progeny (typically by a factor of 10^4 or more), the parent's activity can be approximated as constant — a situation known as secular equilibrium.

Types of Radioactive Decay

Radioactive decay occurs via several mechanisms governed by intrinsic nuclear properties, such as the neutron-to-proton ratio, and binding energy. One category of decays involves the emission of nuclear fragments, which can vary in size and complexity. This range begins with the ejection of a single proton (proton emission), continues with the release of a helium nucleus (α-decay), and extends to the rarer emission of larger clusters — such as a carbon-14 nucleus — in what is known as cluster decay [74]. In addition, specific heavy nuclei may undergo spontaneous fission, splitting into two nearly equal fragments while releasing substantial energy [75, 76].

The Gamow model provides a quantum mechanical description of α-decay, wherein a preformed helium nucleus tunnels through the Coulomb barrier of the parent nucleus. A similar tunneling framework can be applied to proton emission, and a Gamow-like approach has also been utilized to model cluster decay [77].

Further, heavy nuclei can fission spontaneously, which is generally less probable than α-decay. The liquid-drop model explains spontaneous fission through the balance of surface and Coulomb energies. However, shell effects stabilize many nuclei, delaying measurable fission rates until $A \gtrsim 230$ and ${}^{Z^2}/_{A} \gtrsim 34$ as during deformation from spherical to dumbbell shapes, the Coulomb energy initially decreases, while surface energy increases, creating a potential barrier.
According to the Nuclear Wallet Cards, 205 nuclides can undergo spontaneous fission, with the lightest among these being plutonium-230. The parameter ${}^{Z^2}/_{A}$, which serves as an indicator of the balance between the surface and Coulomb force, spans a range from 34.91 for thorium-232 to 47.04 for tennessine-290 [71]. Besides two excited fragments, which decay and produce further emissions, several neutrons are emitted. The energy of the neutrons created during a spontaneous fission event can be described by a Watt distribution

$$W_{a,b}(a,b) = \sqrt{\frac{\pi b}{4a}} \cdot \frac{\mathrm{e}^{b/4a}}{a} \cdot \sinh\left(\sqrt{bE}\right) \cdot \mathrm{e}^{-aE}. \tag{3.5}$$

Where the nuclide-dependent variables a and b are empirically estimated [78]. Table 3.1 provides an overview of the Watt parameters a and b, and the multiplicity values $\bar{\nu}$ — the average number of produced free neutrons during a spontaneous decay — for nuclides relevant in this work.

	$T_{1,2}$ [s]	a [MeV^{-1}]	b [MeV^{-1}]	$\bar{\nu}$
Uranium-235	2.2210×10^{16}	1.29080	4.85231	1.86
Uranium-238	1.4100×10^{17}	1.54245	6.81057	2.01
Plutonium-238	2.7680×10^{9}	1.17948	4.16933	2.21
Plutonium-239	7.6090×10^{11}	1.12963	3.80269	2.16
Plutonium-240	2.0705×10^{11}	1.25797	4.68927	2.156
Plutonium-241	4.5100×10^{8}	1.18698	4.15150	2.25
Plutonium-242	1.1770×10^{13}	1.22078	4.36668	2.145
Americium-241	1.3650×10^{10}	1.07179	3.46195	3.22
Californium-252	8.3470×10^{7}	0.847458	1.03419	3.757

Table 3.1: Relevant Nuclides Watt Parameters and Multiplicities
Spontaneous fission neutron emission parameters for weapons-related nuclides and californium-252. Half-lives $T_{1,2}$ are sourced from the Evaluated Nuclear Structure Data Files (ENSDF) [73], Watt spectrum parameters (a, b) from [78], and multiplicity values $\bar{\nu}$ from [79].

In deployed nuclear weapons, neutrons generated from spontaneous fission may either trigger additional fission reactions or induce high-energy photon emissions through (n, γ) and

$(n, n'\gamma)$ reactions in surrounding materials. In (n, γ) reactions (neutron capture) the neutron is either absorbed by a nucleus forming an excited compound nucleus that emits photons during de-excitation. Alternatively, in $(n, n'\gamma)$ reactions, the neutron transfers energy to the nucleus via inelastic scattering, resulting in an excitation of the nuclide's energy level and the emission of photons upon de-excitation. Measurements of these photon emissions — particularly those produced in the chemical explosive, as detailed in Table 5.6 — have been proposed as a method for warhead confirmation [80]. Additionally, measurements of these photons provide an estimate of the weapon's age, as they allow one to estimate the carbon-14 fraction in the chemical explosive's that accumulates over time via neutron capture [81].

Another type of decay is β-decay, in which either a neutron is transformed into a proton, an electron, and an antineutrino (β^--decay); or a proton is transformed into a neutron, a positron, and a neutrino (β^+-decay). During an Electron Capture (EC) — sometimes considered as a type of β-decay, a electron (most often from the K-shell) is absorbed into the nucleus, where it combines with a proton, forming a neutron and a neutrino. The filling of the resulting gaps in the electron shells, leads to the emission of either characteristic X-rays or Auger electrons.

Gamma decay

After a radioactive decay or fission event, the resulting nucleus is often left in an excited state, whereby each nuclide has several such discrete, quantized energy levels. While the nucleus may undergo further decay to transform into another nuclide, the predominant mechanism for de-excitation — transitioning from a higher to a lower excited state or the ground state — is the emission of electromagnetic radiation in the form of γ-rays. This process is known as γ-decay.
In general, the nucleus undergoes de-excitation very rapidly, often in less than a nanosecond. However, when the energy difference between the excited and the ground state is very small while the change in angular momentum is significant, a nucleus can become "trapped" in the excited state. These long-living, excited states are called metastable or nuclear isomers. An exceptional example is tantalum-180: while its ground state exhibits a half-life of 8.15 hours, its slightly excited metastable state tantalum-180* — which lies 77.2 keV above the ground state — has a half-life greater than 7.1×10^{15} years — exceeding by far the age of the universe.

The gamma emissions of the different nuclides will be the focus of this work. As for the other decays, I will rely upon their energy and intensity on experimental databases [73].

Further De-excitation Pathways

Besides the γ-decay, there are other pathways of nuclear de-excitation: During internal conversion, the energy of the nucleus is directly transferred to a shell electron, which is emitted. As

the shell is refilled by an electron from an outer shell, this process is followed by the emission of X-rays or Auger electrons. The processes of internal conversion particularly allows transitions between states with the same angular momentum.
When the excited state has an energy above 1.022 MeV, the energy of the nucleus can also be transferred into an electron-positron pair, which is then emitted.

3.2 Warhead Confirmation Systems

Sodium Iodide Scintillation Detectors

All analyzed warhead confirmation systems rely on a sodium iodide (NaI) scintillation detector, of the same design and dimensions. The sodium-iodide (NaI) scintillator takes the form of a cylinder measuring 2 inches in both diameter and height. Thallium is added at approximately 10^{-3} mole fraction to create luminescence centers in the NaI crystal. Incoming photons excite electrons from the valence to the conduction band, depositing energy into the crystal. These electron-hole pairs migrate to the luminescence centers. In NaI(Tl), the activator thallium introduces additional energy states within the forbidden band, facilitating electron de-excitation. During this process, photons with a wavelength of approximately 415 nm (2.987 eV) are emitted. As the energy of these photons is below the band gap of NaI, the crystal becomes effectively transparent to them. Due to the low quenching effects — which would be, for example, loss to non-radiative processes, like heat lattice vibration production — in NaI(Tl) crystals, the number of created photons is proportional to the energy deposited by the incoming photon. The light yield of NaI(Tl) detectors is about 38,000 scintillation photons per 1 MeV of absorbed energy. To maximize the number of photons detected, the detector is surrounded by reflective material. The scintillation photons pass an optical window and release electrons from the photocathode, which are then channeled into a photomultiplier tube (PMT), initiating a cascade of electrons. The resulting voltage pulse height, which can be measured, is directly proportional to the number of photons entering the PMT. These, in turn, are proportional to the energy the photon deposits in the scintillating material [83]. Figure 3.2 illustrates the detection process of a photon.

Information Barrier eXperimental

The Information Barrier eXperimental (IBX), developed at Princeton University in 2018, measures the passive gamma spectrum of objects up to 3 MeV across 3,000 energy bins [19]. The measured spectra are compared using the Kolmogorov-Smirnov test [144]. In this statistical test, the maximum norm between the cumulative functions of the spectra is computed (with null-hypothesis H_0, both spectra follow the same probability distribution). If it surpasses the threshold value

$$d_\alpha = c(\alpha) \cdot \sqrt{\frac{n_1 + n_2}{n_1 \cdot n_2}}, \tag{3.6}$$

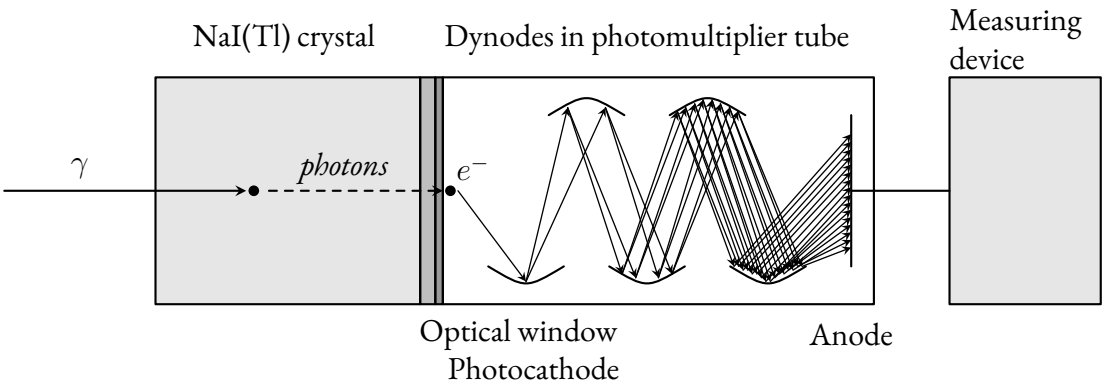

Figure 3.2: Detection Process in a Scintillation Detector
A photon (γ) enters a NaI(Tl) crystal, where it is converted to a large number of low-energy photons, which then strike the photocathode of a photomultiplier tube. The released electrons (e^-) are amplified through multiple dynode stages before reaching the anode, with the final signal being recorded by a measuring device [84].

where n_1 and n_2 denote the sample sizes and $c(\alpha)$ is the Kolmogorov distribution, the null hypothesis H_0 is rejected at a significance level of α. For IBX, the value d_α was set to an artificial threshold of $D_0 = 0.01$. This threshold represents the maximum allowable difference between the two measured gamma spectra. The system's functionality was demonstrated for non-nuclear-warhead-related materials and tested with cobalt-60 and caesium-137 sources. Approximately 1,000,000 counts were used in the trial measurements with other radioactive materials. The authors state that the threshold may change for actual warheads or warhead components and would be part of negotiations [19]. It tries to balance the sensitivity and specificity needed to detect significant deviations. The system is shown in Figure 3.3 on the top left.

Information Barrier eXperimental II

Developed in 2019 at Princeton University, the Information Barrier eXperimental II (IBX II) is centered around the MOS 6502 processor, a chip first produced nearly 50 years ago [20]. The chip's simplicity reduces potential vulnerabilities and should prevent potential backdoors that could be exploited to reveal sensitive information. To confirm an object, IBX II records a gamma spectrum with 262,144 (2^{18}) counts, and summarizes the result in 12 equidistant energy bins (the first and the last bin are smaller than the central bins, see Table 3.2). Subsequently, it uses the χ^2-test

$$\chi^2 = \sum_{i=1}^{12} \frac{(M_i - T_i)^2}{T_i}, \tag{3.7}$$

for comparing the object's low-resolution spectrum with the template's. Here T_i is the number of counts of energy bin i of the template, and M_i is the respective number of counts of the respective measurement. If $\chi^2 < 100$, it is assumed that the inspected object matches the template. The system is shown in Figure 3.3.

Trusted Radiation Identification System

The Trusted Radiation Identification System (TRIS), developed at Sandia National Laboratories from 1999 to 2001 and successfully tested at the Pantex Plant, has been demonstrated to reliably identify various types of weapons and weapon components [85]. While IBX II uses equally sized energy bins between 0 and 3 MeV, the bin structure of TRIS is motivated by specific gamma emissions [86]. In the bin structure of TRIS, key γ-ray emissions are isolated (see Table 3.2). It specifically targets the 186 keV gamma emission of uranium-235, the full-energy peak of plutonium-239 across two combined bins (290–350 keV and 390–500 keV), excludes the 208 keV gamma emission of uranium-237 due to its variability in plutonium, includes bins for americium-241 at 662 keV, uranium-238 at 766 keV and 1001 keV, and uranium-232 at 2614 keV, which is variable in highly enriched uranium (HEU) [86].[5] For comparing the object with a template, TRIS uses the reduced χ^2-test

$$\chi_r^2 = \frac{1}{f} \cdot \sum_{i=1}^{14} \frac{(M_i - T_i)^2}{T_i}. \tag{3.8}$$

Here, f denotes the system's degrees of freedom f (here the number of independent bins is 14). The initial publication on TRIS states that objects will be accepted if $\chi_r^2 < 4$, but does not specify a measurement time or activity of the object. Both are crucial since the value of the χ^2-test scales linearly with the detected counts. In a newer publication, a measurement time of one minute for sources of 500 g plutonium and 500 g highly enriched uranium is denoted [87]. Another publication mentions a measurement time of ten minutes [85]. For the subsequent simulations, TRIS is assumed to determine the spectrum with 2^{18} counts analogous to IBX II. In 2010, the Next-Generation TRIS (NG-TRIS) was introduced, enhancing security and data integrity [88].[6] The third generation of TRIS (3G TRIS) was tested for the first time in June 2024 at the Pantex Plant and presented shortly thereafter [21]. The main change in 3G TRIS is the use of a CsI scintillation detector in place of NaI. In this work, only the NaI scintillation detector is analyzed. TRIS, NG-TRIS, and 3G TRIS rely on the same energy bin structure.[7] The system is depicted in Figure 3.3

Confirmation System	Energy bins [keV]
IBX II	[0–197), [197–451), [451–706), [706–960), [960–1,215), [1,215–1,469), [1,469–1,724), [1,724–1,978), [1,978–2,233), [2,233–2,487), [2,487–2,742), [2,742–2,950)
TRIS	[80–120), [120–160), [172–198), [230–290), [290–350) & [390–500), [350–390), [500–600), [600–711), [711–821), [821–936), [936–1,090), [1,090–1,200), [1,200–2,480), [2,480–2,750)
Excluded	[160–172), [198–230)

Table 3.2: Energy Bin Structures of IBX II and TRIS
The semi-open bin boundaries are discernible from the publicly available assembler code of IBX II [89]. In the absence of published information for TRIS regarding the handling of energy bin limits, the same approach as that used for IBX II has been adopted.

Multi-Criteria Template-Matching

Göttsche, Schirm and Glaser propose a Multi-Criteria Template-Matching (MCTM) approach [18]. The setup employs a NaI scintillation detector behind a 15 cm polyethylene mask and 5 cm steel shield, with a central hole allowing direct gamma detection.[8] This configuration enables simultaneous measurement of the object's photon emissions, the object's neutron emissions via the measurement of the neutron-induced 2,223 keV gamma peak (from neutron capture in hydrogen in the polyethylene), and the object's total count-rate in a single gamma spectrum. However, the polyethylene mask significantly degrades the energy resolution, due to increased photon scattering. The authors conclude that "*the combination of an empirical Kolmogorov-Smirnov test, the total gamma count-rate test, and the total neutron count-rate test (combined with a polyethylene mask) constitute an effective concept to distinguish valid from invalid plutonium items*" [18]. As no threshold values for the individual tests are provided, the KS-test threshold of $D_0 = 0.01$ (similar to IBX) is assumed. The system is shown in Figure 3.3.

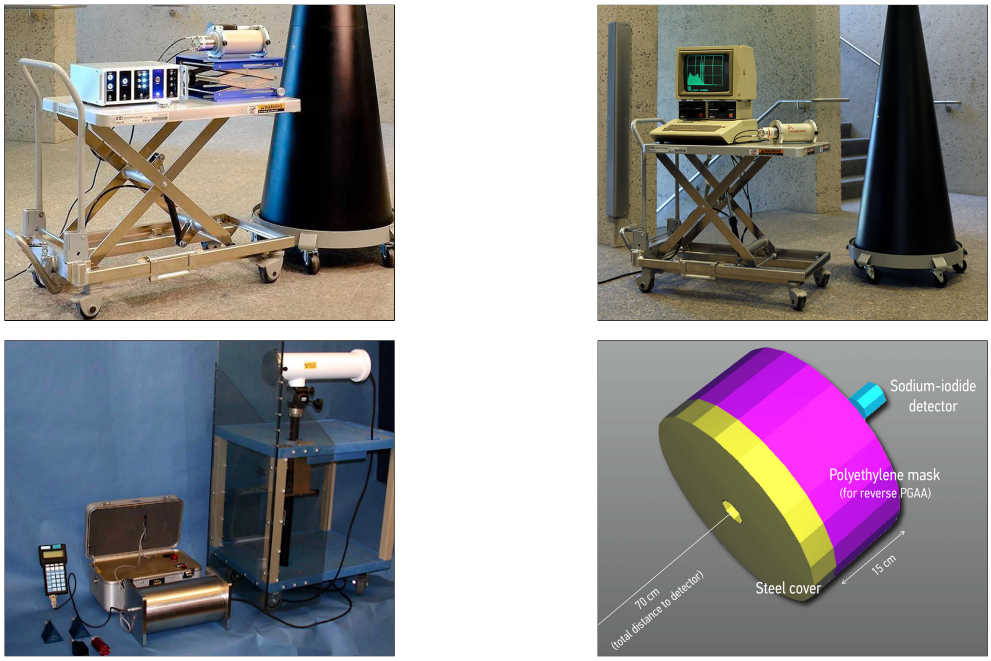

Figure 3.3: Warhead Confirmation Systems
From top left to bottom right: The Information Barrier eXperimental (IBX) [20], the Information Barrier eXperimental II (IBX II) [19], the Trusted Radiation Identification System (TRIS) [90] and the Multi-Criteria Template-Matching (MCTM) approach [18].

3.3 Monte Carlo Particle Transport Codes

All simulations in this work have been performed using the open-source Monte Carlo particle transport code OpenMC [91]. The origins of Monte Carlo methods date back to the Manhattan Project in the 1940s, where scientists faced critical challenges in solving neutron transport problems essential for developing nuclear weapons. Neutronic properties of a system can be determined by solving the particle transport equation, which is based on the Boltzmann transport equation. Deterministic methods for solving this equation involve discretizing core variables: the geometry is divided into small regions, the angular variables are treated using S_n (discrete ordinates) or P_n (spherical harmonics expansions) methods, and the energy is discretized into several groups with flux-weighted constant cross-sections [92]. However, for complex problems, solving particle transport equations deterministically becomes highly challenging. Furthermore, particle transport equations do not capture all system characteristics, as they omit correlations and the detailed histories of particle interactions. Consequently, features such as coincidence counts and pulse-height values cannot be determined solely from these equations (see Section 4.2) [93].

In 1946, Stanislaw Ulam proposed the Monte Carlo method as a new approach to tackle neutron transport problems. This method involves simulating individual particles randomly traversing a system and keeping track of their interactions.

A simplified OpenMC Monte Carlo particle transport simulation is executed as follows, with a comparable schema applicable to analogous codes.

1. Particles are initialized with a defined position, direction, and energy within a discretized geometry composed of cells containing various materials.

2. The particle's free path

$$s(E) = -\frac{\ln(\xi)}{\Sigma_t(E)}$$

is sampled based on its energy and the underlying material of the cell in which the particle is located. Here Σ_t is the material's total macroscopic cross-sections (representing the overall probability of interaction), and ξ is a pseudo-random number in $[0, 1)$. OpenMC employs a Permuted Congruential Generator (PCG) to generate a series of random numbers [94]. This is done by using a Linear Congruential Generator (LCG) in the first step:

$$\xi_{i+1} = g\xi_i + c \mod M$$

with $M = 2^{63}$, $g = 2,806,196,910,506,780,709$, and $c = 1$.[9] In the second step, these numbers are permuted to enhance their statistical quality.

3. A new free path is sampled if the particle exits its current cell. Otherwise, the specific reaction is determined by comparing ξ to sub-interval of $[0, 1)$ defined by the relative probabilities of each interaction

$$\text{Interval(reaction j)} = \left[\frac{\sum_{i=1}^{j-1}\Sigma_i(E)}{\Sigma_t(E)}, \frac{\sum_{i=1}^{j}\Sigma_i(E)}{\Sigma_t(E)}\right),$$

where Σ_i are the macroscopic cross-sections of the individual reactions (for $j = 1$ the interval starts at zero). After the reaction, the particle's position, energy, and direction are updated, and any secondary particles produced are stored in a *bank* for later simulation. The process is repeated by sampling a new free path until the particle is terminated (for example, by falling below an energy threshold or exiting the predefined geometry).

Throughout the simulation, data is collected using *tallies* that record specific events, such as energy deposition or reaction occurrences. The statistical behavior of particles allows for inferring the underlying properties of the system [95]. To achieve statistically reliable results, a

large number of particle histories must be simulated, as the variance decreases with the inverse square root of the number of particles. Since Monte Carlo methods evaluate individual particle tracks, they exhibit excellent scalability and have become the gold standard for solving particle transport problems.[10]

Notes

[1]An atom's diameter is roughly 10^{-10} m, while its nucleus measures in the order of 10^{-14} m [68]. The uncertainty principle limits the precise determination of the volume.

[2]There is an enhanced stability observed in nuclei with even numbers of protons and/or neutrons, where nucleons can form pairs with opposite spins, resulting in stronger binding for even-even nuclei compared to odd-odd nuclei.

[3]Most representations of this curve only show the most stable nuclides — the scatter plot's upper edge.

[4]The magic numbers are 2, 8, 20, 28, 50, 82, and 126. Other such doubly magic nuclei are oxygen-16 and calcium-40.

[5]Table 5.5, provides an overview of the strongest photon emissions of weapon-related nuclear materials.

[6]This was done by integrating an internal multichannel analyzer and fully authenticating Complex Programmable Logic Device (CPLD) data.

[7]In addition, TRIS allows different uncertainties for the template, which is not considered here.

[8]In the absence of explicit dimensions, the hole is assumed to be 2.25 cm in diameter, covering half of the detector's active volume.

[9]As M and c are coprime (satisfied as $c = 1$), and $g - 1$ is divisible by all prime factors of M (which only has the prime factor 2), and $g - 1$ is divisible by four if M is divisible by four (satisfied as M is not divisible by four) it follows by Hull-Dobell's theorem, that the sequence of generated pseudo random numbers has a maximal periodicity of $M = 2^{63} \approx 9 \cdot 10^{18}$ [96].

[10]The success of Monte Carlo methods is intrinsically linked to the evolution of computers, as these techniques rely on executing vast numbers of simple calculations. Initially, calculations were performed by "human computers" (often wives of the scientists in the Manhattan Project) who manually carried out the necessary computations. In 1947, Enrico Fermi developed the FERMIAC, an analog computer, also known as the "Monte Carlo trolley," which significantly accelerated Monte Carlo calculations. In 1948, the first Monte Carlo simulation was run on the ENIAC (Electronic Numerical Integrator and Computer), the first general-purpose electronic digital computer. The ENIAC was subsequently succeeded by the MANIAC (Mathematical Analyzer, Numerical Integrator, and Computer), which became operational in March 1952. IBM released the first FORTRAN compiler in April 1957, enabling the development of Monte Carlo codes in a high-level programming language. The Monte Carlo N-Particle Transport Code (MCNP) written in FORTRAN was first created in 1977 by merging several specialized Monte Carlo codes (MCNG and MCP) and was released in 1983. It is export-controlled, and its distribution is managed by the Radiation Safety Information Computational Center (RSICC). MCNP (last published version MCNP6.2 in 2018 [97]) is still one of the most widely used Monte Carlo codes. Open-source alternatives are GEANT ("GEometry ANd Tracking", current version GEANT4), which CERN developed in the context of high-energy physics, and OpenMC, which was developed at the Massachusetts Institute of Technology with the focus on simulations of nuclear reactors [91, 98].

Chapter 4

Development and Validation of Simulation Tools

This chapter describes the new simulation tools I implemented to conduct the analyses in this work. The first enables the determination of the composition of decaying material, for example, in deployed nuclear warheads. It considers both spontaneous and induced fission based on ENSDF data. Further, it allows the determination of the photon and neutron production rates in this material. The second tool allows the simulation of gamma spectroscopy measurements using open-source tools by implementing a pulse-height tally functionality in OpenMC.

4.1 Material Depletion Module*

Material composition changes due to radioactive decay. Unlike "conventional radioactive material," in deployment-ready nuclear warheads, the material has a non-negligible criticality (see Section 5.1.1). Neutrons from spontaneous fission will initiate numerous additional fissions in diminishing fission chains. For example, in the Fat Man model, every spontaneous fission entails a fission chain of 22 additional fissions [99].[1] To correctly simulate the decay of the material in nuclear warheads, it is necessary to consider both the spontaneous and the induced fissions, together with the other radioactive decay.
A wide range of tools was designed to determine the change in nuclide composition under induced fission for simulating reactor operations (depletion). The U.S. national laboratories de-

*Parts of this section are based on the following publications, which primarily build upon my own work and have been further expanded here:

- **C. Fichtlscherer** et al. "Modeling Spontaneous Fission-Driven Isotopic Change in Subcritical Nuclear Systems". In: *66th Annual Meeting of the Institute of Nuclear Materials Management (INMM) (Submitted)*. 2025
- **C. Fichtlscherer**, M. Kütt. "Uniqueness, Reproducibility and Discrimination of Nuclear Warhead Gamma Signatures". In: *Science & Global Security* 32.1–3 (2024). DOI: 10.1080/08929882.2024.2387966

veloped the export-controlled codes CINDER [100] and ORIGEN [101]. Open-source alternatives are ONIX [102], the depletion module of OpenMC [103] and the `G4RadioactiveDecay` class of Geant4 [104].
While CINDER and ORIGEN include spontaneous fission in their models, the open-source alternatives ONIX and the OpenMC depletion module do not. Geant4 includes spontaneous fission modeling, but its implementation is less specialized and validated for neutron transport and fission chain simulations compared to MCNP and OpenMC [105–108]. CINDER, ORIGEN, ONIX, and OpenMC's depletion module are optimized for critical systems (reactor operations). To determine the induced fission rate, they will evaluate the flux or fission rate using eigenvalue (criticality) simulations and scale them with the reactor power. Since eigenvalue simulations are only suitable for systems of criticality close to one, they are not suitable for the simulation of sub-critical systems [109].
This highlights a gap in well-validated open-source tools for simulating the decay of material sub-critical systems, such as deployed nuclear warheads. I implemented a new open-source depletion module that can include OpenMC tally results to determine the depletion of the material under a steady fission rate from the spontaneous fission neutrons. The induced fission rate was determined in a "fixed-source" simulation. The code can also be iteratively run with OpenMC to update the nuclide composition periodically. After the decay of a mixture of nuclides, the tool can also determine the photon and neutron production rates of that material.

Nuclear Decay and Emission Data

The most comprehensive and validated nuclear decay data are provided by the Evaluated Nuclear Structure Data File (ENSDF), which is a regularly updated database maintained by the National Nuclear Data Center (NNDC), coordinated by the International Atomic Energy Agency (IAEA) [110]. The data contains information on nuclear properties, decay characteristics, energy levels, half-lives, radiation types, intensities, and uncertainties, whereby the data is not interpolated and the result of experimental evidence or well-founded theory [111]. Two researchers within the IAEA's Nuclear Data Center have called ENSDF the "*major library for structure and decay data*" [112].
While the Geant4's `G4RadioactiveDecay` class relies on this ENSDF data, the other mentioned tools rely on the Evaluated Nuclear Data Files (ENDF).[2] The ENDF decay sublibrary is a reduced data set of the ENSDF data. For example, the ENDF/B-VIII.0 decay sublibrary excludes, among others, isomeric states with half-lives shorter than one millisecond or those that decay solely via internal transition [113].
Several agencies provide edited versions of preprocessed ENSDF data. In the following, NNDC's NuDat 3.0 data is used [73]. NuDat 3.0 additionally incorporates data of the Nuclear Wallet Cards — a lightweight decay database, also provided by the NNDC [71, 114].[3] Besides ENSDF data, the Nuclear Wallet Cards also include data from the Experimental Unevaluated Nuclear Data List (XUNDL) if it is more recent [115]. This way, the NuDat 3.0 data also incorporates some XUNDL data. The data was crawled from NuDat's Decay Radiation

Search using a Python script, yielding 197,294 decays and radioactive transitions for 3,162 unstable nuclide states.
In the downloaded data, 53 nuclides have more than one non-zero energy level, whereby 21 of these do not change energy level at all but decay directly from their energy level into another nuclide. For the remaining 32 nuclides, the available data does not provide information on the de-excitation branching ratios from higher to lower energy levels. I determined the de-excitation branching ratios, manually, by comparing the intensities of emitted electrons from internal conversion, the emitted γ-rays corresponding to each energy state, as well as coincidence probabilities and the decay schemes provided by the NNDC.
Additionally, the data of the Nuclear Wallet Cards was included, as Nudat 3.0 does not contain data on stable nuclides, spontaneous fission branching ratios, and Electron Capture (EC) branching ratios.[4] The dates for the Q-values of individual decays, as provided by the NNDC, were separately downloaded and incorporated into the analysis [114]. The data on spontaneous fission neutron production rates and their energy distribution were included from the Fission Reaction Event Yield Algorithm (FREYA) [78]. The spontaneous fission yields are taken from the Spontaneous Fission Product Yields Reaction Sublibrary, the neutron-induced fission yields from the Neutron Induced Fission Product Yields Sublibrary of the ENDF/B-VIII.0 database [116]. ENDF/B-VIII.0 provides yields for neutron-induced fission for 31 nuclides and spontaneous fission yields for nine nuclides.[5] As there is no spontaneous fission yield data for the plutonium isotopes, the thermal fission yield data were used as an approximation.[6]

The data was cleaned of physical nonsensical and incomprehensible entries and rounding errors in the first step. Among other things, a one-to-one relationship of half-life and energy level for a nuclide was created, and floating energy levels were converted into numerical values. If the sum of the branching ratios of the decays exceeds one, I have normalized them to one hundred percent.

Isotopic Change in the Material

I consider Internal Transition (IT), α, β^-, β^+, γ, and electron capture (EC) decays.[7] Further, nuclides can be transmuted via spontaneous or induced fission, whereby the induced fission rate is an input to the code given in the unit number of fissions per nuclide per second, which is determined in a separate OpenMC "fixed-source" simulation. To include an induced fission rate in the decay, I calculated pseudo-half-lifes that take the fission rate, in addition to the regular decays, into account.

After a decay or fission, a nuclide is often in a discrete excited state. A nuclide can have, for example, several β^- decays to different excited states of its child. The different excitation states have, in turn, different decay properties. A nuclide in an excited state can either decay again to another nuclide or undergo de-excitation via IT or γ-decay. The children's energy level after a decay was determined by subtracting the Q-value from the decay energy and taking the next

smaller energy level.[8] I assume that a nucleus undergoes de-excitation to the ground state after EC before it decays further. For the transition probabilities between the different energy levels of one nuclide, there are two different cases, I determined the transition probability from the higher to the lower energy level by subtracting the summed branching ratios of all other decays from one hundred percent. The 32 nuclides with more than one non-zero energy levels are treated individual.

For a given nuclide composition, the code determines the entire decay chain of each nuclide and calculates the change in nuclide composition by solving the underlying Bateman equations via the respective matrix exponential [117]

$$N_t = N_0 \cdot e^{\mathbf{A}t}. \tag{4.1}$$

Here N_0 denotes the initial nuclide composition, N_t the nuclide composition after time t, and $\mathbf{A}$ the decay matrix that further includes the information of spontaneous and induced fission. As $\mathbf{A}$ is sparse and covers many orders of magnitudes, special methods are needed to determine the matrix exponential: I use the Chebyshev Rational Approximation Method (CRAM) of order 48 [118].

Photons and Neutron Production Rates

After the decay of the mixture of nuclides, the code determines the photon and neutron production rates of that material.
Photons are produced either by γ-decay, electron shell transitions (after an electron emission during an internal transition), or by positron annihilation (after a β^+-decay). Other sources, like Bremsstrahlung, are not considered. NuDat does not indicate consistently which nuclide each emission is assigned to. Sometimes, they are assigned only to the parent, sometimes to the child, and sometimes to both. For example, the most significant part of caesium-137 decays via a β^--decay to barium-137*, which undergoes de-excitation to barium-137. According to the NuDat data, both caesium-137 and barium-137*emit a 661.657 keV γ-ray, which can create errors by double counting this emission. To avoid this double-counting, I only assign the photon emissions to the direct nuclide responsible for that decay. This means that in the example above, caesium-137 does not emit any γ-ray, but barium-137* does.
The neutron production rates were determined based on the FREYA data (see Table 3.1).

Validation

I compared the results of the decay module with the results produced by ONIX. To do so, I decayed all 271 nuclides with a half-life of one week or longer for one half-life, then, I determined the difference in the decayed material's nuclide combinations with the ONIX results (using the non-reduced ENDF/B-VIII decay chains).

The analysis of 271 nuclides showed that the absolute difference in decay data exceeded one percent for 33 nuclides. All these discrepancies are attributable to variations between the decay databases used. For instance, nuclides such as niobium-92*, tellurium-123, europium-148*, hafnium-179*, tungsten-178*, and iridium-192* are stable in the ONIX-used ENDF data set, whereas they are considered unstable in the ENSDF database. Other nuclides exhibit differences in half-lives or branching ratios, leading to significant disparities. An extreme case is mendelevium-258; according to ONIX, it undergoes α-decay to einsteinium-254's ground state, which would result in a substantial accumulation of einsteinium-254 due to its 276-day half-life. However, ENSDF data suggests that mendelevium-258 predominantly decays to an excited state of einsteinium-254, which has a much shorter half-life (39 h) and decays via β^--decay.[9]

The emission rates are consistent with the ones for aged uranium of different enrichment provided in [119, 120]. Further, I compared the simulation results of several cases to results calculated by hand.

4.2 Pulse-Height Tally Functionality in OpenMC*

Gamma spectroscopy measurements can be simulated using a pulse-height tally (PHT) functionality of Monte Carlo particle transport codes. Such a functionality must account for the complete simulation history of a particle's energy deposited in a particular volume. Under optimal conditions, the simulated output signal from the detector correlates proportionally with the deposited energy of the detector's active volume. OpenMC lacked the capability of a pulse-height tally for photons, which I implemented and validated. Starting with 0.13.4-dev, the tally has been incorporated into the primary OpenMC code base. I also wrote the OpenMC example on how to simulate gamma detectors, which is available at:

https://github.com/openmc-dev/openmc-notebooks/blob/main/gamma-detector.ipynb

By a development team member, it was recognized that "*every nuclear engineer out there using OpenMC will agree this is an incredibly useful piece of functionality. Maybe it's why people are still hanging on to ol' MCNP, even*" [121]. Deterministic approaches such as those used within GADRAS-DRF [122] allow for exact calculations of the detector response, but are limited to relatively simple detector geometries. Several established codes exist to determine the detector's response function that use Monte Carlo particle transport methods. Examples are MCNP 6.2 [97], GEANT4 [104], FLUKA [123, 124], EGSnrc [125], EGS5 [126], PENELOPE [127], MCSHAPE [128], MARTHA [129], or SIMSPEC-G [130].

*Parts of this section are based on the following publication, which primarily builds upon my own work and has been further expanded here:

- **C. Fichtlscherer** et al. "Modeling gamma detectors in OpenMC: Validation of a newly implemented pulse-height tally". In: *Progress in Nuclear Energy* 172 (2024). DOI: 10.1016/j.pnucene.2024.105186

All the listed code packages have limitations. Some are export-controlled (MCNP, GADRAS-DRF, and MARTHA), limiting access to a larger international community. Others are proprietary (FLUKA, PENELOPE), limiting transparency regarding underlying methods. Furthermore, certain tools are only designed for specific energy ranges (MCSHAPE and SIMSPEC-G). The two related open-source codes, EGS5 and EGSnrc, originated in accelerator physics and cannot model neutrons. Consequently, they cannot be used in nuclear engineering. GEANT4 is open source but targets the user group of high-energy physicists and is significantly slower than other codes. For example, simulation of a gamma spectrum as shown in Figure 4.5 with 10^6 particles took 5.40 seconds with OpenMC and 44.60 seconds with Geant4-11.1.2 (running on a single *AMD Ryzen 7 PRO 6850U* core, excluding compilation time and averaging over 100 individual runs).
Interest in such functionality exists within the OpenMC user community. For example, El-Bouzaidi et al. [131] describe simulations (without providing any code) to determine the response function of a sodium-iodide (NaI) detector with OpenMC. Albeit in principle similar to a PHT, the method lacks the proper accounting for particles undergoing software-based energy cutoff, leading to erroneous results (for example, reflected in the observable differences in the iodine-escape peaks in Figure 5 of their publication).

Implementation

To determine the Pulse-Height Tally value, it is crucial to maintain a record of the overall energy deposited in a specified volume by both the incident photon and secondary particles generated through interactions with the detector material (e.g., photoelectric effect). Figure 4.1 illustrates four particle tracks: Particle I does not interact with the detector volume, leading to a PHT value of zero. The PHT value for particle II can be obtained by summing up the energies lost during three scattering interactions. Particle III is fully absorbed in the volume through the photoelectric effect, resulting in the PHT value reflecting the particle's total energy. Particle IV's PHT value is determined by considering only the energies lost during two scattering reactions within the volume.

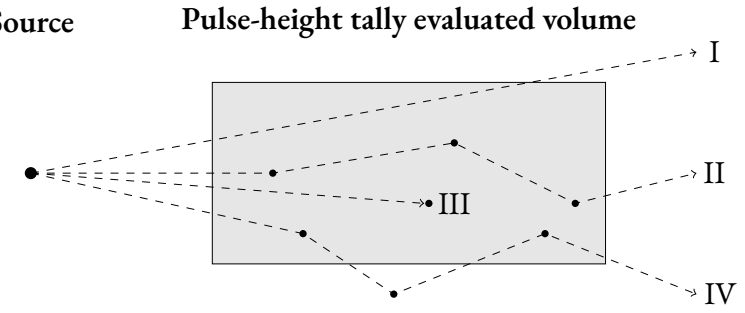

Figure 4.1: Illustrative Particle Histories for the Pulse-Height Tally
Points indicate the locations of interactions, and dashed lines represent the particle tracks.

Solving the neutron transport equations or using tallies in Monte Carlo Particle Transport simulations are two distinct approaches to studying particle transport (Section 3.3). Most unknown properties of a system can be determined by both of these approaches [132, 133]. Typically, such tallies can be determined on the fly by counting each reaction separately, regardless of the interacting particle's previous or subsequent interactions. However, pulse-height tallies are non-Boltzmann tallies, meaning their value can not be obtained by solving the neutron transport equations. The value of the PHT depends on the effects of multiple interactions, including different particles (e.g., pair production), necessitating more advanced implementation methods. Before evaluating the PHT value, it is necessary to simulate the entire history of the particle.

The capability to record energy deposited by individual particle interactions in a specific volume was enabled by introducing a new method to the `OpenMC::particle` class within OpenMC's object-oriented framework. This method allows for determining energy deposited by photons, which occurs through one of three primary interactions: Incoherent (Compton) scattering, photoelectric effect, or pair production. In addition to these interactions, the method accounts for any secondary photons generated and subtracts their energy from the PHT value. The interaction of photons with nuclides may also generate electrons or positrons as secondary particles. OpenMC is not capable of modeling these particles but employs the following approximations: First, two isotropic 511 keV annihilation photons in opposite directions are modeled instead of positrons. Second, for electrons, a thick-target bremsstrahlung approximation is used, where electrons are not transported but instead instantly generate bremsstrahlung photons [134]. The alternative OpenMC offers for electrons, where all energy is deposited at the point of particle creation, is not used here. Third, additional photons are produced in the process of atomic relaxation.

In OpenMC (like in most other Monte-Carlo particle transport codes, for example, EGSnrc, FLUKA, Geant4, MCNP, and Penelope), the cross-section data provided for photon interaction assumes interaction with cold, neutral, and isolated atoms [135]. The density-weighted sum of the cross-sections of the individual elements approximates cross-sections for materials consisting of different elements. OpenMC photon interaction is modeled for energies down to 1 keV, and it terminates transport for photons with lower energies [134] (the manual of MCNP 6.2 also describes a default cutoff value of 1 keV [97]). Treatment for lower energies is complex, as the interactions depend on element properties and are influenced by other effects like the molecular structure of a material. I ensure proper accounting for particles below the cutoff value by adding the remaining energy to the PHT value of the volume in which their transport simulation is terminated.

An analytical validation, a software-based validation, and a comparison to experimental data have been performed to ensure the accuracy of the implementation.

Analytic Validation*

The results of the PHT can be determined analytically in simplified physical models, of which two are described in [137]. MCNP developers used this validation method for their PHT functionality [138]. Two publications with similar author groups give different PHT results for these simplified models [138, 139]. The newer publication [138] contains values inconsistent with the previous publication for the simpler model. Very likely, the same source of inconsistency applies to the more complex model; hence, I provide new results here. I performed an analytical validation of the most complex scenario described in [138], the two-region detector (see Figure 4.2).

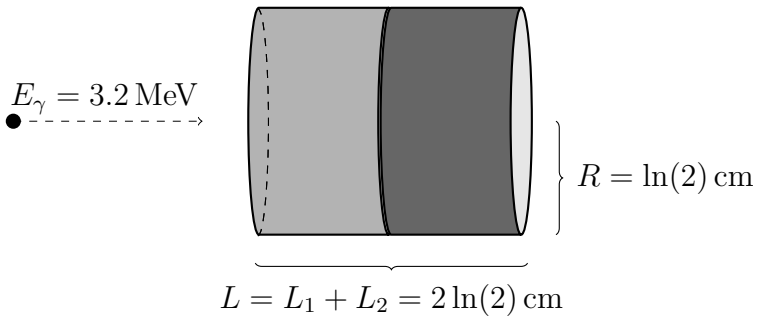

Figure 4.2: Two-Region Detector for Analytical Pulse-Height Tally Validation
The pulse-height is determined in the second cylinder.

In the design, two cylindrical volumes, each having a length and radius of $\ln(2)\,\mathrm{cm}$, are aligned sequentially. These cylinders are composed of three hypothetical elements: Kneeon (50%), Moron (20%), and Odium (30%). These hypothetical elements represent simplified versions of pair production, photoelectric absorption, and Compton scattering interactions. Specifically, during the simplified pair production process, two photons are generated, each carrying a quarter of the energy of the incoming photon. If the energy of the incoming photon exceeds 1.0 MeV, one of the photons generated in the simplified pair production is scattered at an angle of ninety degrees. In the case of simplified Compton scattering, the photon loses half of its energy but maintains its original direction. For the simplified model of the photoelectric effect, the incoming particle is absorbed. The starting photons have an initial energy of 3.2 MeV, and move towards the first cylinder. They are absorbed within the volume once their energy drops below the 0.15 MeV threshold. The material of the cylinders possesses a total macroscopic cross-section of $1\,\mathrm{cm}^{-1}$. After the photons pass the first cylindrical volume, their pulse-height is determined in the second cylinder (marked in darker gray in Figure 4.2). This scenario leads

*Parts of this subsubsection are based on the following bachelor's thesis, which I co-supervised with Prof. Dr. Malte Göttsche, and have been further expanded here:

- M. Miah. "Analytical Validation of the Pulse Height Tally". RWTH Aachen, 2022. URL: https://www.nvd.rwth-aachen.de/global/show_document.asp?id=aaaaaaaabkgyonx (visited on 03/03/2025)

Energy [MeV]	Analytic PHT result	Energy [MeV]	Analytic PHT result	Energy [MeV]	Analytic PHT result
0.0	0.561329	1.2	0.013011	2.6	0.005003
0.2	0.023769	1.4	0.002189	2.8	0.012088
0.4	0.063021	1.6	0.109465	3.0	0.002873
0.6	0.019769	2.0	0.030379	3.2	0.057493
0.8	0.049945	2.2	0.012559		
1.0	0.002810	2.4	0.034298		

Table 4.1: Analytic Determined Pulse-Height Tally Results for Validation
The analytic results for the sixteen different energies that the PHT can take in the two-region setup.

to 500 different particle histories, in which the PHT can take sixteen different values. The exact values are given in Table 4.1.

Software-based Validation

I modified the OpenMC source code to model the simplified photon reactions for validation. I ran an OpenMC simulation with 100 sub-samples of 10^7 particles each. Figure 4.3 shows the simulated and analytically derived results and the residuals with corresponding error bars. The simulated results agree with the expected analytical outcome within the statistical uncertainties. The results of OpenMC 0.12.2 [91] and MCNP 6.2 [97] simulations with identical parameters were compared in the software-based validation.[10] The detector design is derived from Mirion Technology's NaI-based "802 Scintillation Detector" [140] (cf. Figure 4.4). In the following, I modeled the back of the detector as a homogeneous aluminum block [129, 141]. This material has a negligible impact on the final PHT outcome, as demonstrated by simulation results. All simulations were performed using the Electron Photon Relaxation Data 2014 (EPRDATA14) to model photon-related interactions. EPRDATA14 is an ACE data format for MCNP 6.2, based on the IAEA's Electron Photon Interaction Cross Sections (EPICS) 2014 [142]. OpenMC data libraries are provided in HDF5 format based on standard neutron-cross-section evaluations. I use the OpenMC library ENDF/B-VII.1 from a set of Los Alamos National Laboratory-based data libraries. This library includes the EPRDATA14 for photon interactions [143]. Both codes ran with an energy cutoff value of 1 keV and similarly modeled the relevant physical interactions. Photons are started uniformly across a disc, situated 10 cm in front of the detector, and are projected directly towards the detector in a perpendicular orientation. Since the initiated photons hit the entire detector front uniformly, only 82 percent of the starting photons will hit the detector's active volume. After interacting with the casing, a fraction of the photons missing the detector are scattered back into the crystal. In MCNP, non-analog processes like knock-on electrons can generate negative PHT scores. Particles that pass through the observed volume contribute an artificial value of 10^{-12} MeV to the PHT. Therefore, it is recommended to run MCNP with a zero bin and an additional epsilon bin at 10^{-5} MeV to account for both effects separately. In OpenMC, particles that do not pass

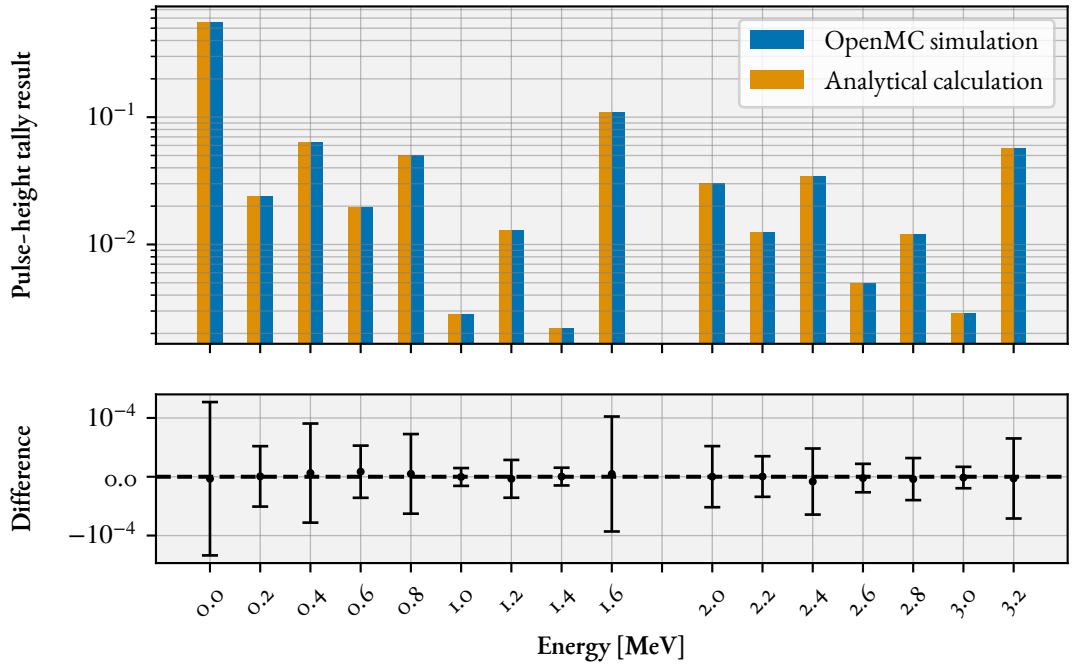

Figure 4.3: Comparison of OpenMC-simulated and Analytical PHT Results
The upper figure shows a comparison of the OpenMC-simulated and analytically determined PHT results. The lower figure illustrates the disparity between the two outcomes. Error bars show the standard deviation of 100 sub-samples with 10^7 particles each per data point. Residuals are correlated.

through the volume do not contribute to the PHT. I ignore results from these first two bins, as they have no physical equivalent. Furthermore, in OpenMC, PHT values on the upper boundary of a bin are not counted in that bin, while this is the case in MCNP. Therefore, I have chosen the bins such that the epsilon bin is followed by 2048 equally sized bins, where the full-energy peak lies precisely in the middle of the uppermost bin. I have shifted the OpenMC bins by 10^{-12} MeV to reduce the chance of other peaks falling precisely on the boundary. With an additional bin up to 20 MeV, I checked that no unexpected counts of higher energies occurred. I utilized the pulse-height functionality to simulate the measurement of this detector with various photon sources and subsequently compared the obtained results.

Caesium-137 spectrum Figure 4.5 shows simulation results for the scintillation detector described above with a starting photon energy of 0.6617 MeV (caesium-137). Each simulation included 10^{10} starting particles. The plot shows various characteristics, such as the full-energy peak (0.6617 MeV), the Compton edge (0.478 MeV), and the backscatter peak (0.184 MeV). At 33.2 keV (zoomed in), the K-edge of iodine can be seen. The sudden rise in the likelihood of

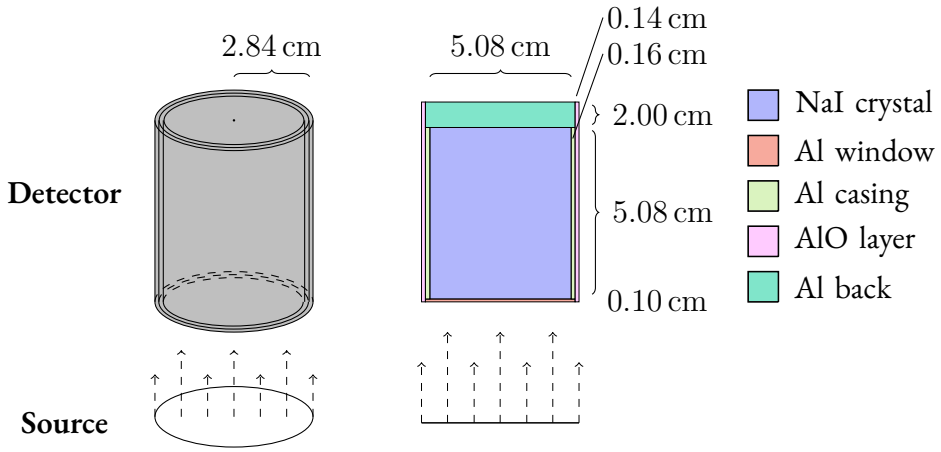

Figure 4.4: Model of the "802 Scintillation Detector" by Mirion Technology
The 2×2 inch NaI scintillation detector model employed for simulations in both OpenMC 0.12.2 and MCNP 6.2.

photoelectric absorption corresponds to the binding energy of an iodine K-shell electron. This electron absorbs the energy of the photon during the absorption process. The two peaks next to each other (at 0.633 MeV) are the result of a photoelectric absorption and the subsequent escape of the K_α- (28 keV) or K_β-X-rays (31 keV) [83]. These characteristic X-rays are created when the vacancy in the inner K-shell is filled with an electron from the L- or the M-shell after the photoelectric absorption. Further, the differences between the escape of the $K_{\alpha,1}$ and the $K_{\alpha,2}$-X-rays or the $K_{\beta,1}$- and $K_{\beta,2}$-X-rays can be seen. The two tiny peaks in the Compton valley at 0.602 MeV (zoomed in) result from a double escape of the K_α- and K_β-X-rays. After the electron is emitted from the K-shell in the initial photoelectric absorption, the thick-target bremsstrahlung approximation is used to determine which photons are produced by the deceleration of the electron. These photons can have an energy higher than 33.2 keV and potentially lead to secondary photoelectric absorptions emitting K_α and K_β-X-rays, able to escape again. The two peaks are the result of two K_α-X-rays or one K_α- and one K_β-X-ray. As the probability for a K_β X-ray escape is much lower than a K_α X-ray escape, the peak of the double K_β X-ray escape remains, because of its statistical improbability, undetectable. If only the crystal without surrounding material is simulated, the third peak becomes visible. The small, broadened peak to the right of the full-energy peak results from the escape of the L_α-X-rays after photoelectric absorption.

The relative error is displayed in the lower part of Figure 4.5. The most significant differences are discernible for very low energies near the iodine K-edge and the bins directly to the left of the full-energy peak. Despite these variations, the two spectra are close to identical. The two spectra's full-energy peak height differs by less than 0.05%.

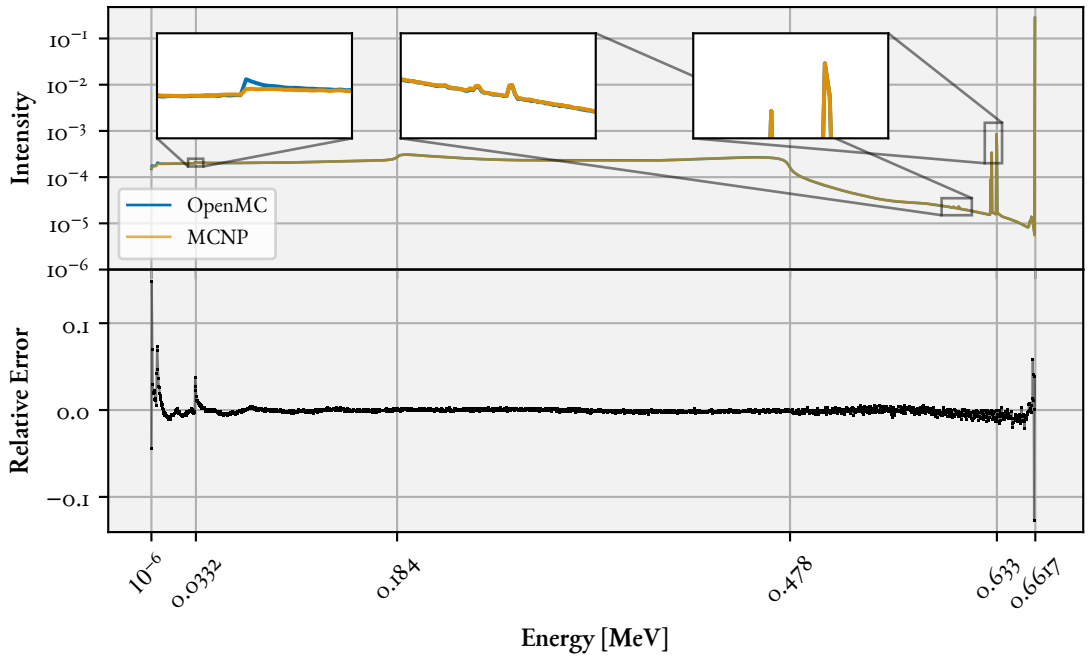

Figure 4.5: Pulse-Height Tally Results in OpenMC and MCNP for a Caesium-137 Source
The top plot displays the simulation results of measuring a caesium-137 gamma spectrum using a pulse-height tally in both OpenMC and MCNP 6.2. The lower plot illustrates the relative error in these simulations.

Comparing various energies 295 simulations for photons with incoming energies ranging from 0.05 MeV to 3 MeV, in increments of 10 keV were conducted. Each simulation results in an individual spectrum with 2048 energy bins analogous to the caesium-137 spectrum described above. The simulations involved 10^8 initial particles for each run. The Kolmogorov-Smirnov test was employed between all 295 energy levels for each pair of OpenMC and MCNP 6.2 simulations (compare Equation 3.6).
The gamma spectra derived from the simulations were normalized to one, and the first energy bin's results were excluded to prevent double-counting. The first bin includes the number of particles that did not interact with the detector, which has no physical measurement equivalent. With $n_1 = n_2 = 2047$ and a significance level of $\alpha = 0.05$, the threshold value is $d_\alpha = 0.03$. For very small energies, the spectra differ more than for higher energies — yet they are well below the significance level of the Kolmogorov-Smirnov test. For most photon energies, the resulting spectra are highly similar (low Kolmogorov-Smirnov test results). Initially, exceptions were visible for the energies of 1.45, 1.69, 1.93, 2.41, 2.68, and 2.84 MeV (shown in red in Figure 4.6). Further investigation showed that a software error likely causes these differences in MCNP 6.2 (probably a limitation by the precision of stored values within MCNP). In

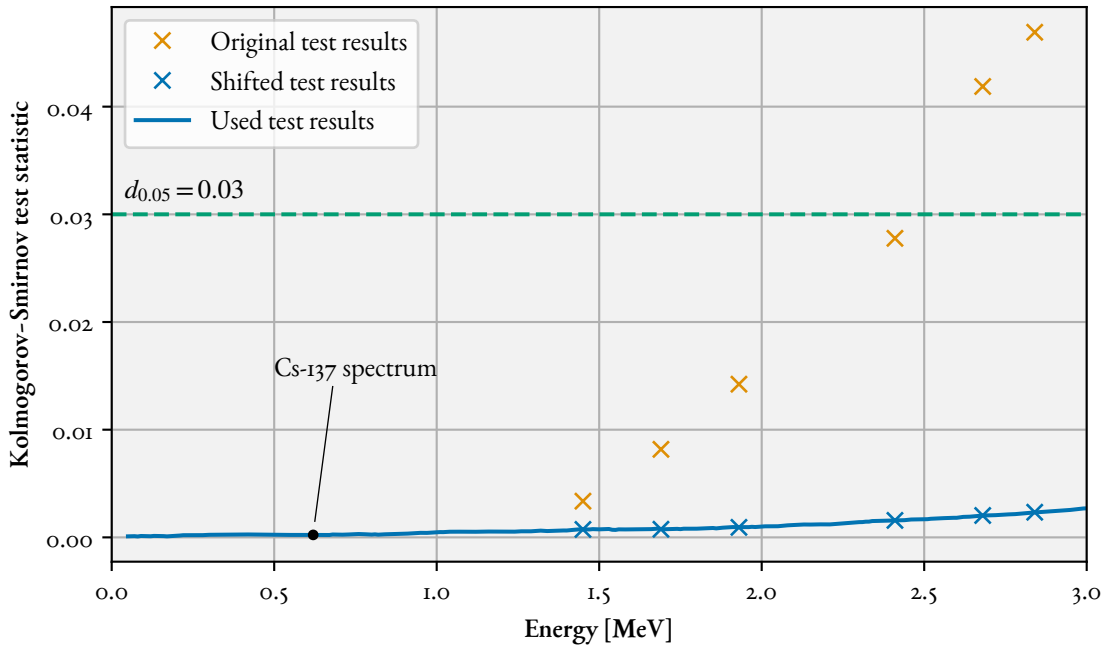

Figure 4.6: Comprehensive Pulse-Height Tally Comparisons in OpenMC and MCNP A comparison of 295 spectra within the 0.05 MeV to 3 MeV energy range, generated by OpenMC and MCNP 6.2, using the Kolmogorov-Smirnov test to determine if the simulation results conform to the same underlying probability distribution. The results are consistent at a significance level of $\alpha = 0.05$ if the test outcome is below the threshold value d_α. Results are plotted as a line to improve visibility. Initially, MCNP 6.2 pulse-height tally results for 1.45, 1.69, 1.93, 2.41, 2.68, and 2.84 MeV showed large discrepancies because some events were sorted in incorrect bins (orange). Using minimally shifted energy bins (20 eV), results improve significantly (blue).

each case, only two energy bins contained significantly different values because specific peaks (single-escape, double-escape, or photon annihilation peaks) were registered in the wrong bin. This was when the peak's energy was within 10 eV of a bin border. Therefore, I repeated the simulations with bin borders shifted by 20 eV, which solves the issue (shown in blue in Figure 4.6).
Results indicate an agreement between the newly implemented PHT in OpenMC and the tally functionalities of MCNP 6.2.

Experimental validation

A comprehensive set of experimental measurements using a 3 × 3 inch NaI scintillation detector for different isotopic sources can be found in [145]. The PHT functionality of OpenMC

was used to simulate these measurements. The detector was conceptualized as a sodium iodide cylinder with thin layers of aluminum oxide and pure aluminum. An iron block was used to model the detector's back. As there are no specific details on the source and background given, I assume point sources and neglect the background. As a result, the subsequent findings are primarily a qualitative comparison.

The effect of diverse physical phenomena, including charge collection statistics, electronic noise, and spatial variations in the detector response across its active volume, results in the broadening of peaks in experimental gamma spectra, rather than the appearance of narrow lines [83]. When the energies of incoming photons are very close, the detector may register them as a single peak. This is described by the energy resolution of a detector, which characterizes its ability to differentiate closely spaced peaks. For a specific energy, the detector's resolution is defined as the ratio of the full width at half maximum (FWHM) of the full-energy peak to its energy. The standard deviation $\sigma(E)$ of the approximating distribution, for a given energy E, is by

$$\sigma(E) = \frac{\mathrm{FWHM}(E)}{2\sqrt{2\ln 2}} \tag{4.2}$$

is related to the FWHM of a peak with a specific energy. To determine the energy-dependent resolution of the detector, I perform a fit of the measured resolutions read manually from Figure 6 in [145] to the function

$$R(E) = \frac{\mathrm{FWHM}(E)}{E} = \frac{a + b\sqrt{E + cE^2}}{E} \tag{4.3}$$

Figure 4.7 displays both the individual values and the fit, employing the parameters $a = -0.643\,\mathrm{MeV}$, $b = 6.794\,\mathrm{MeV}^{0.5}$ and $c = 0.258\,\mathrm{MeV}^{-1}$, with a mean squared error of the fitting of 0.219. The figure also shows detector resolutions calculated from the nine experiments presented below. The spectra I analyzed have, on average, a slightly worse resolution than the nuclides used to determine the detector's resolution.

I applied Gaussian broadening on the PHT results in the experimental simulation through an additional Python function to mimic the characteristics observed in real experimental measurements [83]. Figure 4.8 illustrates nine experimental measurements and their corresponding simulated spectra, with vertical lines indicating the sources of photon energies. The total number of emitted photons of the respective source is given in [145].

No absolute source activity was given for some experimental spectra, marked in Figure 4.8. For comparison, the simulation results were normalized based on the total counts of the experiment. The detector efficiency provided in [145] was utilized for other experiments to calculate the total number of simulated particles. For each nuclide, the efficiency of the full-energy peak was employed.

Some experimental spectra did not align precisely with the anticipated source energies, differing by one energy bin. For the plots shown in the figure, the data was shifted. For zinc-65, an additional peak at 511 keV created by the annihilation of positrons produced in the β^+ decay

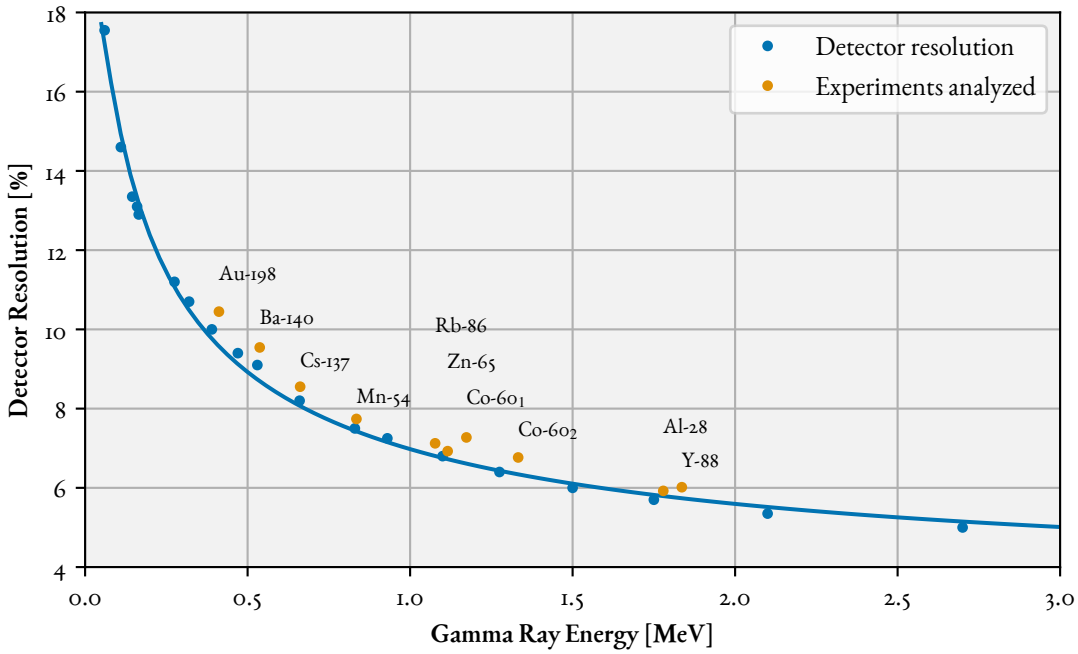

Figure 4.7: Determination of the Detector Resolution
Blue dots show the values given in [145]. The blue line corresponds to the fit parameters detailed in the text, while the orange dots represent the resolution for the experimental spectra under consideration.

can be seen [146]. Since OpenMC does not simulate this decay, I initiated an additional 511 keV photons according to the intensity of the β^+ decay.
The simulation results generally agree well with the experimental gamma spectra for energies below 1 MeV. The simulation spectra are broadened too much for the higher energy range, consistent with the fit in Figure 4.7. The X-ray peaks generated by surrounding materials can be seen in the low-energy regions of the spectra of yttrium-88, zinc-65, and caesium-137. Since I only simulate a simple detector setup, these are not reproduced in the simulation results. I suspect gold-198 was mixed with its metastable isomer in the experiments, producing a gamma peak at 97 keV. In the case of aluminum-28 and rubidium-86, I suspect some detector malfunction, like electronic noise in the lower energy region of the detector. A discrepancy is also evident in the cobalt-60 spectrum. The experimental data includes the summation peak of both photon energies, 1.17 MeV and 1.33 MeV. After the β^- decay, two photons with these energies are emitted within picoseconds. A summation event occurs if the detector absorbs both photons. I have included the sum of the two energies in the figure as a purple dashed line. To simulate such effects with OpenMC (or MCNP), the software would need to initiate several photons for the same particle history. Both codes, however, lack such functionality. Two solutions could be implemented to achieve the summation peak. First, simulation

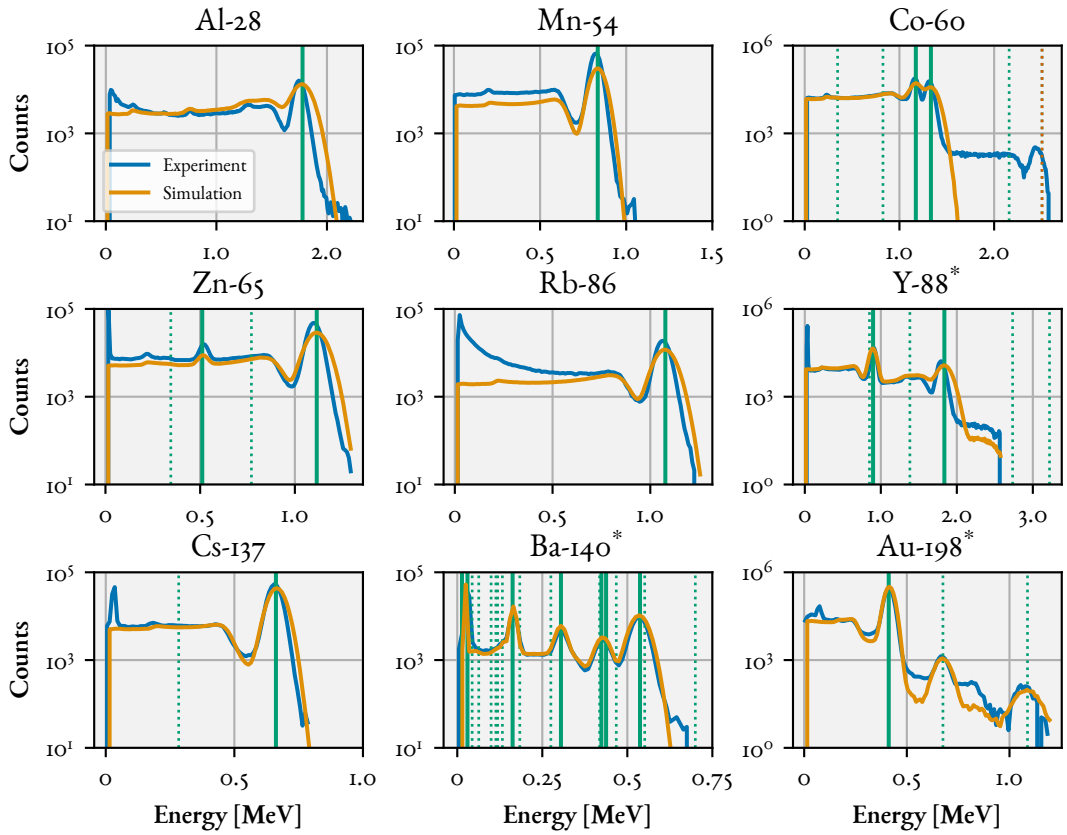

Figure 4.8: Comparison of Experimental and Simulated Gamma Spectra
Incorporate energy broadening according to the detector resolution. The energies of the initial source photons are indicated by green vertical lines, with dotted lines representing energy levels contributing less than one percent to the total intensity.
* simulated spectrum has been normalized with the total counts of the experiment

results of individual particles are combined through post-processing after the Monte Carlo simulation. The publication [147] demonstrates this for MCNP; a similar approach could be taken for OpenMC calculations. Secondly, the software itself could be modified. In OpenMC, the `secondary_bank` could start a second photon with an initial particle. Both solutions are outside the scope of this article, as its primary focus is validating the Pulse-Height Tally (PHT).[11]

Notes

[1]The deployed Fat Man model had a criticality of $k_{\text{eff}} = 0.97$ [99]. Each neutron produces, on average, 0.97 additional neutrons, leading to a chain reaction. The total neutrons produced per initial neutron is:

$$\text{Total neutrons} = 0.97 + 0.97^2 + 0.97^3 + \ldots = \frac{1}{1 - 0.97} - 1 = 32.$$

The equation is simplified using the geometric series. The most spontaneous fission events are caused by plutonium-240 with a multiplicity of 2.16 [78]. Thus, each plutonium-240 spontaneous fission generates $2.16 \cdot 32 = 69.12$ neutrons. The most fission events will be induced in plutonium-239. Plutonium-239 has a fast fission (2 MeV) multiplicity of 3.16 [78]. Therefore, each plutonium-240 spontaneous fission induces approximately $^{69.12}/_{3.16} = 21.87$ fast fissions in plutonium-239.

[2]ONIX also provides JEFF-based decay chains.

[3]In the Nuclear Wallet Card's eighth edition, all nuclides with a half-life of greater or equal to 0.1 s and some with a half-life greater or equal to 1 ms, which decay by spontaneous fission, α-decay or proton emission are included, resulting in data of 6,251 radioactive decays and transitions.

[4]When the spontaneous fission branching ratio is given as an upper limit, I assume the stated threshold. For example, if the value is given as $< 10^{-12}$, I take it as 10^{-12}.

[5]Neutron induced fission yields: Th-227, Th-229, Th-232, Pa-231, U-232, U-233, U-234, U-235, U-236, U-237, U-238, Np-237, Np-238, Pu-238, Pu-239, Pu-240, Pu-241, Pu-242, Am-241, Am-242*, Am-243, Cm-242, Cm-243, Cm-244, Cm-245, Cm-246, Cm-248, Cf-249, Cf-251, Es-254, and Fm-255. Spontaneous fission yields: U-238, Cm-244, Cm-246, Cm-248, Cf-250, Cf-252, Es-253, Fm-254, Fm-256.

[6]For neutron-induced fission, yields are generally provided for thermal, fast, and DT-fission (fission by 14.1 MeV neutrons). If only one set of fission yields is given, these fission yields are taken for all incoming neutron energies.

[7]The molecular properties in which a nuclide is present determine the possibility of how a nucleus can interact with its shell electrons and, by this, the probabilities of some decays and transitions as well as the half-life [148]. This minor effect is not considered in the following.

[8]If the difference between the Q-value and the decay energy is more minor than 0.1% from a child's energy level, I assume a rounding error and take the closer, but slightly higher energy level.

[9]The module is slower than ONIX because its decay chains, including spontaneous fissions, involve thousands more nuclides. However, when spontaneous and induced fission are not considered, the decay module runs approximately 30 times faster than ONIX. This comparison is based on execution using a single *AMD Ryzen 7 PRO 6850U* core, averaged over 100 individual runs.

[10]I only wrote the input files of the MCNP simulations; Dr. Moritz Kütt ran the MCNP simulations on his local computer.

[11]All input files, results of the simulations, and scripts for creating the plots are available on GitHub: https://github.com/cfichtlscherer/Implementation_and_Validation_of_the_Pulse-Height_Tally_in_OpenMC_Code

This page intentionally blank

Chapter 5

Defining Weapon Baseline Emissions

Nuclear weapon designs remain classified, with no official emission models or benchmarks publicly available. The notional models presented in this chapter are derived from an extensive literature review, including declassified documents from nuclear-armed states and former nuclear weapon aspirants (such as Sweden and Switzerland), U.S. weapons laboratory reports, and open-source information.
The passive radiation signatures of nuclear weapons result from the interplay between radiating and non-radiating materials and their geometric arrangements. Therefore, this chapter begins by describing the different warhead components and their materials, followed by their major photon emissions and the corresponding absorption rates in different warhead materials. Then I introduce eight theoretical emission models.

5.1 Nuclear Weapon Materials and Components*

5.1.1 Fissile Material of the Primary — Plutonium

In a nuclear weapon's primary, an exponentially growing fast fission chain reaction produces a vast amount of energy within approximately one microsecond. Several fissile materials could be used for such a chain reaction. The most common are the nuclides uranium-235 and plutonium-239, with the latter being superior due to its higher fission cross-sections, especially for fast neutrons, and its higher multiplicity, illustrated in its smaller critical mass. Plutonium is used in its metallic state, where it can manifest in six primary allotropes. The monoclinic crystal structure (α-phase) is the densest and is stable at room temperature. Several publications assume that weapons use α-phase plutonium (see for example [25, 81, 149]). Still, I assume

*Parts of this section are based on the following publication, which primarily builds upon my own work and has been further expanded here:

- **C. Fichtlscherer**, M. Kütt. "Uniqueness, Reproducibility and Discrimination of Nuclear Warhead Gamma Signatures". In: *Science & Global Security* 32.1–3 (2024). DOI: 10.1080/08929882.2024.2387966

it is used in its δ-phase, as the US declassified the "*mere fact that delta phase [plutonium] has been or is used in weapons*" [58]. While the "pure" δ-phase forms only at higher pressures and temperatures, it can be stabilized at room temperature with alloying elements like gallium.[1] The δ-phase offers several advantages: it is more malleable and ductile compared to the brittle α-phase, eliminates the issue of dramatic shrinkage during cooling in the manufacturing process — as the α-phase has a 20% higher density than the δ-phase — and avoids many phase transitions when heated and compressed during implosion. As described in [99], when the δ-phase is compressed during the implosion, it transitions into α-phase and instantly melts to a liquid state.

In 1996, the US declassified the use of up to 1% gallium as an alloying element in plutonium pits [150]. Here it is assumed that 0.8 wt% gallium — the same amount used in the U.S. implosion weapon Fat Man in 1945 [151] — stabilizes plutonium in the δ-phase. This proportion is also confirmed in other studies [99, 152]. Additionally, this aligns with the 3 at% gallium density noted in [153]. δ-phase plutonium has a density of 15.92 $\mathrm{g/cm^3}$ [152], gallium-stabilized δ-phase plutonium has a density of 15.76 $\mathrm{g/cm^3}$ [154]. I assume gallium is used in its natural isotopic composition, with 60.108 at% for gallium-69 and 39.892 at% for gallium-71.

Since all plutonium isotopes have half-lives that are considerably shorter than the Earth's age, any plutonium generated during the planet's formation has entirely decayed. Consequently, the entire global stock of 560 metric tons of separated plutonium is artificially produced [155].[2] Plutonium is produced in reactors by the neutron capture of uranium-238 and two subsequent β^- decays. For weapons purposes, minimizing the concentration of even-numbered plutonium isotopes is crucial due to their high spontaneous fission rates, which produce an undesirable neutron background. Technically, this is achieved by aiming for a very high plutonium-239 concentration. By the U.S. Department of Energy (DOE) definition, weapon-grade plutonium (WGPu) contains at least 93% plutonium-239 [156]. Plutonium with less plutonium-239 content is considered reactor-grade plutonium (RGPu). However, reactor-grade plutonium can also be used for nuclear weapons. In 1977, the US declassified information about a successful nuclear weapon test using reactor-grade plutonium in 1962 [58]. Carson Mark, former director of the nuclear-weapon-design division at the U.S. Los Alamos National Laboratory, further discussed this issue [157]. Yet the IAEA considers all plutonium as direct use material, meaning "*that [it] can be used for the manufacture of nuclear explosive devices without transmutation or further enrichment,*" with the specified exception of plutonium containing more than 80% of plutonium-238 [158].

The following simulations use the isotopic composition of the so-called "DOE 3013 weapon-grade plutonium" provided by a material compendium of the Pacific Northwest National Laboratory [159].[3] The photon and neutron production rates of the different plutonium isotopes, including americium-241, are given in Table 5.1.

The impact of plutonium aging on the weapon's performance is an ongoing debate. Two factors could affect the weapon's performance: the increased concentration of americium-241, a decay product of plutonium-241, raises the neutron background and heightens the risk

	Neutron production [$10^4\,\mathrm{kg}^{-1}\mathrm{s}^{-1}$]	Photon production [$10^9\,\mathrm{kg}^{-1}\mathrm{s}^{-1}$]
Plutonium-238	263.0000	53.55
Plutonium-239	0.0020	1.35
Plutonium-240	103.1000	0.65
Plutonium-241	0.0002	55.30
Plutonium-242	172.2000	0.04
Americium-241	0.1500	45,648.19

Table 5.1: Plutonium Isotopes Photon- and Neutron Production Rates
Americium-241, as an important decay product of plutonium-241, is included. The values have been determined using the `NNDCDecay` module. The photon particle production rates include only photons, with an energy above 50 keV. The neutron production rate includes only neutrons from spontaneous fission.

of the primary's premature ignition. The second concern involves the helium produced by alpha-decay within the WGPu, potentially causing swelling, microcracks, or crystal structure defects [160]. The amount of helium produced in 50 years in one cubic centimeter WGPu would fill two cubic centimeters at standard temperature and pressure.[4]

The composition of the plutonium vectors of different ages, obtained via decay calculations, and respective photon and neutron production rates, are given in Table 5.2.[5]

For starting the nuclear explosion, the plutonium in the primary is brought into a supercritical state to initiate the fast nuclear chain reaction — achieving a criticality greater than one. The *criticality*, also called the *effective neutron multiplication factor* k_{eff}, is the ratio of the gain to the loss of free neutrons in a generation. It provides a time-independent measure of the system's free neutron number evolution. From a historical context, there are two different definitions of criticality depending on whether neutrons from (n, Xn)-reactions are included in the neutron gain [161]. I include the neutron gain of (n, Xn)-reactions in the following. Additionally, because the evolution of a supercritical nuclear chain reaction is rapid, delayed neutrons are typically neglected [58] — leading to the concept of the *prompt criticality*[6]

$$\begin{aligned} k_{\text{prompt}} &= \frac{\text{prompt neutron gain}}{\text{prompt neutron loss}} \\ &= \frac{\text{prompt neutrons created in fission + neutrons created in } (\mathrm{n}_{\text{prompt}},\mathrm{Xn})\text{-reactions}}{\text{prompt neutrons absorbed + prompt neutrons escaped}}. \end{aligned}$$

There are three methods of bringing the plutonium in a supercritical state. In the gun-type design, one subcritical mass is shot into another to become supercritical.[7] In the implosion design, a subcritical mass is compressed. The third method is the autocatalytic method, in which supercriticality is achieved by compressing or expelling a neutron absorber like boron-10 [162, 163]. Modern nuclear weapons are based on the implosion design.[8] In Figure 5.1, the

	0 a	10 a	20 a	30 a	40 a	50 a
Plutonium-238 [wt%]	0.050	0.046	0.042	0.039	0.036	0.033
Plutonium-239 [wt%]	92.752	92.725	92.699	92.672	92.645	92.619
Plutonium-240 [wt%]	5.952	5.946	5.939	5.933	5.927	5.921
Plutonium-241 [wt%]	0.397	0.244	0.151	0.093	0.057	0.035
Plutonium-242 [wt%]	0.050	0.050	0.050	0.050	0.050	0.050
Americium-241 [wt%]	0.000	0.151	0.242	0.295	0.326	0.342
Gallium-69 [wt%]	0.475	0.475	0.475	0.475	0.475	0.475
Gallium-71 [wt%]	0.325	0.325	0.325	0.325	0.325	0.325
Neutron production [$10^4\,\mathrm{kg}^{-1}\mathrm{s}^{-1}$]	6.35	6.34	6.32	6.31	6.29	6.28
Photon production [$10^9\,\mathrm{kg}^{-1}\mathrm{s}^{-1}$]	1.54	70.69	111.92	136.23	150.15	157.67

Table 5.2: WGPu's Composition, Photon- and Neutron Production Rates
The composition, photon- and neutron production rates of 0.8 wt%-gallium-stabilized δ-phase plutonium with the isotopic composition as given in [159]. The values have been determined using the `NNDCDecay` module. The photon particle production rates include only photons with an energy above 50 keV. The neutron production rate includes only neutrons from spontaneous fission. Older compositions were determined by calculating the decay of respective nuclides.

prompt-criticality of a bare WGPu sphere of different masses and densities (compression levels) is shown. Note that for a weapon, criticality must significantly exceed one. For instance, in the theoretical model of Fat Man, a maximum criticality of 1.51 was achieved [99]. Figure 5.1 demonstrates how criticality depends on mass and compression strength. Neutron reflectors, discussed in the next section, can significantly increase the criticality, thereby lowering the amount of fissile material required to achieve a specific criticality.

In deployed weapons the WGPu takes the form of a pit. Following the definition of the Los Alamos National Laboratory, "*a pit is a hollow sphere of plutonium that, when uniformly compressed by explosives inside a warhead or bomb, causes a nuclear explosion*" [164].[9]

In modern warheads, plutonium is compressed by a factor of three to four [58].[10] To maximize the weapon's yield, one wants to start the fission chain reaction, when the assembly reached the state of maximum criticality, so when the plutonium is compressed to its maximum, a neutron generator produces a pulse of neutrons to start the nuclear chain reaction. According to [165], the "*probability that a nuclear weapon would work without the [neutron generator] is low*". At the beginning of the Manhattan Project, Polonium-210–Beryllium-9 sources were used. They were placed in a small void inside the plutonium pit and would generate a great number of (α, n)-neutrons when compressed [58]. Following [151] there was a standard initiator having a radius of 1.016 cm. This modulated neutron initiator presents the challenges of the short half-life of polonium-210 and the issue of neutrons being generated slightly before the plutonium is fully compressed, leading to preignition and reduced yield [166]. Modern

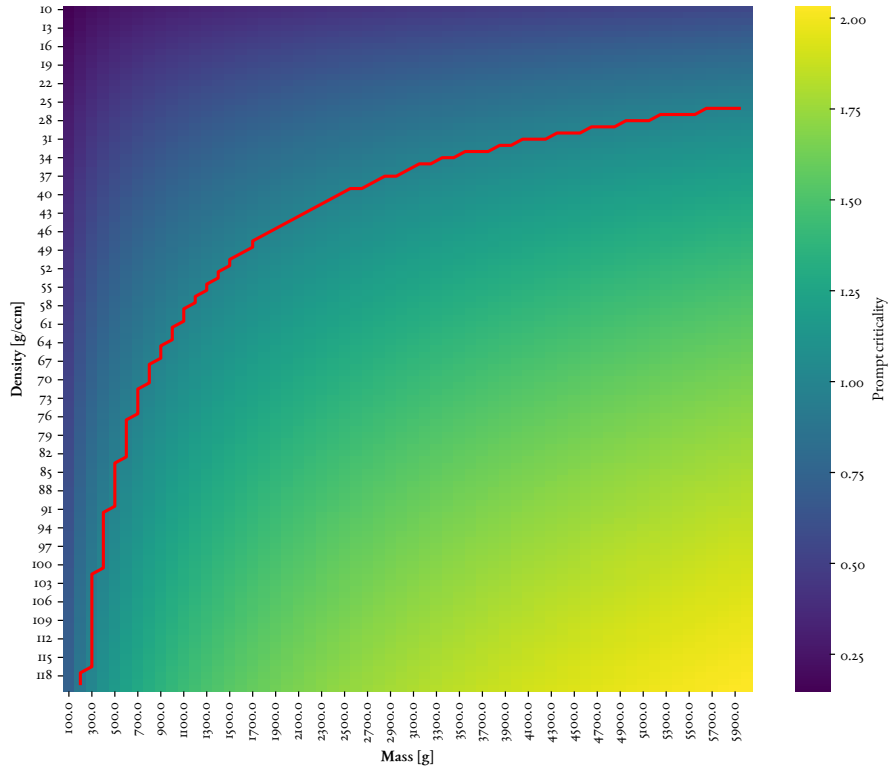

Figure 5.1: Prompt Criticality of a Bare Plutonium Sphere
The prompt criticality of a bare sphere of plutonium of different masses and densities has been determined using OpenMC simulations. The red line represents the criticality of 1.0.

weapons likely employ solid-state neutron generators (linear particle accelerators) outside the fission assembly producing neutrons through DT fusion [58].[11]

5.1.2 Uranium Components

Nuclear warheads feature several uranium components with varying levels of enrichment. In the following, I assume that the components from natural uranium (NU) contain 0.711 wt% uranium-235, the components from depleted uranium (DU) only 0.2 wt%, and the highly enriched uranium (HEU) components, 95.0 wt%.[12] The rest is almost entirely uranium-238. Uranium-238 decays via the short-lived thorium-234, protactinium-234, and protactinium-234* to the long-lived uranium-234. Similarly, uranium-235 decays via the short-lived thorium-231 to protactinium-231. Given that the nuclides before the two "breaks" (uranium-234 and protactinium-231) in the decay chain have short half-lives, the emissions from these materials

can be considered constant for the periods of concern. In the following I assume all uranium is in an equilibrium reached after ten years of decay.[13]
The photon and neutron production rates of the different uranium isotopes are given in Table 5.3. Table 5.4 provides uranium's photon and neutron emissions of different enrichment levels.

	Neutron production [$kg^{-1}s^{-1}$]	Photon production [$10^6\,kg^{-1}s^{-1}$]
Uranium-233	0.38	495.330
Uranium-234	6.83	383.630
Uranium-235	0.01	75.640
Uranium-236	4.30	0.560
Uranium-238	13.49	0.002

Table 5.3: Uranium Isotopes Photon- and Neutron Production Rates
The values have been determined using the `NNDCDecay` module. The photon production rates include only photons with an energy above 50 keV. The neutron production rate includes only neutrons from spontaneous fission.

Enrichment level	DU (0.2%)	NU (0.711%)	HEU (95.0%)
Neutron production [$kg^{-1}s^{-1}$]	13.46	13.39	0.68
Photon production [$10^6\,kg^{-1}s^{-1}$]	1.44	1.87	83.39

Table 5.4: Uranium's Photon- and Neutron Production Rates
Particle production (neutron/photon) for different uranium enrichment levels after 10 years of decay. The values have been determined using the `NNDCDecay` module. The photon production rates include only photons with an energy above 50 keV. The neutron production rates include only neutrons from spontaneous fission.

5.1.3 Reflector, Tamper and Pusher

The plutonium pit is encased in one or multiple layers known as the *reflector*, *tamper*, and *pusher*, which fulfill three main functions. The reflector enhances reaction efficiency by reflecting neutrons back into the fissile material. This increases criticality and reduces the amount of fissile material needed by about one-third. There are different reflector materials, whereby beryllium is considered superior due to its high neutron scattering and low neutron absorption cross-sections. Additionally, beryllium is very heat-resistant, and beryllium-9 exhibits exceptionally high cross-sections for $(n, 2n)$-reactions, particularly with fast neutrons, which leads to significant neutron multiplication [167]. In 2010, the US declassified the

"*fact that beryllium may be presented within the canned subassembly of an unspecified nuclear weapon*" [168]. However, in the past various materials have been considered or used as reflectors, including the more heat-resistant beryllium-oxide — used in the theoretical superbomb design Klaus Fuchs handed to the USSR [169] — and tungsten-carbide — used in Little Boy and South African gun-type weapons [58].[14] Also, carbon structures like synthetically produced diamonds have been utilized [58].

The tamper resists the thermal expansion of the fissile material to prolong the chain reaction.[15] Therefore, tampers are made of high-density materials. Beyond tungsten-carbide, several U.S., Soviet, and British weapon designs included a tamper made of lead or a lead-bismuth alloy [58].[16] In [170, 171], natural uranium tampers are mentioned that allow a higher yield by enabling additional fission. This has also been seen by the results of the Trinity Test, in which more than 30% of the total yield resulted from fission within the natural uranium tamper [172].

When an explosive shockwave hits the interface between a less dense and more dense material, Rayleigh-Taylor instabilities can develop, resulting in a less-than-optimal compression. To alleviate this effect, an intermediate-density material pusher can be placed between the low-density explosive and the high-density tamper. In Fat Man, an aluminum shell was used for this purpose [153].

Additional layers bring further functionalities: In the potential configuration of Fat Man, a thin layer of borated (boron-10) acrylic surrounded the uranium tamper [99]. This layer is designed to absorb spontaneous fission neutrons that might otherwise be reflected back into the plutonium pit, effectively acting as an anti-reflector for neutrons exiting the reflector.

During "Operation Ranger" in 1951, the US first tested the levitating core design [173]. It was declassified that the only one-year later produced Mk-7, employed such a levitating core design [175]. This design includes an air gap between the tamper and the core, held with wires or foam, which allows the shock wave to gain additional momentum before hitting the core [174].

In 2006, a sketch of an early Soviet design was published that included an additional layer of cork between the explosive and the pusher, which could have a similar purpose [176].

The primary of modern thermonuclear weapons seems to rely solely on a beryllium reflector, omitting tampers or pushers [58, 149, 171]. This change likely stems from the primary's role as an X-ray emitter to ignite the secondary rather than being the sole yield producer. Further, techniques like *boosting* (explained in the following) allow sufficient yield production in the primary without tampers or pushers, facilitating significant weight reduction crucial for missile-deliverable arsenals.

5.1.4 Chemical Explosives

To become supercritical, the plutonium is compressed by conventional chemical explosives. Modern warheads achieve this by using about six times the fissile materials mass in chemical

explosives [177]. The used technique involves explosive lenses that alternate between materials with fast and slow velocities of detonation (VoD), which is the speed at which the shock wave propagates through the explosive material during detonation.
The Fat Man bomb utilized the high-velocity explosive "Composition B" (VoD $= 7,920\,\mathrm{m/s}$), a mixture officially of 60% RDX, 39% TNT, and 1% paraffin wax, and the slow-exploding Baratol (VoD $= 4,870\,\mathrm{m/s}$), a blend of 76% barium nitrate and 24% TNT [58, 166].
Over time, such devices' fast-explosive component was replaced by the faster and more powerful HMX with a velocity of VoD $= 9,110\,\mathrm{m/s}$. However, safer alternatives like TATB (VoD $= 7,720\,\mathrm{m/s}$) have been adopted due to their lower sensitivity to external shocks. However, HMX remains extensively used in Russian systems to this day [58].
Slow explosives have also evolved, with alternatives such as boracitol — a mix of 60% boric acid and 40% TNT — and plumbatol, consisting of 70% lead nitrate and 30% TNT [58].

All explosives primarily consist of carbon, hydrogen, oxygen, and nitrogen, with similar densities, causing minimal variation in neutron and photon emissions across different explosives. In the following models, PBX-9502 (a TATB-based explosive), made up of 95 wt% TNT and 5 wt% KEL F800 binder is assumed [178, 179].

5.1.5 Deuterium-Tritium Boosting

The US declassified the use of the hollow boosting technique in their warheads, which is described as "*a method wherein the boost gas is in a hollow pit at detonation time*" [175].[17] As declassified, this method was first tested during the "Item Test" in "Operation Greenhouse" in 1951 [175].[18] During boosting deuterium (D) and tritium (T) are fused to helium-4 which significantly increases the number of free neutrons in the system [171, 180]. This has three advantages: First, it increases the weapon's yield. Using one mole DT mixture increases the yield of a four-kilogram implosion-type weapon by a factor of 5–10, under the assumption that half of the DT mixture undergoes fusion. [181].[19] For pits with an inner radius of 4.25 cm as described in [25], the pressure of the DT gas would be 154 bar.[20] Secondly, it allows for the usage of a smaller amount of fissile material. Finally, boosting provides a dominant, timed neutron source and by this prevents fizzle yield (premature, low-yield detonations) created by preignition.
For starting the DT fusion reaction, high temperatures (typically 20–30 million Kelvin) and pressures are needed [58]. Once the critical temperature is produced by the energy of the fission reactions, the deuterium and tritium burn by the following fusion reaction in 2–4 ns — much faster than a single fission-chain generation [171]:

$$\mathrm{D} + \mathrm{T} \rightarrow n_{14.1\,\mathrm{MeV}} + \mathrm{He\text{-}4}_{3.5\,\mathrm{MeV}}. \tag{5.1}$$

While the average neutron from uranium fission carries about 2 MeV of energy, DT fusion

neutrons possess an energy of 14.1 MeV. This higher energy makes them much more "effective" due to the increased multiplicity, the higher (n, Xn) cross-sections, and the shorter time they spend in the reflector.[21]
Although boosting is most commonly found in implosion-type weapons, it seems probable that all kinds of weapons have been boosted. The US deployed the W33, an HEU-based gun-type fission weapon with variable yield. During Operation Nougat Aardvark in 1962, it achieved a yield of 40 kt(TNT) [58, 181, 184], suggesting it had boost capabilities. Also, South Africa considered boosting their gun-type weapons [58].
While gas boosting is a common practice in nuclear weapons, obtaining tritium is notably challenging since it must be bred in reactors and replaced regularly due to its short half-life of only 12.3 years. Weapons have also been boosted with other materials: for instance, in the third Chinese nuclear test, the use of a small amount of lithium deuteride increased the yield from approximately 10–30 kt(TNT) to about 100–300 kt(TNT) [171, 185].

5.1.6 Second Stage

A few months after the first successful Soviet nuclear test in 1949, President Harry S. Truman ordered — as a response — the development of a hydrogen bomb. Unlike fission weapons, which are limited in yield by the critical mass of their fissile material components, thermonuclear weapons can theoretically produce arbitrarily high yields. The concept of the hydrogen bomb is closely related to boosting. However, instead of merely providing extra neutrons to enhance fission, it is designed to harness the energy released during fusion. In 1941, Enrico Fermi and Edward Teller were the first to propose the idea of a hydrogen bomb that should use the energy of a fission bomb to ignite a fusion reaction [186]. Several methods have been proposed for igniting the fusion reaction in hydrogen bombs. Initially, the "classical super" concept aimed to ignite a deuterium-filled pipe using heat from a fission bomb, causing the deuterium to burn from one end to the other [56]. However, this approach was abandoned in favor of the Teller-Ulam design, introduced in 1951 [187]. This new design used the X-ray radiation from the fission bomb to compress the secondary to densities sufficient for ignition. In 1952, the US tested Ivy Mike, the first Teller-Ulam design. Due to the scarcity of tritium, Ivy Mike utilized the fusion of two deuterium atoms, requiring a substantial amount of deuterium to be cooled below its boiling point of 23.5 K. This made the bomb very large and impractical for military use, weighing over 74 tons [188]. Additionally, while the ignition temperature for DT fusion with external X-ray heating is only 2.4 keV, for DD fusion, it rises to 10 keV [171]. Despite these challenges, the test was successful, yielding 10.4 Mt(TNT) — about 700 times the yield of Little Boy.
The first test of an aircraft-portable hydrogen bomb was Castle Bravo in 1954. The bomb produced a yield of 15 Mt(TNT) and weighed about 10.5 tons [56, 189]. It was a "dry" fusion design, using solid lithium deuteride (LiD) as fusion fuel. Lithium deuteride has a density of 0.8 $\mathrm{g/cm^3}$ and is ignited in the Jetter cycle in which the lithium-6 is fissioned by a neutron into helium and tritium that then fuses with the deuterium [190]. The lithium for the fusion

fuel requires enrichment of lithium-6. Castle Bravo utilized lithium enriched to 40%, while modern "*weapons require enrichment up to 95% 6Li*", (used for the following models) [188, 191].[22] According to [177], the 95% "*enrichment level is an economic rather than a physical limit*".[23]
The Soviets' first fusion design, RDS-6, successfully tested in 1953, in contrast, employed a "layer cake" design akin to Edward Teller's proposed "alarm clock" from 1946 that was never developed further in the US. This design featured an additional layer of lithium-deuterium around the primary to initiate DT fusion [192]. However, this design is not typically classified as an actual thermonuclear weapon but rather as a boosted weapon due to its inability to produce scalable yields [56, 192]. In 1955, the USSR successfully tested the RDS-37, a Teller-Ulam design. All modern thermonuclear weapons are believed to adhere to this design [58].
A high-Z, opaque tamper encapsulates the secondary's fusion fuel to shield it from premature heating by thermal radiation. It further acts as an X-ray compression ablator. It is commonly constructed from fissile materials, such as uranium, to enhance the weapon's yield through additional fission reactions initiated by the DT neutrons (fission-fusion-fission process) and supply extra neutrons that facilitate the Jetter cycle [171].[24] In the center of the fusion fuel, fissile material (spark plug) is compressed to supercriticality to ignite the fusion reaction. Besides WGPu and HEU, the US also tested uranium-233 spark plugs [177]. While older Teller-Ulam designs feature a cylindrical secondary, newer designs use a spherical configuration, which is more effective for compression.
The radiation channel between the primary and secondary is filled with a low-density, low-Z material, aerogel.[25] Due to the small number of bound electrons per atom, the material can be rapidly ionized, making it transparent to X-rays and prevents the high-Z plasma from the radiation casing from entering the space between the primary and the secondary [171, 194]. The expansion of this aerogel plasma compresses the fusion stage [195]. In the subsequent models, polystyrene foam with a density of $0.016\,{}^{\mathrm{g}}/_{\mathrm{cm}^3}$ is assumed as aerogel [58, 149, 195].
The primary and the secondary are in a *radiation casing*, typically made of aluminum or steel with some lining of depleted uranium (DU) or natural uranium (natU) [58, 195].[26] The radiation casing has the task to reflect the X-rays back onto the secondary.[27]

5.1.7 Reentry Vehicle

Many modern warheads are designed for being missile deliverable. The land-based part of the U.S. nuclear triad consists of 400 LGM-30G Minuteman III Intercontinental Ballistic Missile (ICBM) which can be equipped with up to three W78 or W87 warheads — due to the New START regulations today every ICBM is only equipped with a single warhead [58, 196–198]. The warhead is housed within a reentry vehicle (RV) designed to endure extreme conditions during atmospheric entry. Traveling at velocities of up to $6.8\,{}^{\mathrm{km}}/_{\mathrm{s}}$ (19.8 Mach), the RV must shield the warhead from intense thermal heating and structural vibrations during the 60–90-second reentry phase before reaching its target [199]. While the W78 uses the Mk12-A RV, the W87 uses the Mk21 RV [177]. In the following, these RVs are modeled with

an aluminum substructure, with an outer layer of carbon-phenol (1.555 g/cm^3) and a nose tip of reinforced carbon-carbon (1.89 g/cm^3) [200, 201]. Carbon-carbon is a high-strength composite material with carbon fiber reinforcement in a carbon matrix. It is known for its exceptional heat resistance and durability, particularly in aerospace and high-temperature applications.

5.2 Photon Emissions and Shielding Factors

Significant research focuses on the photon emissions of plutonium, particularly γ-rays, and the information that can be obtained from these emissions. An entire chapter in [202] examines which energy regions yield valuable plutonium data. The Fixed-energy Response-function Analysis with Multiple efficiency (FRAM) code analyzes the isotopic composition of uranium and plutonium using high-resolution gamma spectra and helped establish the foundation for the warhead confirmation system proposed by the UK-Norway Initiative [203, 204]. Luke and Archer introduced in 2000 the "Pu-300, Pu-600, Pu-900" method, which uses gamma emissions from these energy regions to determine when the last americium separation took place, the plutonium-239/plutonium-240 ratio, and the presence of oxygen in the sample — three critical indicators for a sample being a weapon [205].

I present the characteristic photon emissions of WGPu, HEU, and DU in Table 5.5. In a detector, these photon emissions generate additional characteristic peaks — such as the single- and double-escape peaks. In addition to the photons generated by radioactive decay, high-energy photons are produced through neutron capture (n, γ)-reactions and inelastic scattering $(n, n' \gamma)$-reactions. In nuclear weapons, neutrons generated in the plutonium will induce these reactions in the surrounding chemical explosives [80]. An overview of the energies of the most significant of these photons is given in Table 5.6.

The final measured peaks depend not only on the production rate of photon particles but also on their absorption fractions during their travel from their production site through the weapon to the detector. Figure 5.2 shows the energy-dependent transmission fractions of key warhead materials, highlighting that aluminum and the TATB-based explosive PBX-9502 attenuate photons far less than uranium or plutonium. Photons with energies below 100 keV cannot penetrate 1 cm of uranium or plutonium. To ensure strong detector signals from photons, they must have sufficiently high energy and be produced in significant quantities. Examples of promising γ-rays for confirming the presence of WGPu are the higher energy gamma emissions at 662.40 keV, and 722.01 keV.

Energy [keV]	Production [$kg^{-1}s^{-1}$]	Parent	Energy [keV]	Production [$kg^{-1}s^{-1}$]	Parent	Energy [keV]	Production [$kg^{-1}s^{-1}$]	Parent	Material
101.06	2.88×10^7	U-237	102.98	7.36×10^7	U-237	104.23	3.59×10^7	Pu-240	WGPu
110.42	1.73×10^7	Pu-238	111.30	3.29×10^7	Pu-238	114.23	6.83×10^6	U-237	WGPu
114.45	1.29×10^7	Pu-238	115.38	9.86×10^6	Pu-239	116.26	1.22×10^7	Pu-239	WGPu
125.30	1.54×10^7	Am-241	129.27	1.35×10^8	Pu-239	148.57	6.68×10^6	Pu-241	WGPu
203.55	1.22×10^7	Pu-239	208.01	1.90×10^7	U-237	332.85	1.06×10^7	Pu-239	WGPu
345.01	1.19×10^7	Pu-239	375.05	3.33×10^7	Pu-239	380.19	6.54×10^6	Pu-239	WGPu
393.14	7.51×10^6	Pu-239	413.71	3.14×10^7	Pu-239	662.40	1.37×10^6	Am-241	WGPu
722.01	7.40×10^5	Am-241							WGPu
105.60	9.98×10^5	U-234	109.19	1.24×10^6	U-235	120.90	7.90×10^5	U-234	HEU
143.76	8.17×10^6	U-235	163.36	3.78×10^6	U-235	185.72	4.25×10^7	U-235	HEU
202.12	8.05×10^5	U-235	205.32	3.74×10^6	U-235				HEU
112.81	2.65×10^4	Th-234	143.76	1.75×10^4	U-235	163.36	8.13×10^3	U-235	DU
185.72	9.12×10^4	U-235	205.32	8.03×10^3	U-235	258.23	9.64×10^3	Pa-234*	DU
543.98	4.63×10^2	Pa-234*	691.00	1.13×10^3	Pa-234*	699.02	7.19×10^2	Pa-234*	DU
702.00	9.13×10^2	Pa-234*	705.94	7.06×10^2	Pa-234*	740.10	1.38×10^3	Pa-234*	DU
742.81	1.34×10^4	Pa-234*	766.42	4.00×10^4	Pa-234*	781.75	9.80×10^2	Pa-234*	DU
786.28	6.86×10^3	Pa-234*	805.75	7.44×10^2	Pa-234*	825.60	8.33×10^2	Pa-234*	DU
851.58	8.70×10^2	Pa-234*	880.90	5.05×10^2	Pa-234*	883.22	4.42×10^2	Pa-234*	DU
921.72	1.61×10^3	Pa-234*	945.94	1.27×10^3	Pa-234*	996.10	7.06×10^2	Pa-234*	DU
1,001.03	1.06×10^5	Pa-234*	1,124.93	4.25×10^2	Pa-234*	1,193.73	1.71×10^3	Pa-234*	DU
1,237.26	6.62×10^2	Pa-234*	1,392.70	4.36×10^2	Pa-234*	1,434.14	1.23×10^3	Pa-234*	DU
1,510.21	1.65×10^3	Pa-234*	1,553.75	1.04×10^3	Pa-234*	1,737.75	2.69×10^3	Pa-234*	DU
1,765.44	1.10×10^3	Pa-234*	1,809.04	4.72×10^2	Pa-234*	1,831.36	2.20×10^3	Pa-234*	DU
1,867.69	1.17×10^3	Pa-234*	1,874.88	1.03×10^3	Pa-234*	1,911.19	7.87×10^2	Pa-234*	DU

Table 5.5: Nuclear Weapon Related Photon Decay Emission
The production rates were determined for 30-year-old material. The values have been determined using the `NNDCDecay` module. The analysis considers only emissions with an energy above 100 keV, identifying those contributing more than 1% to the total emissions with an energy above 100 keV, and more than 0.1% with an energy above 500 keV. The table includes the direct parent nuclide for each photon (γ-ray). The energies and production rates were rounded to two decimal places.

Element	Energy [keV]
Hydrogen	2,223.25; 6,250.0
Carbon	1,261.77; 3,683.92; 4,945.30
Nitrogen	1,678.24; 1,681.17; 1,884.85; 1,999.69; 2,520.45; 2,830.80; 3,531.98; 3,677.80; 4,508.69; 5,268.98; 5,297.66; 5,533.25; 5,561.95
Oxygen	870.68; 1,087.71; 2,184.38; 3,272.11

Table 5.6: Nuclear Weapon Related Neutron Capture Photon Emission
Notable neutron capture (n, γ) and inelastic scattering $(n, n' \gamma)$ emissions for hydrogen, nitrogen, carbon, and oxygen, major elements in conventional explosives [206]. The energies were rounded to two decimal places.

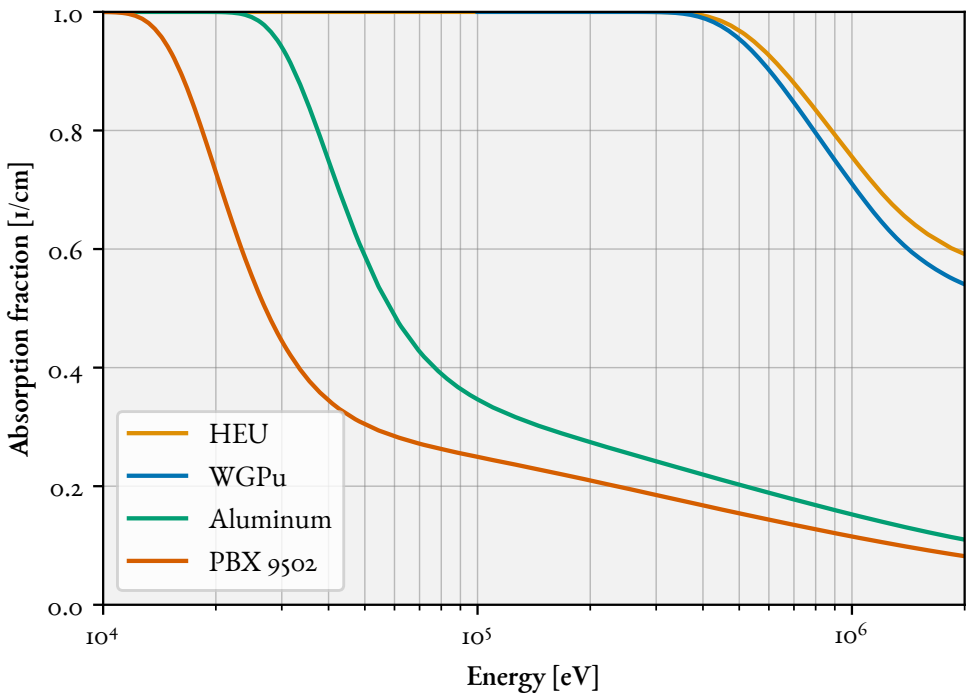

Figure 5.2: Photon Absorption Fractions for Warhead-Related Materials
The photon absorption factors for the warhead-related materials HEU, WGPu, Aluminum, and the chemical explosive PBX 9502 were obtained by OpenMC fixed-source particle transport simulations. The simulations involved directing photons of varying energy perpendicularly through a one-cm-thick vertical slab of each material. The absorption fraction is one minus the fraction of full-energy particles leaving the slab.

5.3 Baseline Signatures of Nuclear Weapons*

Building upon the previous section's description of nuclear weapons' different materials and components, the following section presents theoretical emission models of fissile material, warhead components, and weapons.

5.3.1 Fissile Material Models

Plutonium Point Source

Determining the isotopic vector of plutonium is crucial in various verification procedures, such as neutron multiplicity counting [79]. Therefore, I analyze a one-gram point-source model of plutonium. Using a point source simplifies the model, although a one-gram δ-phase plutonium sphere has a radius of approximately 2.5 mm. In this theoretical model, γ-rays do not interact with the material, resulting in emissions at the discrete energies of plutonium and its decay products.

Plutonium Pit

In the model of [25], the plutonium pit has an inner radius of 4.25 cm and an outer radius of 5.0 cm and consists of 4 kg α-phase plutonium.[28] By assuming gallium-stabilized-δ-phase-plutonium and maintaining the dimensions, the pit's weight is reduced to 3.184 kg. This number still seems reasonable, as according to [177, 208, 209] modern warheads use about 3 kg of plutonium in their primary stage.
In Figure 5.3, the photon emissions of a 0 and a 50 year plutonium pit are compared. The increasing photon emissions from the pit over time result from the decay of plutonium-241 into the more active americium-241. This is most evident in the photon emission spectrum at energies of 56.9 keV, 662.4 keV, and 772.0 keV as can be seen in Figure 5.3.[29]

*Parts of this section are based on the following publication, which primarily builds upon my own work and has been further expanded here:

- **C. Fichtlscherer**, M. Kütt. "Uniqueness, Reproducibility and Discrimination of Nuclear Warhead Gamma Signatures". In: *Science & Global Security* 32.1–3 (2024). DOI: 10.1080/08929882.2024.2387966

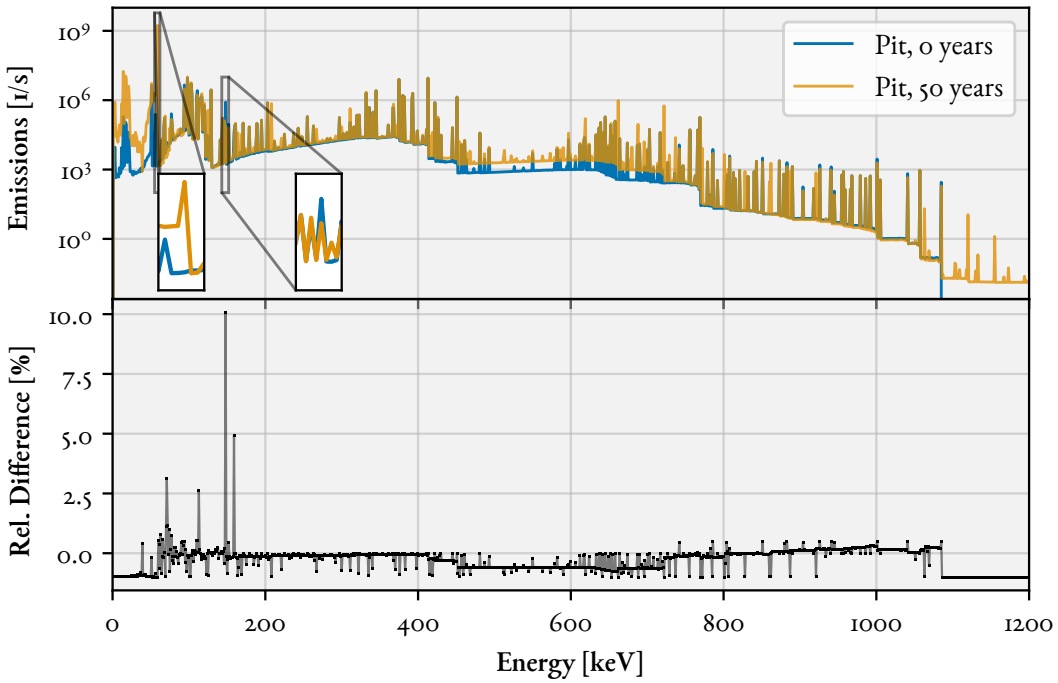

Figure 5.3: Photon Emission Spectra of Plutonium Pits
The simulated photon emission spectra are presented for isolated plutonium pits at two different ages: 0 years and 50 years (top). The relative differences are calculated and depicted in the lower graph, using the formula $^{\text{pit}_{0\,\text{a}}-\text{pit}_{50\,\text{a}}}/_{\text{pit}_{50\,\text{a}}}$. Insets show the effects of the decay of plutonium-241 ($T_{1,2} = 14.3$ years) to americium-241 by focusing on the 59.6 keV γ-ray emission of americium-241, and the 148.6 keV γ-ray emission of plutonium-241.

Beryllium Reflected Plutonium Ball

The Beryllium Reflected Plutonium (BeRP) ball, a sphere comprised of α-phase, weapons-grade plutonium with a mass of 4483.884 grams and a density of 19.604 $^{\text{g}}/_{\text{cm}^3}$, was produced by the Los Alamos National Laboratory (LANL) in October 1980, serving for a sequence of experiments.[30] Encased in a 0.0305 cm thick stainless steel 304 cladding with a nominal density of 7.62 $^{\text{g}}/_{\text{cm}^3}$, the BeRP ball's plutonium metal composition consists of 99.58 wt% plutonium, enriched with minor alloys including 0.0335 wt% gallium, 0.0239 wt% carbon, and 0.001 wt% iron [24].
Various sometimes contradictory compositions of the BeRP ball are reported in the literature and are summarized in Table 5.7. For the analyses presented here, the composition provided by [24] is used and decayed to obtain the current composition of the BeRP ball. The results of this calculation are also presented in Table 5.7.
The photon and neutron emissions of the BeRP ball have been simulated and are shown in

Plutonium-238	Plutonium-239	Plutonium-240	Plutonium-241	Plutonium-242	Americium-241	Date	Source
0.0200	93.740	5.950	0.2690	0.028	0.05570 / 0.0559*	09/1980	[24]
0.0200	93.730	5.960	0.2680	0.028	0.05570	—	[210]
0.0200	93.270	5.910	0.0700	0.030	—	—	[210]
0.0200	93.735 ± 0.005	5.950 ± 0.01	0.2685 ± 0.0005	0.028	—	—	[211]
0.0200	93.740	5.940	0.2690	0.028	0.25000	2009	[18]
—	93.284	5.950	0.2000	0.028	0.11300	—	[212]
0.0160	93.265	5.907	0.0680	0.028	0.24724	2009	[24]
0.0160	93.270	5.907	0.0680	0.028	0.24750	01/2009	simulated
0.0142	93.230	5.898	0.0330	0.028	0.27630	01/2024	simulated

Table 5.7: Comparison of the BeRP Ball's Composition in the Literature
The composition of the BeRP Ball (in weight percent) from different sources. If specified in the source, the date of measurement/analysis is also given. 0.42 weight percent of the plutonium are alloys. Additionally, the composition of the BeRP Ball after simulated decay is presented. * [24] notes ambiguity regarding whether the measured Americium-241 content is part of the plutonium composition or pertains to the overall metal, which is 99.58% plutonium by mass. I adopt the first value.

Figure 5.4.

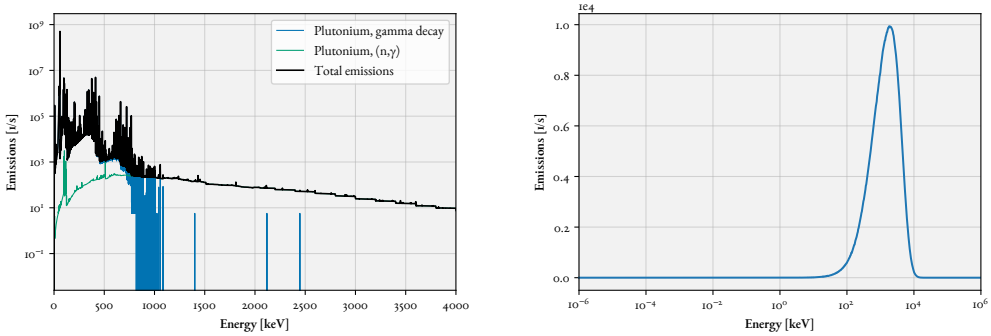

Figure 5.4: Photon and Neutron Emission Spectra of the BeRP Ball
The simulated photon emission spectrum is on the left, and the neutron emission spectrum is on the right. The determined composition at 01/2024 is assumed.

5.3.2 Three Notional Weapon Models

Already ten years ago, in an overview of different confirmation systems, Jie and Glaser stated that "*in order to demonstrate the capabilities of a proposed system, a widely accepted reference item would be extremely helpful*" [213]. In the following, three notional warhead emission models, shown in Figure 5.5, are presented. Each of these could serve as such a reference item.

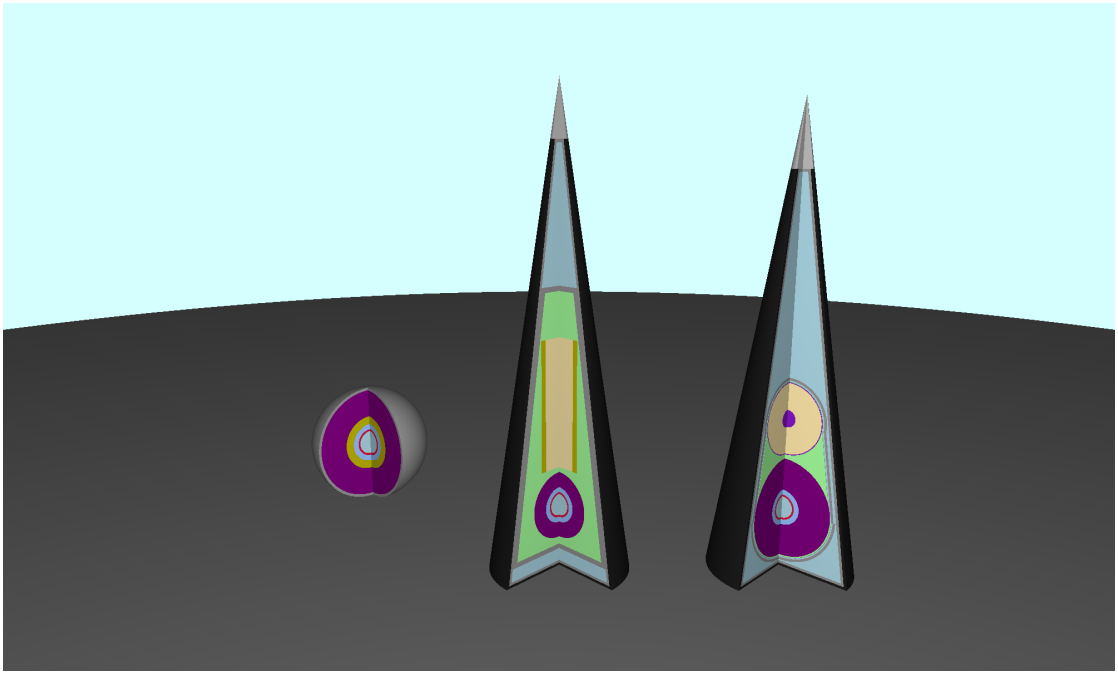

Figure 5.5: Theoretical Warhead Emission Models
A notional single-stage weapon model (left), a notional two-stage warhead model similar to the U.S. W78 (center), and another resembling the U.S. W87 (right). The two-stage warheads are shown within their reentry vehicles, akin to the Mk-12a for the W78 and Mk-21 for the W87.

Frolov-Prilutskii-Sagdeev Model

The first theoretical warhead emission models were published in 1990 following the Black Sea Experiment [25]. The publication contains four slightly different one-stage implosion design weapons, often called the "Fetter Model" after the publication's first author. Based on a private conversation with S. Fetter, I use the new name FPS model, named after the Russian co-authors Frolov, Prilutskii, and Sagdeev, mainly responsible for the model. The models are "*not intended to be realistic weapon designs, but were constructed to define a range of radiation outputs that includes a reasonable lower bound on the radiation that would be emitted by actual warheads*" [25]. Many publications over the last 30 years, like [80, 81, 149], are based on these models.
The models consist of concentric spheres of material. Two models are based on a 12 kg HEU pit with an inner radius of 5.77 cm and an outer radius of 7 cm, resulting in a uranium density of 18.9846 $\mathrm{g/cm^3}$. The other two models are based on a 4 kg WGPu pit with an inner radius of 4.25 cm and an outer radius of 5 cm, which results in a plutonium density of 19.798 $\mathrm{g/cm^3}$ — hinting towards plutonium's α-phase. The pit is surrounded by a 2 cm thick beryllium reflector, a 3 cm thick tamper of either DU or tungsten, a 3 cm layer of chemical explosives and a 1 cm thick aluminum casing.[31]

As HEU-based weapons are hardly detectable by their passive photon emissions and require active measurements, only the WGPu-based models are considered in the following [22].[32] Further, it is only focused on the model with a DU tamper as a fissionable tamper comes with the benefit of a dramatic increase of the weapon's yield (see Section 5.1.3) and is therefore probably the preferable variant.
I assume the pit consists of gallium-stabilized-δ-phase plutonium. Further, PBX-9502 is used as the chemical explosive, even though Soviet weapons during this time were probably based on HMX [58]. The model has a total weight of 126.6 kg, shown in Figure 5.5 on the left. The passive photon and neutron emissions of the model at an age of 30 years are shown in Figure 5.6. Emissions are created by γ-decay in the pit and the tamper, and by (n, γ)- and $(n, n' \gamma)$-reactions mainly in the chemical explosive from spontaneous fission neutrons.

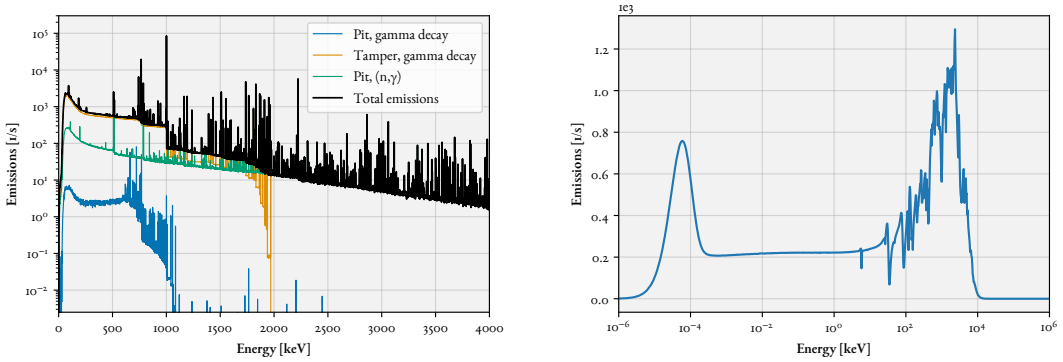

Figure 5.6: Photon and Neutron Emissions of the FPS Model
The simulated photon emissions on the left and neutron emissions on the right of the 30-year-old FPS model. The photon emissions are the sum of different contributions that are broken down in the graph.

Warhead 78 Model

The W78 is a 335 kt(TNT) yield two-stage warhead based on the Teller-Ulam-Design with a cylindrical secondary that was developed during the 1970s by Los Alamos National Laboratory (LANL) [214].[33] Between 1979 and 1982, 1,083 of these warheads were produced, and it is assumed that approximately 920 remain in service [214]. The W78 is currently the oldest weapon in the U.S. nuclear arsenal that has not received significant life extension [215]. Using only publicly available information, I developed a notional emission model resembling the W78. When equipped with the Mk12-A reentry vehicle, it is referred to as the W78-RV.[34]
A sketch of the model can be found in [171]. The same dimensions as in [25] were assumed for the hollow-boosted plutonium pit and the beryllium reflector. The dimensions of the surrounding shell of high explosive were chosen to result in the shell in 15 kg PBX 9502 [171] — close to the 1:6-ratio in mass of fissile material to chemical explosives.[35] The second stage

has a height of 100 cm. The radii of the two cylinders were determined to be 6.909 cm and 9.024 cm, resulting in masses of 6 kg of LiD and 10 kg of DU, respectively, as given in [171].[36] In [171] the radiation cases weight is given with 75 kg. The model here takes the form of a truncated cone. According to [58], it has a thickness between 1–3 cm and has a high-Z material lining. I use natU for that lining as described in [216]. The thickness of the lining was chosen to result in a total weight of 15.5 kg natU, analogous to the W87 model's lining [149]. This results in a 1.868 cm-thick aluminum radiation case with 0.072 cm natural uranium lining. The radiation case and the Mk12-A reentry vehicle are assumed to have a cone angle of 82.2° [216]. The Mk-12a reentry vehicles were modeled with a 0.3 cm thick aluminum substructure, a 1 cm outer layer of carbon-phenol, and a nose tip of reinforced carbon-carbon.[37] The radiation case has a height of 100 cm while the model, including the RV, has a height of 181.102 cm.[38] The calculated total weight of W78-RV is 242.1 kg. In [216], the total weight of the W78 is reported to be less than 362.9 kg. This discrepancy can be attributed to the omission of several detailed components of the reentry vehicle in the model. The photon and neutron emissions of a 30-year-old W78-RV model are shown in Figure 5.7.

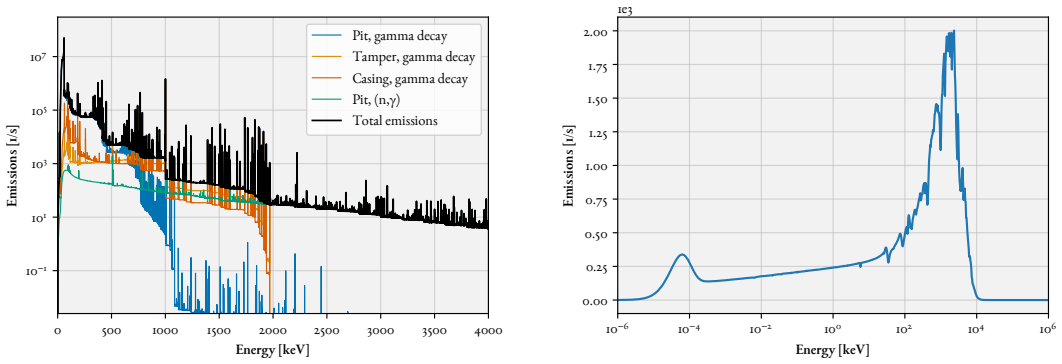

Figure 5.7: Photon and Neutron Emissions of the W78-RV Model
The simulated photon emissions on the left and neutron emissions on the right of the 30-year-old W78-RV model.

Warhead 87 Model

The W87 is an advanced thermonuclear warhead in the U.S. arsenal, utilizing the Teller-Ulam design with a spherical secondary. It has a yield of 300 kt(TNT) that can be increased to 475 kt(TNT) using HEU sleeves around the secondary [216]. Based on the W87, the W87-1 is being developed, intended to replace the W78 in the 2030s [217]. A theoretical emission model of the W87 warhead was proposed by Sonder et al. [149]. Since this model is too large for the associated RV, Mk-21 [216], I reduced the size of the secondary slightly. Further, gallium-stabilized-δ-phase-plutonium instead of α-phase-plutonium was utilized, and the density and composition of the uranium components were corrected according to [159].

Several other features of this model appear uncommon, but I have incorporated them nonetheless: The model includes 56.6 kg of chemical high explosives, which was probably adopted from the FPS model. However, compared to other sources like [171, 218], this amount seems excessive, especially considering that for single-stage weapons, it also needs to compress the heavy tamper material. Based on the assumption that the chemical explosive mass is six times that of the pit material (see Section 5.1.4), an explosive mass of approximately 19.1 kg would be suggested. Additionally, the model uses HEU as the pusher for the secondary, which seems unusual since, unlike the spark plug, the pusher will never reach criticality. Its role is primarily as a high-Z material to compress the LiD before ignition, and it subsequently enables further fission by the 14.1 MeV DT-fusion neutrons. At this energy, the fission cross-section of uranium-238 is significantly higher than at lower energies. Moreover, other sources, such as [177], mention using non-enriched uranium for the pusher.
The RV Mk-21 was modeled similarly to the Mk12-A, based on a 0.3 cm aluminum substructure surrounded by a 1.0 cm carbon-phenol heat shield and a reinforced carbon-carbon nose tip. In [218], a schematic of the W88 warhead is given. Following the naming conventions and the other design schematics, its design is very similar to the W87 model in [149]. One of the main differences is the slight indentation in the radiation case between the primary and secondary components of the weapon, resulting in a peanut shape (compare [177]). To maximize energy transfer from the primary to the secondary, indentations seem counterintuitive, which is why the model does not include this.
The W87 consists of four radioactive components: the 3.184 kg plutonium pit, a 2.95 kg HEU spark plug, a 14.42 kg HEU pusher, and a 15.5 kg NU radiation case. The model's photon and neutron emissions are shown in Figure 5.8.

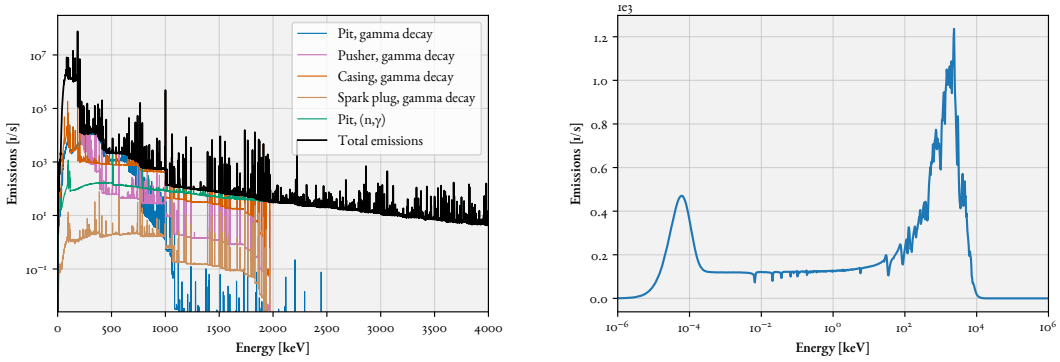

Figure 5.8: Photon and Neutron Emissions of the W87-RV Model
The simulated photon emissions on the left and neutron emissions on the right of the 30-year-old W87-RV model.

Table 5.8 provides an overview of the weight and total emissions of the different emission models. The W78 and W87 warheads have asymmetrical features. In the following I will use the average emissions from these models as an approximation.

	Weight [kg]	Emissions [$^{\text{neutrons}}/_{\text{s}}$]	Emissions [$^{\text{photon}}/_{\text{s}}$]	Pit Fraction
Point source	0.001	63.07	4.50×10^{8}	100.0%
Plutonium pit	3.184	2.63×10^{5}	1.62×10^{11}	100.0%
BeRP ball	4.484	8.54×10^{5}	5.70×10^{8}	99.9%
FPS model	126.554	2.62×10^{5}	9.08×10^{5}	0.3%
W78	202.324	3.08×10^{5}	5.55×10^{8}	97.9%
W78-RV	242.124	2.97×10^{5}	4.53×10^{8}	97.2%
W87	124.574	1.94×10^{5}	3.51×10^{8}	1.1%
W87-RV	164.544	1.82×10^{5}	3.30×10^{8}	1.1%

Table 5.8: Overview of Model's Photon and Neutron Emissions
Emissions of the different source objects (30 years old) except the BeRP ball with an age of 44 years (see Section 5.3.1). The pit fraction describes the percentage of the photon emissions resulting from radioactive γ-decay in the plutonium compared to the overall emissions.

Notes

[1]Plutonium can also be stabilized with alloys like aluminum in its δ-phase, but this produces unwanted (α, n) neutrons, increasing preignition risk and potentially yield reduction.

[2]There are two exceptions to non-artificial plutonium on Earth: traces of plutonium-244 have been discovered on the ocean floor, attributed to extraterrestrial origins, likely deposited by cosmic events such as supernovae or neutron star mergers [219]. Additionally, natural uranium formations can form cracks filled with water, mimicking the conditions of nuclear reactors ("natural reactors"). These formations can produce traces of plutonium via neutron capture from uranium-238 [220].

[3]Other publications present slightly different compositions. For example [25] uses 0.005 wt% plutonium-238, 93.3 wt% plutonium-239, 6 wt% plutonium-240, 0.44 wt% plutonium-241, 0.015 wt% plutonium-242 and 0.2 wt% "other," which is said to be oxygen. The appendix to the same publication [221] does not include the "other" component and adds the weight fraction to plutonium-239 (then 93.5 wt%). In [149] uses 95 wt% plutonium-239, 4.7 wt% plutonium-240, 0.1 wt% plutonium-241, and 0.2 wt% americium- 241 is used. While [152] gives an isotopic vector of 0.02 at% plutonium-238, 93.6 at% plutonium-239, 5.9 at% plutonium-240, 0.44 at% plutonium-241, and 0.04 at% plutonium-242.

[4]While in 2007, a publicly available version of the JASON report concluded that "*there is no evidence from the [underground nuclear-explosion testing] analyses for plutonium aging mechanisms affecting primary performance on timescales of a century or less in ways that would be detrimental to the enduring stockpile*" [222], a reevaluation has occurred since then, as the US has started a new series of subcritical tests in 2024 to "*collect valuable information to support the safety, security, reliability, and effectiveness of America's nuclear warheads*" [223].

[5]These simulations do not include the geometric assembly — the effect of initiated fission chains. As the plutonium produces heat of about 1.9 W/kg via the energy mainly produced by alpha decay [177], it is worth speculating if there is some kind of heat transfer system (e.g., heat pipes) to secure the pit from overheating. In [157], the amount of needed aluminum that could cool the more heat-producing reactor-grade plutonium is estimated. In [224] "In-Flight Insertion Devices" were mentioned in early nuclear weapon designs to insert the pit only minutes before the bomb's dropping for safety considerations. These could also be used to cool a more heat-producing pit.

[6]I developed an OpenMC feature to determine the prompt-criticality specifically. It was officially integrated into OpenMC, starting with version 0.14.0. https://github.com/openmc-dev/openmc/pull/2348

[7]A refinement is the double-gun design, in which two subcritical masses are shot against each other.

[8]South Africa was the only state whose entire arsenal relied on gun-type weapons, which comes with several disadvantages to establishing a position in modern security architectures. Implosion designs are inherently safer, allowing for higher yields and minimization of the warheads. This is especially important for making warheads missile-deliverable.

[9]Early pit designs were solid [151]. Further, in the past, so-called composite pits containing uranium and plutonium were produced [225]. Following [56], it seems that such pits do not bring additional benefits in efficiency or yield. It could be interpreted that composite pits were the result of plutonium scarcity during the early part of nuclear weapon programs. For example, it was declassified that the Soviet RDS-4 (in service from 1953 to 1966) used a composite pit of 4.2 kg plutonium and 6.8 kg HEU (90% enriched) [226]. Lastly, some U.S. artillery warheads, such as the W47, compressed plutonium in a cylindrical instead of spherical form [218]. The W47 was the first nuclear weapon in which the plutonium pit takes the shape of an ovoid [227].

[10]While it is widely assumed that modern weapon pits contain between 3 and 4 kg of plutonium [58, 208], many sources state that weapons can also be produced with significantly less fissile material: The lightest US nuclear weapon — the Mk-54 manufactured between 1961–1965 — had a total weight of 23 kg. It was declassified that the British copy of the Mk-54, called "Wee Gwen" contained 1.6 kg of plutonium and 2.42 kg of uranium — whereby the uranium component was probably the tamper [58, 228, 229]. In [230], it is stated that only 1 kg of WGPu creates a yield of 1 kt(TNT) under high pressures. In [231], the US-trained former head of Germany's only plutonium separation facility, Wolfgang Stoll, claims that 500 g of plutonium is sufficient for a nuclear

weapon under supercompression, which requires pressures exceeding 40 GPa. This is an interesting match of numbers as the US declassified the "*fact that all U.S. weapon pits that contain plutonium have at least 500 grams of plutonium*" [175]. For comparison, the IAEA defines the *significant quantity* (the amount of nuclear material for which the possibility of manufacturing a nuclear explosive device cannot be excluded) of plutonium as 8 kg [158].

[11]However, there are other options. For example, the Iranian nuclear weapons program has worked extensively on uranium deuteride neutron initiators [232]. Experiments conducted in 1989 at the Southwest Institute of Fluid Physics (China's first nuclear fusion research institute) concluded that "*the neutron yields varied on the order of* 10^2 *to* 10^7 *when ... UD*$_3$ *was replaced by D*$_2$ *...*", indicating that deuterium is a much more efficient initiator [233]. This raises questions about Iran's objectives in this context.

[12]Here, I define specific enrichment values for classifications of uranium that are traditionally categorized by ranges of enrichment levels. For instance, unenriched natural uranium may have slight variations in uranium-235 content. The DOE requires for depleted uranium a content of less than 0.3% uranium-235 [234]. Conversely, uranium with more than 20% U-235 content is classified as highly-enriched.

[13]The difference in photon production rates between 10 and 50 year old NU is less than 0.05%.

[14]Tungsten-carbide was also the reflector during the "demon core" accident [235].

[15] In weapons, the heat produced by the fission chain reaction eventually causes the assembly to expand beyond the radius of *second criticality*, thereby self-terminating the reaction [157, 162, 194].

[16]Lead-208 is very stable and resists neutron absorptions by its double-magic neutron and proton number.

[17]In modern weapons, the boost gas is inserted shortly before ignition.

[18]In an interview with Richard Rhodes, Carson Mark, an important figure in the development of the hydrogen bomb, characterized it more as a "proof of principle" than an actual boosted weapon [56].

[19]It may be assumed that this factor could be raised with the use of more DT, as "*according to one well-placed US observer, boosting is 'mainly responsible for the remarkable 100-fold increase in the efficiency of fission weapons' since 1945*" [182, 183].

[20]It is assumed that the plutonium pit is roughly at room temperature.
According to [236] in 2000 "*the exact amount of tritium needed for the stockpile is classified. The planning number of 2.5 kilograms per year is an unclassified approximation of the tritium requirement*". (in [237] 2.8 kg per year is mentioned). In [238] "*the NWC Chairman certified the active and reserve tritium stockpile requirements of 2,800 grams per 18-month irradiation cycle by 2026*". Assuming tritium replacement every 7 years and today's number of 3,748 nuclear weapons in the U.S. arsenal, this results in about 3.5 g (1.17 mole tritium) per weapon [17], where most of the tritium is likely used for boosting, with some possibly needed for the secondary. The US is also working on tritium recycling by separating the strongly neutron-absorbing decay product helium-3 [239].

[21]As the neutron number continues to increase, neutrons that get trapped or "waste" time in the reflector instead of initiating fission reactions become less and less influential.

[22]The Castle Bravo yield was much higher than anticipated because it was not known that lithium-7 also produces tritium through high-energy neutron bombardment, making it the worst radiological disaster in U.S. history [56, 189].

[23]At the beginning of the development of thermonuclear weapons besides deuterium and lithium deuteride, there was a third fusion fuel considered: deuterated ammonia [188], for which there is no evidence that it was ever tested.

[24]Weapons with a fissionable tamper produce especially large amounts of fallout and are therefore considered as "dirty". The US declassified in 2002 "*the existence of uranium enriched to 20 percent or greater in the secondary of a specified weapon*" [193].

[25]One such aerogel might be Fogbank, produced at Y12, which is acknowledged as a component in many thermonuclear devices (among them the W78 and W87). A former general manager at Oak Ridge noted, "*The material is classified. Its composition is classified. Its use in the weapon is classified, and the (production) process itself is classified*" [240]. Fogbank was produced during the 1980s, but its production facility closed in the mid-1990s. In 2000, the US decided to resume production, but initial attempts to reproduce Fogbank were unsuccessful,

and it wasn't until 2008 that they succeeded. In the meantime, the US had lost the ability to produce one of the critical components of its nuclear weapons [241].

[26]Also other heavy metals are used, as the US declassified in 2008 the "*fact that thorium metal is used in the radiation case of the W71 warhead*" [242].

[27]Even though a significant part of the weapon's yield is generated from the final fission reactions within the radiation casing. There are also non-fissionable radiation casings [58].

[28]There are multiple sources on other pit sizes: the NNSA states that pits have "*about the size of a bowling ball*" [243], whereby a typical bowling ball has a radius of 10.85 cm, which would result in a remarkably larger and thinner pit [244]. This size also fits the object (probably a pit from the Pantex Plant in 1996) seen in [245] and the leaked pictures from the Israeli weapons' pits from 1985 [246].

From the measurement of the Black Sea Experiment, the authors concluded a plutonium mass of 3–6 kg with an outer radius of 5.4–8.0 cm for the Soviet SS-N-12 [39]. The US declassified that "*hypothetically, a mass of 4 kilograms of plutonium or uranium-233 is sufficient for one nuclear explosive device*" [175].

[29]For the emission plots in this work, only emissions above 0.0025 counts per second are displayed, indicating that this signal would be measurable within a three-sigma interval over an hour of measurement time. A detection rate of 0.0025 counts per second results in an average of 9 counts per hour. The three-sigma interval for this one-hour measurement would be 9 ± 9 counts. Any count exceeding this rate would be detectable, even within a three-sigma confidence interval.

[30]One of the initial experiments employing this sphere involved a critical benchmark test using a beryllium metal reflector, which led to the sphere being named the Beryllium-Reflected Plutonium (BeRP) ball [24].

[31]From the measurement of the Black Sea Experiment the authors concluded a 3–10 cm thick sphere of high-explosives for the Soviet SS-N-12 [39].

[32]The high-intensity γ-ray emissions of uranium-235 are in the energy range of 130–230 keV, which can be shielded easily.

[33]In another chapter of [214] the yield of 330 kt(TNT) is given. In [58], the yield is stated to be between 335–350 kt(TNT). In [197] the yield of 340 kt(TNT) is given.

[34]The U.S. nuclear deterrent comprises only seven warhead models: B61, B83, W76, W78, W80, W87, and W88. Historically, the US developed a much larger number of different warhead types with (status 2020) the FM, LB, B3, B4, T4, B5, W5, B6, B7, W7, B8, W9, B11, B12, B14, B15, B17, W19, B21, W23, B24, W25, W27, B27, B28, 'B28-2,3', W28, W30, W31, W33, W34, W38, B39, W39, W40, B41, B43, W44, W45, W47, W48, W49, W50, W52, W53, B53, W53, B54, W54, W55, W56, B57, W58, W59, B61-1, B61-2, B61-5, B61-10, W62, B63, W66, W68, W69, 'W70-1,2', W70-3, W71, W72, 'W79-0,1', W80-0, B83-0, W84, W85 "*not longer in stockpile*" anymore, the B61-3, B61-4, B61-7, B61-11, W76-0, W78, W80-1, B83-1, W87-0, W88 "*being phased out*", and the for the B61-12, W76-1, W76-2, W80-4 (not enter the stockpile yet), W87-1 (not enter the stockpile yet), W88 Alt 370, W93 (not enter the stockpile yet) for "*future deterrent*" [247, 248]. Here "W" stands for warhead (delivered by missiles), "B" for bomb (dropped from an airplane), "T" probably for tactical, "FM" is Fat Man, "LB" is Little Boy. In addition, the US had the T1 as part of its arsenal, which does not appear in the source above as it is the only U.S. nuclear weapon that was not developed in a nuclear weapons laboratory but directly by the U.S. Army [58]. The gaps in the numerical sequences probably represent weapon models that never entered the stockpile since they were either canceled in the development phase (like the W21 [218]) or pure test devices like the Trinity Gadget or Ivy Mike.

[35]Originally, the W78 employed chemical explosives in its primary that were sensitive to external shocks, indicating the use of materials other than TATB [177]. Plans to replace the explosive in the W78 have faced challenges, as "*we can't simply swap out IHE [insensitive high explosives] for the conventional HE [high explosives] being used in the W78. The primary design must be modified*" [249]. Despite these difficulties, it was decided to use the shock-insensitive high explosive PBX-9502 for the model.

[36]In [171], the primary is placed on top of the secondary. To make it fit into the MK12-A RV, the secondary was placed at the top as high as possible in the radiation case. Further, interestingly, the model does not have a spark plug, which is also mentioned in [177]. According to [218], the secondary of the W78 is identical to that

of the older W50. The W50 warhead, weighing only 187 kg, was exceptionally light, likely due to its original development for the Nike Zeus anti-ballistic missile program. This may have led to the decision to reduce weight by omitting the spark plug. To initiate the Jetter-Cycle without a spark plug, DD or DT fusion may generate high-energy neutrons in the secondary.

[37] The simplified model of the reentry vehicle is based on [200, 201]. In [201], it is assumed that "the heat shield required for a 7,400 kilometer MET [Minimal Energy Trajectory] is roughly 5–10 millimeters".

[38] The height of the RV in [171] is given with 180 cm, while in [214], the height is given with 181.3 cm.

This page intentionally blank

Chapter 6

Vulnerabilities of Weapon Signatures

In this chapter, I describe how nuclear signatures of the introduced emission models in Section 5.3.2 emerge from measurements with confirmation systems (Section 3.2). Next, I evaluate the completeness of these signatures — their ability to correctly accept authentic warheads — by assessing the systems' capability to verify warheads of varying ages using a template-based approach. Finally, adopting a red-teaming approach, I examine the soundness of the signatures — their robustness against hoax objects — by analyzing the uniqueness of the signatures when confronted with four distinct types of hoax objects.

6.1 Nuclear Signatures of Warheads*

For measuring the weapon's photon emissions, the analyzed confirmation systems rely on a cylindrical sodium-iodide (NaI) scintillator detector (see Section 3.2). To determine the emission model's signature (output in the confirmation system) more efficiently, I simulated the response function of this detector. Using publicly available high-resolution data from the IBX II system [250], I derived the detector's resolution (Equation 4.3):

$$a = 29.243\,\mathrm{keV}, \qquad b = 0.011\,\mathrm{keV}^{1/2}, \qquad c = 6.680\,\mathrm{keV}^{-1}$$

I then computed pulse-height tallies in the NaI-crystal in 12,000 individual simulations, ranging from 0 to 12 MeV in steps of 1 keV (see Section 4.2). The detector response function, shown in Figure 6.1, was determined by applying Gaussian broadening with the determined detector resolution to the pulse-height tally values. Figure 6.1 shows the main features of a gamma spectrum: The full-energy peak is shown, which occurs when the entire energy of the particle

*Parts of this section are based on the following publication, which primarily builds upon my own work and has been further expanded here:

- **C. Fichtlscherer**, M. Kütt. "Uniqueness, Reproducibility and Discrimination of Nuclear Warhead Gamma Signatures". In: *Science & Global Security* 32.1–3 (2024). DOI: 10.1080/08929882.2024.2387966

is absorbed. The Compton edge marks the maximum energy transferred to electrons via Compton scattering. Further, the single and double escape peaks, which are 511 keV and 1,022 keV away from the full-energy peak, respectively, are shown. They result from the escape of one or both annhilation photons after pair production. A similar effect is seen at 511 keV: the particle-inducing pair production, and one of the annihilation photons is detected. Finally, the backscatter peak appears at about 200 keV.

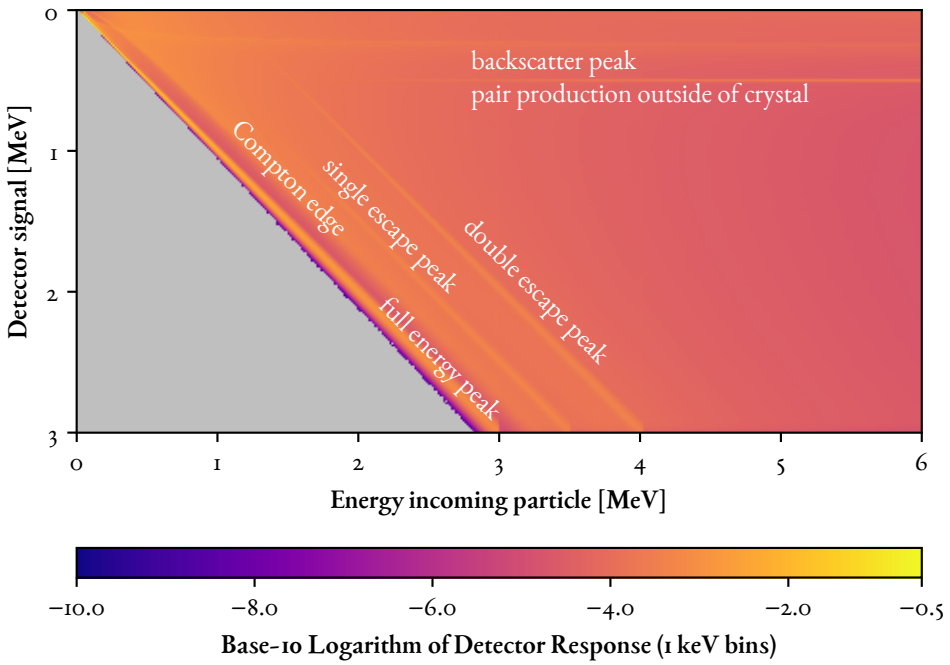

Figure 6.1: Detector Response Function 2x2 Inch NaI Scintillation Detector
The simulated detector response function is plotted on a logarithmic scale (base 10). The events with zero entries are represented in gray. The plot shows the different characteristic peaks of the gamma spectrum.

To determine the warhead gamma signatures, I assume this detector response is for the analyzed confirmation systems, whereby they still have different bin structures. A linear interpolation approach was employed to estimate the detector's response to incoming energies falling between the discrete steps of the detector response function.
For the MCTM system, which allows an additional indirect measurement of the object's neutron emissions, I assumed that photons would enter the detector only through the 2.25 cm hole in the steel block in front of it, effectively reducing its active area. The neutron-induced reactions in the polyethylene mask and the corresponding detector response of the MCTM

system were simulated separately for each emission model and hoax object.

6.2 Completeness of the Nuclear Signatures*

Warheads of the same type must exhibit consistent signatures to ensure completeness in the confirmation process, with any variations remaining within an acceptable range. As modern warheads are manufactured with the highest precision, a major factor contributing to discrepancies in these signatures is the warhead's age.[1] As plutonium undergoes radioactive decay, its photon emissions change significantly, primarily due to the accumulation of americium-241. In contrast, the plutonium's neutron emissions, as well ass emissions from uranium components, remain largely stable over considered time frames. Consequently, warhead signatures dominated by photon emissions from the plutonium pit are particularly sensitive to aging effects (see Table 5.8). Figure 6.2 presents test results of different confirmation systems for the plutonium pit and the W78-RV, whose photon emissions are primarily driven by γ-decay in the plutonium. It should be noted that some of the operational W78 warheads were produced as early as 1979 [215].
The results indicate high false negative rates for warheads of varying ages. Whereby the defining factor is not the age of the warhead but the time when the plutonium was bred in the reactor or last refined or purified before pit production. The majority of the current U.S. pits were produced during the 1980s. Since the closure of the Rocky Flats Plant in 1989, the United States has produced only a limited number of pits — on the order of tens — at Los Alamos. However, the NNSA has recently announced plans to significantly increase pit production in the coming years [258]. An additional challenge arises if there is a significant time gap between the measurement of the golden sample and the measurement of the warhead.
My analysis indicates that the observed signatures do not always ensure completeness in the confirmation process, especially when gamma emissions from the plutonium dominate the emission model's spectrum. In many cases, the system incorrectly determines that the object does not match the template, falsely concluding that it is not a warhead, even when it is. This implies that, future verification procedures would require multiple golden samples of different ages rather than a single one, thereby increasing the complexity of the process.

*Parts of this section are based on the following publication, which primarily builds upon my own work and has been further expanded here:

- **C. Fichtlscherer**, M. Kütt. "Uniqueness, Reproducibility and Discrimination of Nuclear Warhead Gamma Signatures". In: *Science & Global Security* 32.1–3 (2024). DOI: 10.1080/08929882.2024.2387966

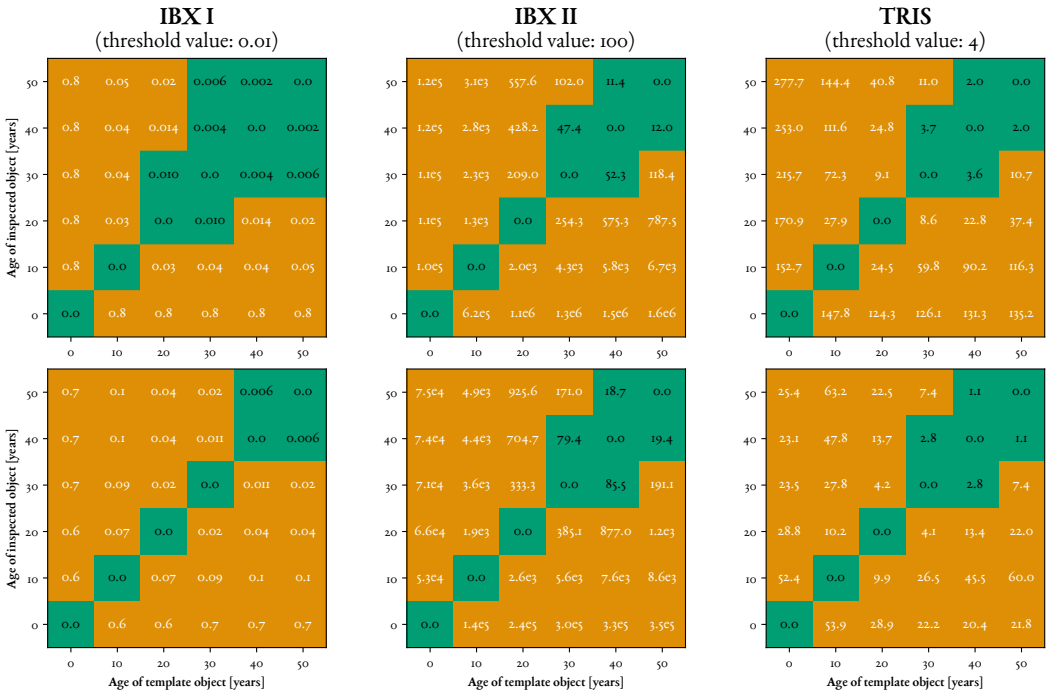

Figure 6.2: Confirming the Pit and the W78-RV Model in IBX, IBX II, and TRIS
This figure shows the theoretical best-case test results for the confirmation systems IBX, IBX II, and TRIS when confirming the pit (top) and the W78-RV model (bottom) to themselves, ranging from 0 to 50 years. On the x-axis, the age of the object is shown, and on the y-axis, the age of the inspected object is shown. The test results are given in the heatmap, where green represents a positive test result (objects are considered the same) and red represents a negative one (false negative result).

6.3 Soundness of the Nuclear Signatures*

A hoax is an object designed to be misidentified as an actual warhead by a confirmation system. Its design, therefore, depends on the specific confirmation system and warhead it seeks to mimic. Unlike an open-ended investigation, a verification process relies on pre-agreed, exact measurements. Inspectors who suspect deception cannot conduct additional measurements without the host state's consent. This requirement enables a state to meticulously prepare for verification — calibrating hoax objects to particular measurement systems and even rehearsing

*Parts of this section are based on the following publication, which primarily builds upon my own work and has been further expanded here:

- **C. Fichtlscherer**, M. Kütt. "Uniqueness, Reproducibility and Discrimination of Nuclear Warhead Gamma Signatures". In: *Science & Global Security* 32.1–3 (2024). DOI: 10.1080/08929882.2024.2387966

the disarmament procedure with these devices in controlled exercises.

By employing hoaxes, a state could seek a strategic or militarily significant advantage [29]. For instance, a state might consider it beneficial to retain parts of its arsenal that are slated for disarmament while dismantling hoax objects instead.[2] The U.S. B61, for example, consists of 4,000–6,000 different parts [58, 218]. However, when attempting to deceive a disarmament process, only a few of these components are critical for a state to retain. These critical components probably include DT boosting gas, enriched lithium, and, most importantly, WGPu, as their clandestine production poses significant challenges.

Various concepts of hoaxes have been proposed in the open literature. One idea is to replace the warhead with a hoax object from "*materials that emit neutrons and γ-rays with an appropriate spectrum*" [27]. A related concept was explored in a 2004 study by Lawrence Livermore National Laboratory, which assessed the quantities of barium-133 required to replicate the γ-ray intensity of 1 kg HEU and 10 g plutonium-239 [251]. Based on this, in Section 6.3.1 I analyze a hoax concept in which the entire warhead is replaced with an optimized combination of photon-emitting nuclides to mimic the gamma emission signature of an actual warhead.

A 1998 report by the U.K.'s Atomic Weapons Establishment proposed the replacement of fissile material in a warhead with "*imitating materials*" to create a hoax object [26]. This is done in Section 6.3.2 that expands upon the first hoax design, by only removing the plutonium pit and leaving the rest of the weapon intact. A combination of photon-emitting nuclides coating the weapon's exterior, combined with a polonium-210–beryllium-9 (α, n)-neutron source in the weapon's interior — used to mimic the characteristic photon emissions originate from (n, γ)- and (n, n', γ)-reactions in non-fissile components — is optimized to replicate the warhead's radiation signature.

Many sources suggest the replacement of the WGPu pit with the more available RGPu [22, 50]. Section 6.3.3 analyzes a hoax concept by replacing the WGPu pit with a thin shell of reactor-grade plutonium (RGPu). This substitution allows for an even closer match of the (n, γ)- and (n, n', γ) emissions, as the energy distribution of these neutrons matches the energy spectrum of the WGPu pit much closer.

Section 6.3.4 presents a further elaboration of the hoax object, by removing only parts of the weapon's fissile material. The concept of partial removal of fissile material has been widely examined in the literature. For example, declassified hoaxes from Field Test 34 contained only 500 g of WGPu [51] (compare Figure 2.2). Similarly, [18] analyzed how the MCTM system could confirm the BeRP ball after removing different portions of its core material. A 2004 study assessed the amount of californium-252 needed to replicate the neutron intensity of 200 g of plutonium [251]. Also [43] proposed a hoax object that utilized a californium-252 source to replace the WGPu pit in a weapon (placed in a container) that "*will produce almost identical neutron flux densities and energy distributions at the container surface*". For the hoax object instead of removing the entire plutonium pit, only portions of it are replaced with a californium-252 neutron source. This approach enables a more precise replication of the

neutron count-rate and energy distribution.

6.3.1 Replacing the Warhead with Radioactive Nuclides

For this hoax concept, it is assumed that the entire warhead is replaced with an optimized combination of photon-emitting nuclides.

Potential Isotopes

I assume that nuclides considered for a hoax must have a half-life of at least seven days. In the ENSDF dataset (see Section 4.1), 271 such unstable nuclide states exist. Out of the 271, 73 are directly accessible via the DOE's Isotope Program, which holds exclusive authority within the DOE for isotope production and distribution. With over 310 nuclides (from which many are stable), it is one of the world's leading isotope producers. It is presumed that a potential attacker would have access to these nuclides at least.
Besides using individual nuclides, they could also be utilized in equilibrium with their decay products (see Section 3.1). The 271 nuclide states lead further to 199 equilibria that allow the utilization of shorter-living nuclides (with their parents) for a hoax. An approximate equilibrium is reached by allowing decay to proceed for a period equivalent to seven times the half-life of the longest-lived parent nuclide.
Figure 6.3 illustrates the relationship between half-life and average photon emissions for all nuclide states. Photons with an energy below 50 keV are efficiently shielded. Hence, they are unsuitable for verification measurements and are excluded. In the log-log plot, a clear linear correlation is evident among the photon-emitting nuclides, as the black dashed line shows. This linear fit corresponds to the following relationship:

$$\text{Average emitted photons [1/s/mol]} = 1.96 \cdot 10^{18}[1/\text{mol}] \cdot (\text{Half-life [days]})^{-1.06}\,.$$

This equation illustrates how the average photon emission rate decreases with increasing half-life, following a power-law relationship.
Additionally, the plot illustrates that americium-241 emits more photons than its parent nuclide, plutonium-241, which leads to the seemingly paradoxical effect where plutonium's photon radiation increases as it ages.

Optimization Process

Determining the optimal combination of nuclides that mimic a specific gamma signature, is a minimization problem. For the TRIS and IBX II systems, this problem is convex, while for the IBX and MCTM systems, it becomes non-convex:

$$\arg\min_{h\in\mathbb{R}_+^{|I|}} \left(\mathcal{T}(Rh, w_T) + \mathcal{T}(R\mathcal{B}_t(h), w_{T+t}) + \lambda||h||_1 \right). \tag{6.1}$$

Here, I denotes the set of considered nuclides and equilibria, and h represents their amounts. All entries of h must be non-negative. Further, certain entries can be forced to zero to avoid specific nuclides (e.g., expensive or chemically unstable ones). The matrix R contains their detector response functions, and w_T is the template signal at the sample's age T. The function $\mathcal{B}_t(h)$ computes the nuclide vector h after a decay time t, solving the corresponding Bateman equations. The function $\mathcal{T}$ is the test function specific to the IBX, IBX II, TRIS, or MCTM system.

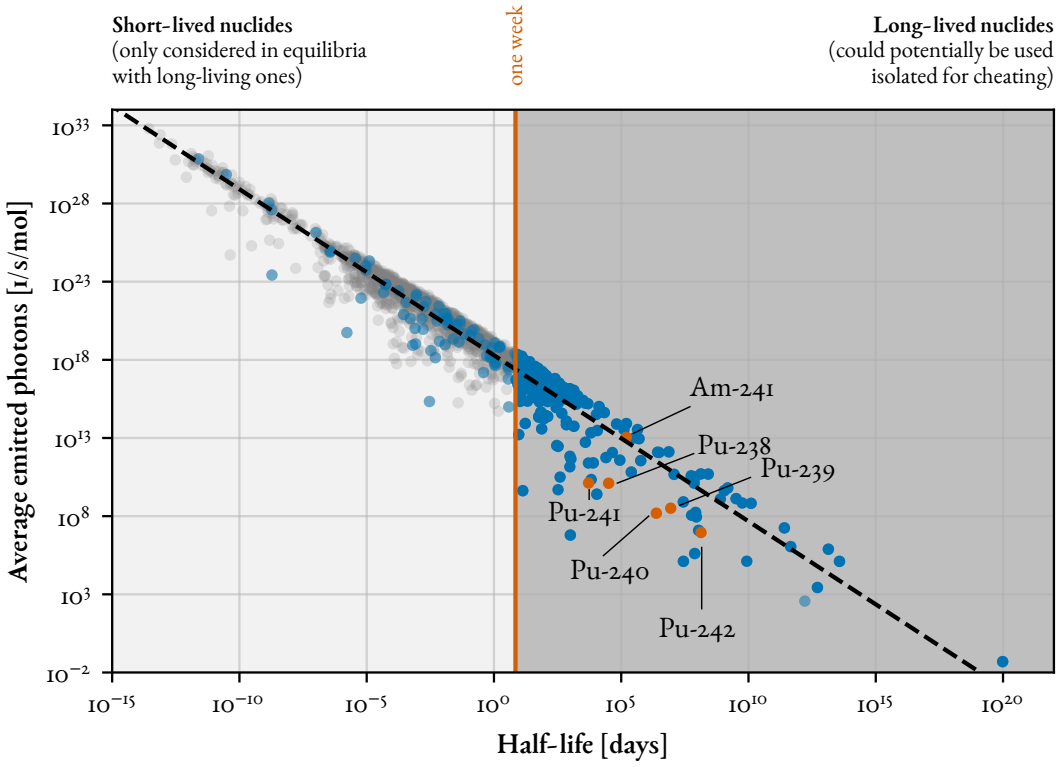

Figure 6.3: Photon Emission Rates and Half-Life of all Photon-Emitting Nuclide States The nuclide information is determined from the NNDC-provided ENSDF data. The dashed black line shows a fit of the linear relationship between the half-life and the average photon emission rate (linear in the log-log plot). Grey dots represent nuclides with photon emissions but are not considered in the following. Blue dots represent nuclides considered for the presented simulations by the constraint of their short half-life. The key fissile material nuclides are marked in red. Only photon emissions with an energy above 50 keV are considered.

The objective function comprises three terms:

- **Template fit:** The first term, $\mathcal{T}(Rh, w_T)$, optimizes the fit to the template signal.
- **Temporal consistency:** The second term, $\mathcal{T}(R, \mathcal{B}t(h), wT + t)$, ensures that the hoax remains effective after a specific time. The signature change due to decay is continuous. It is assumed that if the hoax signal matches the template at the beginning and after three days, match the template throughout this entire interval.[3] The decay of the warhead and plutonium is significantly slower and thus can be neglected.
- **Regularization:** The third term, $\lambda|h|_1$, is a regularization term that promotes sparse solutions, favoring the use of as few different nuclides as possible. Using the 1-norm of h maintains the convexity of the regularization term while encouraging sparsity [252]. The regularization parameter λ controls how strongly this condition should be weighted compared to template matching and temporal consistency.

Hoax objects are assumed to be point sources. In practical applications, the material could be applied as a thin layer to a plastic sphere, creating a surface source with emissions equivalent to a point source. The nuclides could be distributed heterogeneously, thus avoiding undesirable chemical reactions. Precise compositions could be determined by measuring activity rather than mass. Due to the small quantities of material involved, self-shielding effects can be neglected for most detected hoaxes. Within the theoretical model, some bins of the template may be zero, rendering the χ^2-test less suitable. An indicator function excludes nuclides that contribute to these empty, uncompared bins during optimization. In real-world applications, this concern can be neglected due to background radiation. Consequently, the comparison of these bins was omitted in the optimization problem. The optimal hoax compositions are ultimately determined by solving the convex optimization problem presented in Equation 6.1, using the Sequential Least Squares Programming (SLSQP) method provided by Python's SciPy package [253]. The initial guess for the optimization is derived from the combination of nuclides whose spectrum is closest to the template in terms of the Euclidean norm, obtained using SciPy's Non-Negative Least Squares (NNLS) solver [254]. To determine the precise amounts of the respective nuclides, their combined activities were adjusted to match the activity of the template.
The minimization problem presented in Equation 6.1 was solved using two approaches. First, I sought a combination of nuclides whose combined spectrum closely matches the template's. Second, I emphasized the regularization term to find a *minimal hoax* that is just within the error tolerance of the respective test but consists of as few different nuclides as possible. To further reduce the number of other nuclides in the solutions, a meta, depth-first greedy algorithm was employed [255]. This algorithm starts with a solution of Equation 6.1 with a specific regularization parameter λ and tries to reduce the number of different nuclides in the solution even further by excluding one of the nuclides of the solution from I and then solving the minimization problem again. When a new solution is found from that solution, one of the

nuclides of the solution is additionally excluded from I. This process is repeated until the minimization problem leads only to solutions outside the error tolerance of the respective test. Solutions using an even smaller number of nuclides run thousands of these minimization processes with restricted I. Additionally, in both types of hoaxes, I excluded solutions that required quantities of nuclides exceeding 50 kg, as such large amounts would present significant practical challenges and serve as an additional obstacle.

Results

An example of such a hoax is shown in Figure 6.4 that provides detailed spectra for a cheating scenario within the TRIS framework. The figure includes the spectrum of a minimal hoax, the template spectrum, a 30-year-old W87-RV warhead, and the individual detector signals corresponding to each nuclide involved.

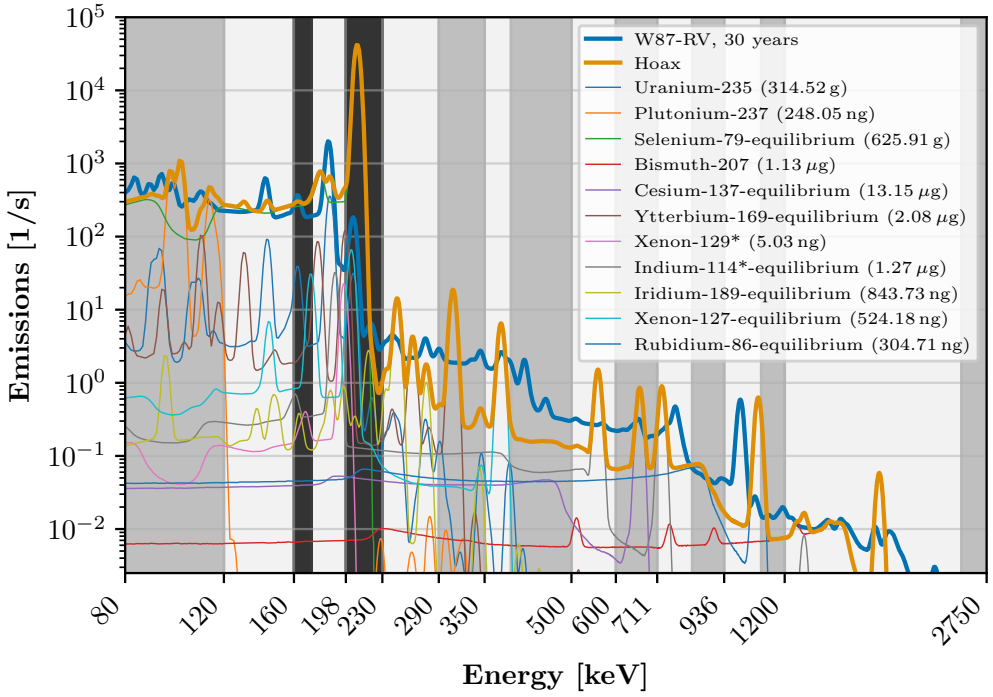

Figure 6.4: Nuclide Hoax of a 30-year-old W87-RV Warhead
A log-log plot illustrating the detector signal within the TRIS framework. The figure contrasts the individual isotopic emissions of the minimal hoax ($\chi^2_r = 2.32$) with their combined cumulative spectrum. The two bins excluded by TRIS are prominently highlighted in black. An asterisk (*) next to a nuclide's name signifies its metastable state, while the label "equilibrium" indicates that the nuclide is in equilibrium with its decay products.

To assess the influence of each nuclide on the hoax's effectiveness, I calculated the TRIS test results for all eleven hoax configurations, systematically omitting one nuclide at a time. The results are provided in Table 6.1

Removed nuclide	Amount	χ^2_r
Uranium-235	314.52 g	63.49
Plutonium-237	248.05 ng	29.34
Selenium-79-equilibrium	625.91 g	40.94
Bismuth-207	1.13 µg	31.13
Cesium-137-equilibrium	13.15 µg	23.73
Ytterbium-169-equilibrium	2.08 µg	18.60
Xenon-129*	5.03 ng	14.97
Indium-114*-equilibrium	1.27 µg	11.42
Iridium-189-equilibrium	843.73 ng	9.11
Xenon-127-equilibrium	524.18 ng	7.47
Rubidium-86-equilibrium	304.71 ng	5.91

Table 6.1: Chi-Square Values for Removing Specific Nuclides
The test results of the hoax presented in Figure 6.4 has $\chi^2_r = 2.32$. The table shows the test results when removing individual nuclides from the hoax.

Figure 6.5 provides an illustrative example of the hoax objects designed for the FPS model, W78-RV, and W87-RV, specifically for the IBX II and TRIS confirmation systems.
Table 6.4 presents a comprehensive overview of the vulnerabilities of all four confirmation systems. It can be seen that hoaxes in which the entire weapon model is replaced with a combination of other radioactive nuclides can not replicate high-resolution, but low-resolution gamma spectra. In the context of the MCTM system, only seven isotopes produce γ-rays within the energy range of 2,175–2,275 keV that could potentially mimic the neutron-induced peak at 2,223 keV and possess half-lives exceeding 7 days: europium-156, tin-125, antimony-124, vanadium-48, cobalt-56, arsenic-74, and rhodium-102. However, for each of these isotopes, the intensity of gamma emissions at this high-energy range is sufficiently low, rendering them unsuitable due to their associated emission of additional undesired photons.
In general, this type of hoax is more effective for objects with photon emissions that predominantly result from decay within the plutonium pit. As there are only a few nuclides emitting γ-rays in the higher energy range of the typical (n, γ) and $(n, n' \gamma)$ emissions.

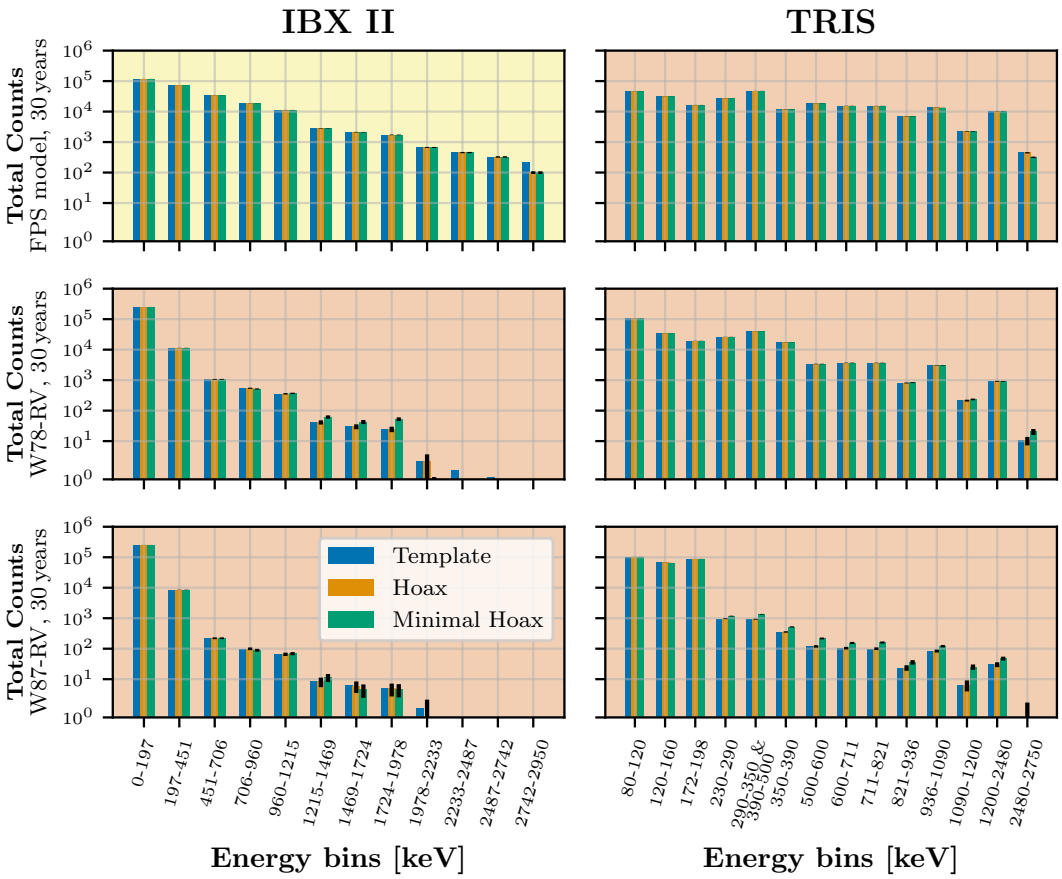

Figure 6.5: Simulated Template Measurements for Nuclide Hoaxes
The "Hoax" denotes a combination of nuclides as close as possible to the template signal. At the same time, the "Minimal Hoax" is the solution with the smallest number of nuclides, which is still accepted by the confirmation system. The error for the individual bins is given as the square root of the respective counts. An orange background denotes that cheating could be facilitated using some of the 73 nuclides the DOE Isotope Program offers. A yellow background suggests that the potential for cheating exists only with nuclides not supplied by the DOE Isotope Program.

6.3.2 Replacing Plutonium with an (α, n)-(n, γ)-Source

In the second hoax scenario, it is assumed a malicious actor would replace the plutonium pit from a nuclear weapon with another neutron source, which will produce similar (n, γ) and $(n, n' \gamma)$ emissions. In cases where the entire emission model is composed of plutonium (e.g., the plutonium point source, the pit, and the BeRP ball), I assume a complete replacement of the object, following the approach used in the first hoax scenario. In addition, the actor

could strategically position radioactive nuclides around the exterior of the hoax object to more convincingly replicate the gamma signature of the original device.
As a neutron source that would be placed inside the pit-less weapon model, I consider a mixture of polonium-210 and beryllium-9 ("PoBe source") that produces neutrons through the (α, n)-reaction

$$\alpha + {}^{9}\mathrm{Be} \rightarrow {}^{12}\mathrm{C} + n + \gamma_{4.44\,\mathrm{MeV}}. \tag{6.2}$$

As shown in Equation 6.2, the PoBe source produces not only neutrons but also 4.44 MeV γ-rays. These γ-rays were also simulated, as they can influence the signature of the hoax by directly generating signals in the detector or inducing secondary effects. This effect is particularly significant in emission models where the PoBe source, located in the place of the former pit, is not heavily shielded (see Table 5.8).
The energy spectrum and yield of the produced neutrons were determined using the software Sources4C [256].[4] The neutron energy spectrum of the PoBe source and the neutron energy spectrum of WGPu are shown in Figure 6.6. The energy spectrum of spontaneous fission is described by Watt distributions, which are very similar for various fissile materials (see Table 3.1) [78]. Since the cross-sections of the (n, γ) and $(n, n'\,\gamma)$ reactions depend on neutron energy, the intensities of the resulting γ-rays vary accordingly. Simulations show that neutrons with the energy distribution of a plutonium source are 2.49 times more likely to induce (n, γ) reactions in hydrogen compared to neutrons from a PoBe source. Conversely, neutrons from a PoBe source have a 1.53 times higher probability of inducing (n, γ) reactions in carbon than those from a plutonium source. However, as the (n, γ)-cross-sections for hydrogen are approximately four orders of magnitude larger than the carbon (n, γ)-cross-sections, this effect minimally impacts detection in confirmation systems.[5]
In the following, I assumed that the intensity of the PoBe source would remain constant for over three days. Further, I neglected the 803 keV γ-ray that can be produced with a minimal probability of 0.001% when polonium-210 decays into an excited state of lead-206. In the optimization procedure, the emissions of the PoBe source inside the pit-less object were simulated and incorporated into the optimization algorithm from the previous section, treating it as an additional isotope available for adjustment. Additionally, the process now accounts for baseline emissions from uranium components (because not the entire warhead is replaced), resulting in the absence of a viable hoax for the W87 in the TRIS confirmation system. Notably, for combinations of IBX II and TRIS, and the plutonium point source, the pit, and the BeRP ball, the algorithm suggests solutions without a PoBe source, relying instead on a combination of radioactive isotopes, as in the first hoax approach. The vulnerabilities of all combinations of confirmation systems and emission models at different ages are compiled in Table 6.4.

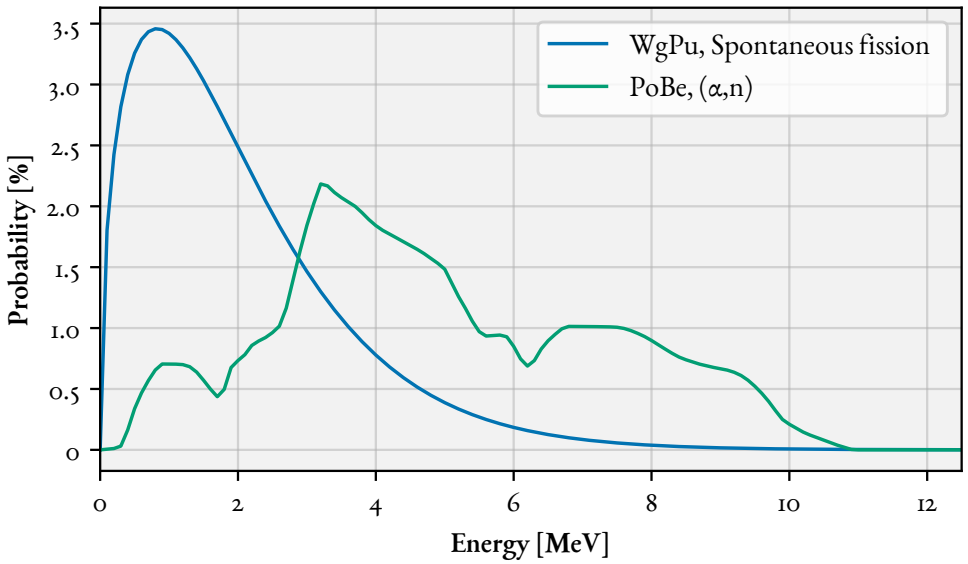

Figure 6.6: Neutron Energy Spectra: WGPu Spontaneous Fission, (α, n)-Source
For the (α, n)-source, a mixture of polonium-210 and beryllium-9 is used. Energy bins have a width of 100 keV.

6.3.3 Substituting Weapon-Grade with Reactor-Grade Plutonium

In the third hoax scenario, the warhead's WGPu pit is replaced with a thin shell of RGPu, without additional isotopes on the exterior, to isolate the effects of plutonium replacement. For the point source, the pit, and the BeRP ball, the entire object is replaced with an RGPu source.

In contrast to WGPu, which is produced through low burnup, RGPu is produced automatically during the regular operation of a power reactor. Like WGPu, it is separated from the spent nuclear fuel after the burnup. The longer irradiation time of the produced plutonium-239 makes it absorb additional neutrons, resulting in a higher content of the heavier plutonium isotopes.[6] The neutron emission rate of RGPu is higher than that of WGPu due to the higher amount of even plutonium isotopes, and the photon emission rate of RGPu is higher than that of WGPu due to the greater americium-241 content. Further, due to α-decays of the plutonium-240, RGPu produces about 5–6 times more heat than WGPu [257].[7]

As there are different reactor operations, there is no universal definition of RGPu. In the following, I use the composition of 30-year-old "270 Power Grade Plutonium" [159], assumed in the following to be 30 years old. Similar to the composition and emissions of WGPu in Table 5.2, the composition and emissions of RGPu were determined in Table 6.2. To identify the hoax object, I employed a Newton-based optimization algorithm to determine the required amount of RGPu replacing the weapon's pit to best match the object's signature. Due to its

	0 a	10 a	20 a	30 a	40 a	50 a
Plutonium-238 [wt%]	0.990	0.915	0.845	0.781	0.722	0.667
Plutonium-239 [wt%]	62.380	62.362	62.344	62.326	62.308	62.290
Plutonium-240 [wt%]	21.780	21.757	21.734	21.711	21.688	21.665
Plutonium-241 [wt%]	11.880	7.317	4.506	2.775	1.709	1.053
Plutonium-242 [wt%]	2.970	2.970	2.970	2.970	2.970	2.970
Americium-241 [wt%]	0.000	4.524	7.238	8.839	9.756	10.252
Neutron production [10^4 kg^{-1}s^{-1}]	30.17	29.96	29.76	29.57	29.39	29.22
Photon production [10^9 kg^{-1}s^{-1}]	8.08	2,078.46	3,312.90	4,040.91	4,457.52	4,682.86

Table 6.2: RGPu's Composition, Photon- and Neutron Production Rates
I assume the composition of "270 Power Grade Plutonium" [159]. The photon particle production rates include only photons from γ-decay, with an energy above 50 keV. The neutron production rate includes only neutrons from spontaneous fission. Older compositions were determined by calculating the decay of respective nuclides.

higher radioactivity, significantly less RGPu is needed than WGPu, resulting in a hoax emitting fewer neutrons than the original model. This discrepancy arises from the self-shielding effect of photons in plutonium, whereas neutron emissions tend to increase due to induced fission reactions. The effect is illustrated in Figure 6.7 on the left, showing the overall neutron and photon emission rates for different amounts of RGPu for the W78-RV with the plutonium pit replaced with a shell of RGPu. The data reveal that while neutron emissions increase with the amount of RGPu, photon emissions reach a saturation point due to self-shielding.
For the example of the W78-RV, the optimization process resulted in a need for 62 g of RGPu to generate the same number of photon emissions in the hoax compared to the original W78-RV model. The high-resolution detector response for this hoax compared to the spectrum of the W78-RV hoax is shown in Figure 6.7 on the right. This hoax is indistinguishable from a 30-year-old W78-RV warhead when examined with IBX II or TRIS.
Hoaxes in which WGPu is replaced with RGPu are particularly effective for objects in which all photon emissions from the plutonium pit are heavily shielded, as their signature is dominated by the photon emission sfrom uranium components and by (n, γ)- and (n, n', γ)-reactions induced by neutrons emitted from the pit. This is the case for tampered weapons as the FPS model, but also for the W87-RV model, where the thick shell of chemical explosives produces a strong shielding effect. For these objects RGPu hoaxes can successfully mimic high-resolution gamma spectroscopy measurements, including those used in IBX.[8] Due to the distinct differences in the photon emission spectrum, RGPu hoaxes cannot replicate the signature of emission models composed solely of plutonium, making them directly detectable. The vulnerabilities of all combinations of confirmation systems and emission models at different ages to this hoax are summarized in Table 6.4.

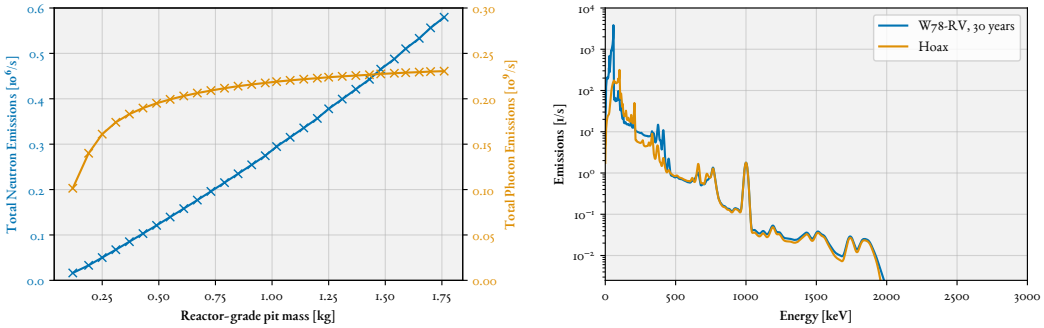

Figure 6.7: Photon and Neutron Emissions of RGPu in the W78-RV
The left shows the hoax's total photon and neutron emissions for different amounts of reactor-grade plutonium. The right shows the detected photon spectrum for W78-RV (30 years old) and a hoax that fools the IBX II or TRIS confirmation systems, made out of 62 g reactor-grade plutonium.

6.3.4 Replacing Parts of the Plutonium with Californium-252

The fourth hoax exploits photon self-shielding effects inside the plutonium (see Figure 6.7) and represents a very challenging cheating scenario to detect. Since only photons from γ-decay of the surface nuclides influence the photon emission spectrum, a malicious actor could replace portions of the inner WGPu with a californium-252 neutron source to match the total neutron emission rate while secretly withholding weapons-grade material.[9]
Compared to an (α, n)-source, the spontaneous fission neutrons from californium-252 exhibit an energy spectrum nearly identical to that of spontaneous fission neutrons from WGPu.[10] Californium-252 is not a pure neutron source but produces additional γ-rays. One gram of californium-252 additional produces: 43.4 keV ($2.94 \cdot 10^9$ γ/s), 100.2 keV ($2.58 \cdot 10^9$ γ/s), 155.1 keV ($1.04 \cdot 10^8$ γ/s), and 207.4 keV ($5.75 \cdot 10^6$ γ/s).[11] Simulations revealed that 1 mm of WGPu shields 100.0%, 94.9%, 97.8% and 85.0% of theseγ-rays, respectively. The 155.1 keV γ-ray is absorbed more than the 100.2 keV γ-ray because the latter's energy lies below plutonium's K-shell binding energy (K-edge) at 121.79 keV.

Optimization Process

A Cf-252 hoax is characterized by the remaining mass of WGPu (M_{WGPu}) and the amount of californium-252 ($M_{\text{Cf-252}}$) placed at its center. Identifying such a hoax is an optimization problem, where $M_{\text{Cf-252}}$ is the search parameter. The hoax was determined by solving for the amount of californium-252 required to match the total neutron emissions (N_{em}) of a given template (T). For solving the problem, it was reformulated as a root-finding problem:

$$f(T, M_{\text{WGPu}}, M_{\text{Cf-252}}) = N_{\text{em}}(T) - N_{\text{em}}(\text{hoax}(M_{\text{WGPu}}, M_{\text{Cf-252}})) \tag{6.3}$$

where f maps to the difference in neutron emissions between the template and the hoax. To solve this problem, I implemented a Newton-like optimization algorithm, approximating the derivative via finite differences:

$$\frac{\partial f(M_{\text{Cf-252}})}{\partial M_{\text{Cf-252}}} \approx \frac{f(\delta_{M_{\text{Cf-252}}}) - f(M_{\text{Cf-252}})}{\delta_{M_{\text{Cf-252}}}}. \tag{6.4}$$

The algorithm iteratively perturbs $M_{\text{Cf-252}}$ by a small step $\delta_{M_{\text{Cf-252}}}$, evaluates the resulting change in neutron emissions, and updates the estimate until the difference in emissions is sufficiently small.

Results

As an illustrative example, this hoax strategy is demonstrated for the BeRP ball, verified with the MCTM system (as in the MCTM introducing publication [18]).[12]
Figure 6.8 shows the neutron emission spectrum (left) and the measured high-resolution gamma spectrum using the introduced scintillation gamma detector (right) for the original BeRP ball and a hoax in which 650.84 g of plutonium from the center is replaced with 0.075 µg californium-252 — an amount determined through optimization. The neutron emission spectra are almost identical, suggesting similar responses across various neutron detectors (e.g., the helium-3 neutron detector used during the INF inspections [33] or the indirect measurement in the MCTM system [18]). Also, the measured high-resolution gamma spectra from the BeRP ball and its corresponding hoax are indistinguishable.

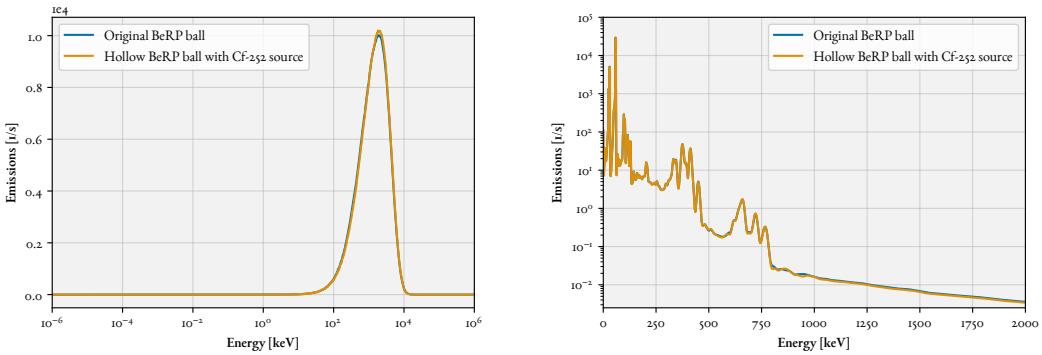

Figure 6.8: Neutron Emissions and Gamma Spectrum of a Californium-252 Hoax
The energy distribution of the neutron emissions (left) and the high-resolution gamma spectrum in the IBX system (right) for the BeRP ball in blue and a hoax by removing 650.84 g of plutonium from the center (caveat radius of 1.9938 cm) and replacing it with 0.075 µg californium-252.

In Figure 6.9 it can be seen that the original BeRP ball and its hoax produce an identical signature in the MCTM system. It can be seen that compared to the measured spectrum

with the IBX system (Figure 6.8 on the right), by the mask in front of the detector, many of the photons get scattered before getting detected, leading to a much lower resolution of the detected spectrum.

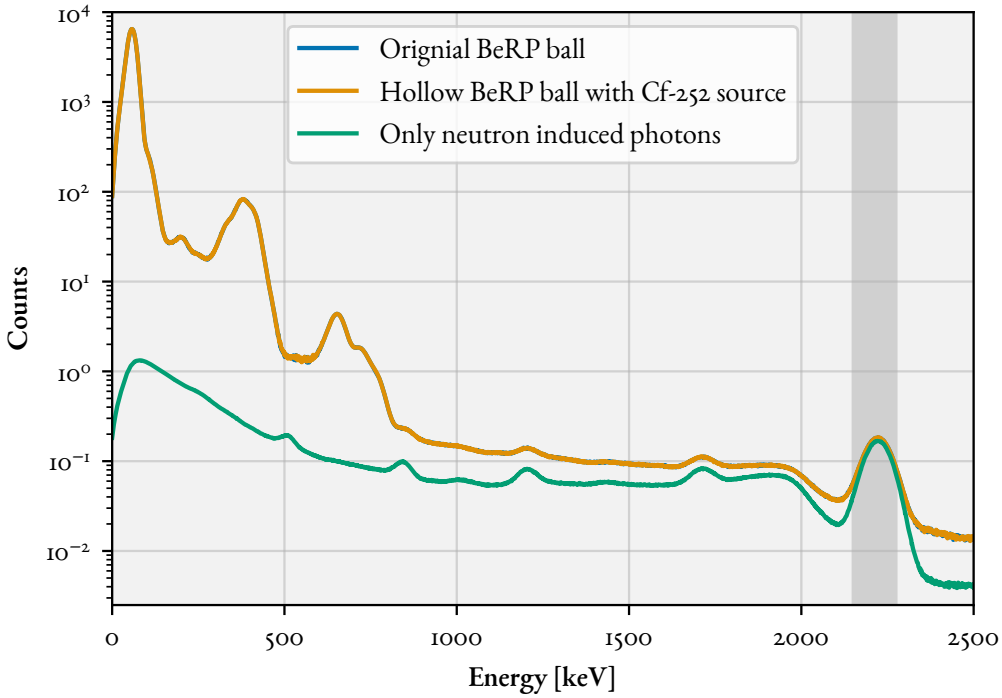

Figure 6.9: MCTM-Measured Spectrum of a Californium-252 Hoax
The measured spectrum of the original BeRP ball and a hoax in which 650.85 g of plutonium from the inner is replaced with 0.075 µg of californium-252. The number of counts was normalized to 2^{18}. Only 0.2% of the detected photons originate from neutron emissions from the BeRP ball. Their theoretical sole contribution to the resulting gamma spectrum is also shown.

Table 6.3 summarizes the simulated total neutron and photon emissions of the BeRP ball, with different amounts of the inner part being removed. Additionally, this table provides the amount of californium-252 needed to place in the center of the hollowed BeRP ball to obtain the same number of neutron emissions as the so-created hoax. All these hoaxes pass the Kolmogorov-Smirnov test of MCTM.
Cf-252 hoaxes for all emission models are not detectable by any of the analyzed confirmation systems. With the plutonium point source being the only exception, as self-shielding effects are absent. Cf-252 hoaxes were optimized for all introduced emission models of different ages to replace 500 g of the WGPu with californium-252. The results for the different confirmation system and emission model combinations are provided in Tabel 6.4.

Cavity radius [cm]	Mass [g]	Emission ($\pm\sigma$) [10^5 neutrons/s]	Emission ($\pm\sigma$) [10^8 gammas/s]	$M_{\text{Cf-252}}$ [µg]	MCTM KS-test
0.0	4483.91	8.523 ± 0.056	5.694 ± 0.054	—	—
0.9938	4403.31	7.772 ± 0.045	5.694 ± 0.054	0.010	0.000
1.9938	3833.06	4.998 ± 0.023	5.693 ± 0.050	0.075	0.000
2.4938	3210.35	3.438 ± 0.012	5.694 ± 0.045	0.139	0.000
2.9938	2280.46	1.993 ± 0.005	5.691 ± 0.038	0.223	0.000
3.4938	981.82	0.698 ± 0.001	5.689 ± 0.025	0.316	0.000

Table 6.3: Total Neutron and Photon Emissions of Modified BeRP Ball
The total neutron and photon emissions from the BeRP ball with different amounts of the inner part being removed. The amounts were adopted to match the exemplary results given in Table 1 in [18], whereby the minor differences result from the different specifications of the BeRP ball (compare Section 5.3.1). Further, the amount of californium-252 needed to obtain the same number of neutron emissions as the intact BeRP ball and the Kolmogovo-Smirnov test result between the BeRP ball and the californium-252 hoax is given.

6.4 Overview of Cheating Possibilities*

I analyzed the four hoaxes described above across the four warhead confirmation systems (IBX, IBX II, TRIS, MCTM) for the following eight theoretical emission models (see Section 5.3): a plutonium point source, a plutonium pit, the BeRP ball, the FPS model, a W78 and a W87 warhead with and without their reentry vehicle. The age of the emission models varied from new to 50 years old. Table 6.4 summarizes the systems' vulnerability to cheating.
It can be observed that hoax resistance does not significantly depend on the age of the warhead; rather, it is primarily influenced by the general warhead design.

*Parts of this section are based on the following publication, which primarily builds upon my own work and has been further expanded here:

- **C. Fichtlscherer**, M. Kütt. "Uniqueness, Reproducibility and Discrimination of Nuclear Warhead Gamma Signatures". In: *Science & Global Security* 32.1–3 (2024). DOI: 10.1080/08929882.2024.2387966

		Nuclide Hoax						Po-Be Hoax						RGPu Hoax						Cf-252 Hoax					
	Age [years]	0	10	20	30	40	50	0	10	20	30	40	50	0	10	20	30	40	50	0	10	20	30	40	50
IBX	Point source	✓	✓	✓	✓	✓	✓	✓	✓	✓	✓	✓	✓	✓	✓	✓	✓	✓	✓	✓	✓	✓	✓	✓	✓
	Pit	✓	✓	✓	✓	✓	✓	✓	✓	✓	✓	✓	✓	✓	✓	✓	✓	✓	✓	×	×	×	×	×	×
	BeRP	✓	✓	✓	✓	✓	✓	✓	✓	✓	✓	✓	✓	✓	✓	✓	✓	✓	✓	×	×	×	×	×	×
	FPS model	✓	✓	✓	✓	✓	✓	✓	✓	✓	✓	✓	✓	×	×	×	×	×	×	×	×	×	×	×	×
	W78	✓	✓	✓	✓	✓	✓	✓	✓	✓	✓	✓	✓	✓	✓	✓	✓	✓	✓	×	×	×	×	×	×
	W78-RV	✓	✓	✓	✓	✓	✓	✓	✓	✓	✓	✓	✓	✓	✓	✓	✓	✓	✓	×	×	×	×	×	×
	W87	✓	✓	✓	✓	✓	✓	✓	✓	✓	✓	✓	✓	×	×	×	×	×	×	×	×	×	×	×	×
	W87-RV	✓	✓	✓	✓	✓	✓	✓	✓	✓	✓	✓	✓	×	×	×	×	×	×	×	×	×	×	×	×
IBX II	Point source	×	×	×	×	×	×	×	×	×	×	×	×	✓	✓	✓	✓	✓	✓	✓	✓	✓	✓	✓	✓
	Pit	×	×	×	×	×	×	×	×	×	×	×	×	✓	✓	✓	✓	✓	✓	×	×	×	×	×	×
	BeRP	×	×	×	×	×	×	×	×	×	×	×	×	✓	✓	✓	✓	✓	✓	×	×	×	×	×	×
	FPS model	○	○	○	○	○	○	○	○	○	○	○	○	×	×	×	×	×	×	×	×	×	×	×	×
	W78	×	×	×	×	×	×	×	×	×	×	×	×	×	×	×	×	×	×	×	×	×	×	×	×
	W78-RV	×	×	×	×	×	×	×	×	×	×	×	×	×	×	×	×	×	×	×	×	×	×	×	×
	W87	×	×	×	×	×	×	×	×	×	×	×	×	×	×	×	×	×	×	×	×	×	×	×	×
	W87-RV	×	×	×	×	×	×	×	×	×	×	×	×	×	×	×	×	×	×	×	×	×	×	×	×
TRIS	Point source	×	×	×	×	×	×	×	×	×	×	×	×	✓	✓	✓	✓	✓	✓	✓	✓	✓	✓	✓	✓
	Pit	×	×	×	×	×	×	×	×	×	×	×	×	✓	✓	✓	✓	✓	✓	×	×	×	×	×	×
	BeRP	×	×	×	×	×	×	×	×	×	×	×	×	✓	✓	✓	✓	✓	✓	×	×	×	×	×	×
	FPS model	×	×	×	×	×	×	×	×	×	×	×	×	×	×	×	×	×	×	×	×	×	×	×	×
	W78	×	×	×	×	×	×	×	×	×	×	×	×	×	×	×	×	×	×	×	×	×	×	×	×
	W78-RV	×	×	×	×	×	×	×	×	×	×	×	×	×	×	×	×	×	×	×	×	×	×	×	×
	W87	×	×	×	×	×	×	✓	✓	✓	✓	✓	✓	×	×	×	×	×	×	×	×	×	×	×	×
	W87-RV	×	×	×	×	×	×	×	×	×	×	×	×	×	×	×	×	×	×	×	×	×	×	×	×
MCTM	Point source	✓	✓	✓	✓	✓	✓	✓	✓	✓	✓	✓	✓	✓	✓	✓	✓	✓	✓	✓	✓	✓	✓	✓	✓
	Pit	✓	✓	✓	✓	✓	✓	✓	✓	✓	✓	✓	✓	✓	✓	✓	✓	✓	✓	×	×	×	×	×	×
	BeRP	✓	✓	✓	✓	✓	✓	✓	✓	✓	✓	✓	✓	✓	✓	✓	✓	✓	✓	×	×	×	×	×	×
	FPS model	✓	✓	✓	✓	✓	✓	✓	✓	✓	✓	✓	✓	×	×	×	×	×	×	×	×	×	×	×	×
	W78	✓	✓	✓	✓	✓	✓	✓	✓	✓	✓	✓	✓	✓	✓	✓	✓	✓	✓	×	×	×	×	×	×
	W78-RV	✓	✓	✓	✓	✓	✓	✓	✓	✓	✓	✓	✓	✓	✓	✓	✓	✓	✓	×	×	×	×	×	×
	W87	✓	✓	✓	✓	✓	✓	✓	✓	✓	✓	✓	✓	×	×	×	×	×	×	×	×	×	×	×	×
	W87-RV	✓	✓	✓	✓	✓	✓	✓	✓	✓	✓	✓	✓	×	×	×	×	×	×	×	×	×	×	×	×

Table 6.4: Summary of Cheating Vulnerabilities

AThe analysis covered objects aged 0, 10, 20, 30, 40 and 50 years. A cross ("×") marks cases where hoaxes are possible, while a check mark ("✓") indicates resistance to hoaxes. For nuclide-based hoaxes, a circle ("○") highlights cases where specific nuclide compositions can be achieved, though the necessary nuclides are unavailable from the DOE Isotope Program.

Notes

[1]According to [22] the US produces its heavy-metal weapon components with a tolerance up to 0.0508 mm. This could already result in significant differences as, for example, the mean-free-path of the strongest uranium γ-ray at 186 keV is about 4 mm in uranium [202], which would result in the extreme case in an intensity difference of 2.5%. Therefore, in [22], selecting more than one golden sample to determine the variability between the warheads is suggested.

[2]Evidently, cost-benefit considerations constrain the utility of hoax objects; if the cost of creating a hoax objects exceeds that of another option to achieve the desired strategic advantage, the hoax is not practical. A state could, for example, clandestinely produce an additional warhead.

[3]In a declassified description of the warhead dismantlement process at the Pantex Plant it is stated that "*within 72 hours of arrival at Pantex, gamma spectroscopy and/or neutron detection verification of each warhead is performed*" [10].

[4]Since SOURCES4C is not open-source and requires obtaining a copy through the Radiation Safety Information Computational Center (RSICC), Dr. Moritz Kütt ran the code and provided me with the results.

[5]This effect is even more pronounced for oxygen — not considered in the models. The 6.13 MeV γ-ray, produced by inelastic scattering in oxygen, is 18.11 times more likely to be generated by neutrons from a PoBe source than those from a plutonium source.

[6]The higher amount of plutonium-238 results from a neutron capture of americium-241, with subsequent β^+ and α-decays.

[7]The higher activity and heat generation of RGPu challenges the suitability of existing facilities designed for manufacturing pits with conventional weapons-grade plutonium for manufacturing RGPu pits for hoax objects.

[8]Notably, for heavily tampered weapons, where gamma emissions from the pit do not reach the detector, alternative neutron sources with an energy spectrum similar to that of the WGPu pit could also be utilized.

[9]Such an hoax approach for the MCTM system was already mentioned in [18]. Still, no further attention was given as this would "*run the risk of generating additional detectable signatures.*"

[10]Though californium-252 is costly, reaching prices of up to $27 million per gram [259], it serves as a highly effective neutron source, producing approximately $2.3 \cdot 10^{12}$ $^{n}/_{s \cdot g}$ [260]. As an example, a californium-252 sample of 37.05 µg, costing about $10 would have a neutron emission rate of $8.54 \cdot 10^{5}$ $^{n}/_{s}$, the same as the BeRP ball (compare Table 5.8).

[11]Encasing the californium-252 source in a material like tungsten, which has a high density of $19.3\,{}^{g}/_{cm^3}$ and offers strong photon shielding while maintaining low neutron absorption — particularly for fast neutrons [261] — could effectively block γ-rays. However, (n, γ) and $(n, n'\,\gamma)$ reactions in tungsten would produce additional photons.

[12]The simulated composition used was "simulated (01/2024)", detailed in Table 5.7.

Chapter 7

Adapting Measurement Systems

In Chapter 6, I showed that warhead signatures frequently lack both soundness and completeness. Despite these vulnerabilities, especially low-resolution gamma spectroscopy remain highly attractive for warhead confirmation due to its inherent privacy-preserving nature. Unlike information barriers, which are susceptible to hacking, these systems rely on a small number of broad spectral bins, they simplify data collection while minimizing information exposure. To address the existing limitations of low-resolution gamma spectroscopy, this chapter introduces optimized bin structures explicitly designed to enhance robustness against deception attempts, thereby mitigating the weaknesses identified earlier. These optimized structures were derived with a specially designed genetic algorithm.

7.1 Optimizing Bin Structures*

As discussed earlier, various measurement methods exist for confirming nuclear warheads. Solely neutron emission count-rate measurements, such as those conducted under the INF treaty (see Section 2.1), lack robustness since neutron emissions can be mimicked by alternative neutron sources [43]. Conversely, a confirmation that relies solely on photon emission measurements is vulnerable to internal self-shielding effects, potentially allowing the covert removal of weapon-grade plutonium without detection, as demonstrated by [18]. Combined neutron-gamma systems, like the MCTM, aim to overcome these limitations by measuring neutron

*Parts of this section are based on the following publications, which primarily build upon my own work and have been further expanded here:

- **C. Fichtlscherer**, M. Kütt. "Uniqueness, Reproducibility and Discrimination of Nuclear Warhead Gamma Signatures". In: *Science & Global Security* 32.1–3 (2024). DOI: 10.1080/08929882.2024.2387966
- **C. Fichtlscherer**, M. Kütt. "Improving Warhead Authentication using Gamma Spectroscopy". In: *65th Annual Meeting of the Institute of Nuclear Materials Management (INMM)*. 2024. URL: https://cdn.fourwaves.com/static/media/formdata/b12613f9-28b7-4568-a069-5c7cfeff3c8e/21b15233-1c7f-4a44-a2e5-bf980042b9e5.pdf (visited on 02/25/2025)

and photon emissions simultaneously. However, as shown in Section 6.3.4, significant self-shielding, which allows the removal of fissile material without influencing the warhead's photon emissions, inherently permits replacing fissile material with neutron sources like californium-252. This occurs because the same self-shielding that hides material removal likewise hides photons from a replacement neutron source. Consequently, combined neutron-gamma measurements only hardly offer improved detection capability over gamma-only measurements; any cheating scenario detectable by the MCTM system is also identifiable using gamma-only systems like IBX (see Table 6.4).
My analysis of cheating scenarios presented in Chapter 6 indicates that when plutonium is heavily shielded (as for the FPS model and the W-87 model) or against a scenario in which alternative neutron sources partially replace fissile material, passive measurements of photon and neutron emissions are inadequate. More invasive verification methods, such as physically opening the warhead, would become necessary.
As neutron emission measurements provide no additional advantage in other analyzed cheating scenarios, this chapter will exclusively focus on photon emission measurements. Moreover, the investigation will specifically target scenarios accessible through gamma-spectroscopic techniques, as IBX — unlike IBX II and TRIS — can detect hoaxes involving combinations of radioactive isotopes.
Throughout this chapter, my analysis is restricted to the following four theoretical emission models: the plutonium pit, the W78-RV, the W87-RV, and the FPS model (for detailed discussion, see Chapter 5).

Increased Resolution

The fundamental principle of low-resolution gamma spectroscopy, is to preserve privacy by capturing key characteristic photon emissions using large spectral bins. For example, the bin structure of TRIS was determined by carefully evaluating significant photon emissions of nuclear weapons (see Section 5.2). As a result, TRIS utilizes 14 energy bins of varying widths between 0 keV and 2,750 keV, while IBX II employs 12 equally spaced bins between 0 keV and 2,950 keV (see Table 3.2). Although in conflict with the privacy-preserving principles of low-resolution gamma spectroscopy, a straightforward approach to detecting nuclide hoaxes is to increase the detector resolution. My initial analysis examines how many equally spaced energy bins are required to detect nuclide hoaxes reliably across different weapon emission models. Specifically, I evaluated the χ^2-test between the true emission model and the best possible nuclide hoax, determined as described in Chapter 6, for varying numbers of energy bins between 0 keV and 3,000 keV. The optimization process was based solely on the first term of the minimization problem in Equation 6.1, disregarding multi-day inspections and the preference for a limited number of nuclides. Similar to IBX II an object is rejected for χ^2-test values above 100. Figure 7.1 illustrates the outcomes of these χ^2-test results between the emission models and the most effective hoaxes identified. The analysis incorporated the point source, pit, and warhead models previously discussed, each aged to 30 years.

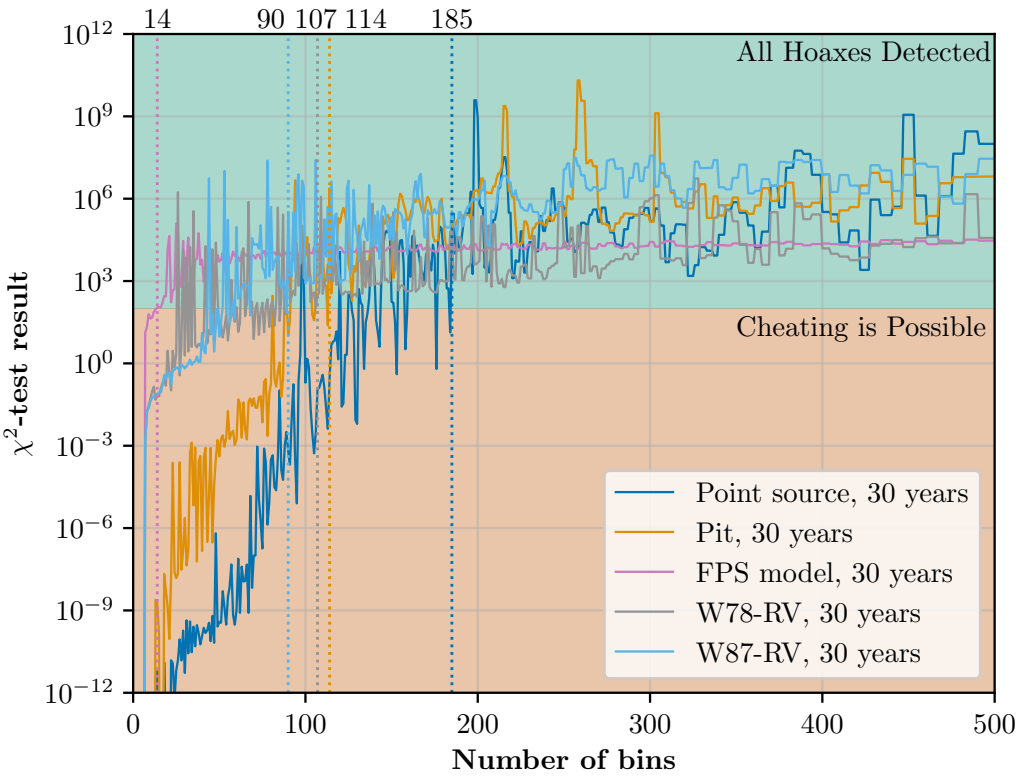

Figure 7.1: Best Hoax Chi-Square-Test Results vs. Energy Bins
The measurement of the gamma spectrum with an increasing number of equally-sized energy bins between 0 and 3,000 keV was simulated. The corresponding χ^2-test results are shown between the best hoax for the respective bin number and emissions from various emission models. Dotted lines indicate the resolution beyond which the system can be considered secure with a significance level of 100, assuming 2^{18} recorded counts during the measurement.

The demonstrates reveals that a higher detector resolution leads to detection of nuclide hoaxes, though the required level of resolution varies significantly depending on the emission model. While 14 energy bins are already sufficient for the FPS model, the plutonium point source requires up to 185 energy bins for effective hoax detection. However, while an increased resolution will allow for the detection of isotopic hoaxes, it will make it even harder to confirm same-type-different-age objects. Figure 7.2 illustrates this effect by comparing the plutonium point source, the pit, and the W78-RV model at different ages, using 185, 114, and 107 energy bins, respectively — the lowest resolutions at which all nuclide hoaxes are detected. The results indicate worse performance than TRIS and IBX II (see Figure 6.2).

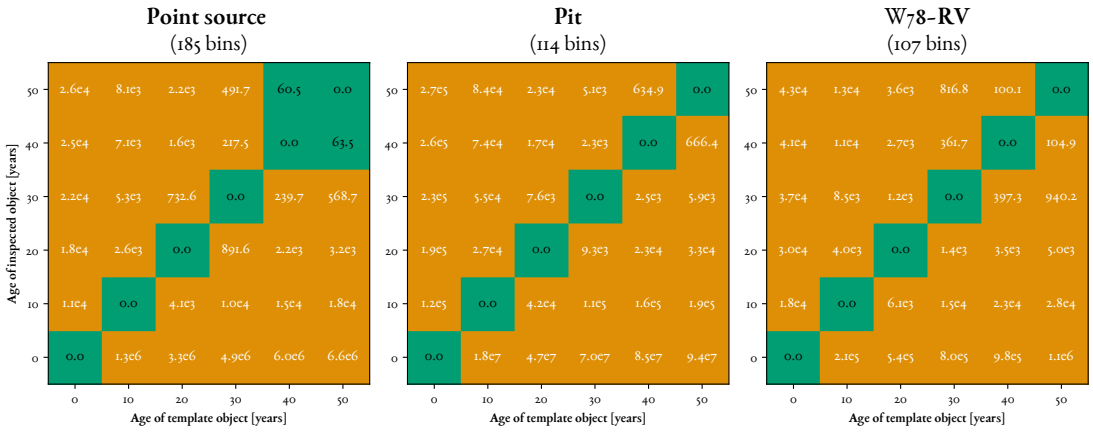

Figure 7.2: Non-Completeness of Gamma Signatures with Increased Resolution
The measurement of the passive plutonium point source, pit, and W78-RV gamma spectrum using 185, 114, and 107 equally-sized energy bins, respectively, between 0 and 3,000 keV were simulated. The χ^2-test results between different aged models with that bin structure using 2^{18} counts in the measurement and a threshold value of 100 have been calculated. An orange background indicates that the objects are different, and a green background indicates that the objects are identical.

7.1.1 Using a Genetic Algorithm to Find Improved Bin Structures

For simultaneously addressing nuclide hoaxes and assure the successful confirmation of same-type-different-age objects a more sophisticated bin structure is necessary. To determine such bin structures, I formulate these requirements as an optimization problem and solve it using a genetic algorithm.

Introduction to Genetic Algorithms

Genetic algorithms share a fundamental idea with neural networks: in the absence of a deep understanding of intelligence, they mimic natural processes known to produce intelligent outcomes — neural networks emulate brain structures, while genetic algorithms imitate evolutionary processes [262]. Despite the success of genetic algorithms in the neighboring field of nuclear engineering to optimize, for example, reactor design, their use in nuclear verification is novel [263–266].
The term "genetic algorithms" today refers to a blend of various methodologies that emerged in the latter half of the 20th century, evolving alongside advancements in computing to address complex optimization problems [267–269]. They are probabilistic optimization methods inspired by the principles of natural selection. But unlike random search methods, which generate solutions independently without leveraging insights from past outcomes, genetic

algorithms refine their search probabilistically by incorporating feedback from previous generations [270]. They are robust and can find global optima in complex, multimodal landscapes, where traditional optimization methods often fail [271]. Further, they are also appreciated for their domain-independent search capabilities, which allow them to outperform traditional "weak methods" without requiring highly specialized domain knowledge [272]. However, genetic algorithms can suffer from slow convergence rates and are highly sensitive to their initial hyperparameters. These issues can lead to premature convergence, where the algorithm settles on suboptimal solutions too early in the process [273, 274].
In principle, a genetic algorithm searches for optimal solutions by creating a diverse population of candidate solutions, each assessed and assigned a specific fitness value based on their suitability for the problem. Through an evolutionary process, the fittest individuals are subjected to mutation and crossover — mutation slightly alters a good solution in hopes of finding a superior nearby solution, akin to hill-climbing, while crossover aims to combine elements of multiple strong candidates to produce even better offspring [275, 276].

Generalization Optimization Problem of Low-Resolution Gamma Spectroscopy Warhead Confirmation

In a generalization of IBX II and TRIS, a low-resolution gamma spectroscopy warhead confirmation system measures the gamma spectra of a template T and a test object S with a certain energy bin structure and compares them via a weighted χ^2-test

$$\chi^2_{\mathrm{w}}(S,T) = \sum_{l=1}^{n} \omega_l \cdot \frac{(s_l - t_l)^2}{t_l}. \tag{7.1}$$

If χ^2_{w} is below a particular threshold value C, the two objects are considered to be identical. Here, s_l is the object under inspection and t_l are the template's counts in bin l, weighted by ω_l. I will assume that 2^{18} counts will be recorded for a spectrum (similar to IBX II [20]). The χ^2-test result scales with the number of counts. Therefore, the threshold value C and the number of counts can be adjusted together, for example, enabling faster measurements with fewer counts or more precise measurements, overcoming potential issues of wrong attribution due to statistical fluctuations in the measurement. The introduction of bin specific weights generalizes the χ^2-test and allows more flexibility for evaluating the spectrum. For example, as observed in Figure 5.3, some aspects of the gamma spectrum are more susceptible to aging due to gamma emissions from plutonium-241, while other aspects of the spectrum contain key warhead photon emissions (see Table 5.5).

The optimization problem consists of finding a weighted bin structure that allows confirmation of same-type different-age objects but is not susceptible to hoaxes made from decoy nuclides

$$\chi^2_{\mathrm{w}}(W_i, W_j) \leq C \qquad \text{and} \qquad \chi^2_{\mathrm{w}}(H, W_i) > C \qquad\qquad \forall i, j \in \{0, \ldots, 50\},$$

where W_i denotes the low-resolution passive gamma spectrum for a specific i-year-old weapon model W and H is the low-resolution passive gamma spectrum of the best nuclide hoax. In addition, I have formulated several constraints on the solution:

1. Bins have a minimum width of 5 keV.
2. The gamma spectrum is only considered from 100 keV to 1200 keV.
3. Weights take values between 0 and 100.

The first constraint prevents solutions with narrow bins around specific photon emissions and allows for calibration uncertainty. The second arises because γ-rays below 100 keV are hardly relevant due to shielding, above 1,200 keV there are no relevant photons that emerge from γ-decay in the plutonium and uranium anymore, as shown in Table 5.5. Only positive weights are permitted. As a weighted χ^2-test is with weights ω_i and a threshold value of C is equivalent to a χ^2-test with all weights and the threshold value multiplied by the same factor, the upper limit of 100 does not restrict the solution space but makes the weights more interpretable.

Description of the Algorithm

The algorithm searches for a solution with a predefined number of n energy bins.[1] In the *initialization*, a random population of 100 individual solutions is generated. The weight of every energy bin of these solutions is set to one. Solutions must fulfill specific constraints (described above), which can be complicated to implement, mainly since the optimum often lies at the border or corner of feasible solutions [276]. For the constraints 1 and 3 a *death penalty* approach was implemented — if a solution does not fulfill the constraints it is directly removed from the population.[2] The disadvantage of the death penalty is that it can be computationally heavy, as many solutions may be discarded.
To keep a similar generation size, the factor for how many additional individuals are created is dynamically adjusted by the reciprocal of the kill factor of the previous generation.
Each individual is assigned a *fitness* based on their ability to identify objects of varying ages as identical while being resistant to hoaxes. The fitness is the quotient of the minimum weighted χ^2-test result of the emission model to its best hoax and the maximum weighted χ^2-test result between all different age combinations of the emission model

$$\text{fitness} = \frac{\min \chi^2_{\mathrm{w}}(T_i, H)}{\max \chi^2_{\mathrm{w}}(T_j, T_k)}.$$

Here T_i, T_j, and T_k are emission models at different ages, while H is a hoax. A quotient above one is equivalent to reliable bin structures, meaning that even the best hoax to any emission model has a higher weighted χ^2-test result than any age combination of emission models. In the FPS model, the plutonium pit is surrounded by a heavy uranium tamper. Since the uranium absorbs all plutonium emissions and remains in a stable equilibrium, the emissions of the FPS model remain constant over time. Therefore, the fitness of the FPS model is set to the χ^2_{w}-test result of the model to its best hoax.

The five fittest individuals are considered the elite of a generation and form the initial members of the next generation. This *elitism* ensures the algorithm's convergence as it ensures that the highest fitness of an individual in the population does not decrease over generations.

The second part of the next generation is formed by *crossover*, combining elements from reasonable solutions (here, the elite) to achieve improved outcomes. This is done by randomly selecting energy bins from the fittest individuals of the previous generation. The underlying rationale is that these bin structures have proven effective in specific energy regions, and their random combination can lead to improved bin structures across multiple energy regions.

Mutation forms the third part of the next generation, assuming other reasonable solutions are near a good solution. A mutation is executed by shifting all bin borders slightly, moving the solution a small distance in a random direction. The fitness landscape of the weighted bin structures contains multiple optima. This presents a common optimization challenge: avoiding entrapment in local optima. To counteract this, the strategy of *novelty search* is employed, where random individuals are introduced into the next generation. Novelty search reduces the risk of getting confined to local optima and fosters greater exploration within the solution space.

Every fitness evaluation of an individual consumes computational resources. Ultimately, discovering effective solutions necessitates a balance between exploration and exploitation — should the algorithm devote more effort to optimizing promising solutions or finding new ones? Moreover, this balance may shift during the algorithm's execution: initially, it should explore the solution space extensively, but later focus on exploiting the best solutions. This adaptability is facilitated by employing dynamic rates for the next generation's composition. It is adjusted based on the fitness outcomes from previous crossover, mutation, and novelty search implementations by *Rechenberg's control* [267]. This is done by calculating the average fitness of the individuals generated through crossover, mutation, and novelty search. The method with the highest average fitness is then used for 60% of the next generation, with the remaining methods used 30% and 10% of the time, respectively. Setting a minimum threshold for production rates ensures that no method is completely excluded. The specific percentages have been determined through multiple trial-and-error iterations. With this new generation of individuals, the algorithm starts all over again.

If the maximum fitness stays constant for over five generations, the algorithm adjusts the

weights instead of the bins. For this purpose, the bin borders from the previous generation's elite (the five most promising bin structures) are retained, but the bin weights are adjusted using a genetic algorithm. The new generation of weights is formed by elitism (taking the best-performing weights to the next generation), two types of mutation (shifting all weights slightly in a random direction and replacing the weight of one bin with a random weight), and novelty search (adding random weights to the generation). If the maximum fitness again remains constant over five generations, the algorithm will switch back to adjusting the borders of the bins. This way, the algorithm will iteratively adjust the bins and the weights until a predefined fitness value is reached or a maximum number of iterations is exceeded. Meaning the genetic algorithm adjusts the solutions based on previous outcomes and fine-tunes the optimization parameters according to the algorithm's past performance. This meta-level adaptation influences the quantity of individuals produced, the methods of their production, and the optimization of bins or weights. A structural overview of the algorithm is given in Figure 7.3.

1. Initialization
The algorithm is initiated with a random population of energy bin structures, with all weights equal to one.

2. Death Penalty
Individuals who do not fulfill secondary conditions are removed from the population.

3.1 Fitness Evaluation
The fitness of every individual in the population is evaluated.
3.2 Adaptive Composition
Based on the fitness outcomes from the previous generation's Elitism, Crossover, Mutation, and Novelty Search, the composition percentages for the next generation are dynamically adjusted.

If there was no improvement of the strongest individual over the past five generations, the algorithm switches between 4A and 4B.

4A.1 Building the new Generation (adjusting bin boarders) — Elitism
The individuals with the best fitness are selected as the first part of the next generation.
4A.2 Building the new Generation (adjusting bin boarders) — Crossover
The second part of the next generation is created by choosing random bin combinations from the fittest individuals.
4A.3 Building the new Generation (adjusting bin boarders) — Mutation
The third part of the next generation is created by changing the bin borders of the fittest individuals with a Gaussian.
4A.4 Building the new Generation (adjusting bin boarders) — Novelty Search
The fourth part of the generation is created by adding new random individuals.

4B.1 Building the new Generation (adjusting bin weights) — Elitism
The individuals with the best fitness are selected as the first part of the next generation.
4B.2 Building the new Generation (adjusting bin weights) — Mutation I
The second part of the next generation is created by changing the bin weights of the fittest individuals with a Gaussian.
4B.3 Building the new Generation (adjusting bin weights) — Mutation II
The third part of the next generation is created by changing the weight of one bin of the fittest individuals with a random weight.
4B.4 Building the new Generation (adjusting bin weights) — Novelty Search
The fourth part of the generation is created by adding new random bin weights.

5. Repetition or Termination
The algorithm is repeated with the new generation or terminates if a certain fitness or number of iterations is reached.

Figure 7.3: Structure of the Genetic Algorithm for Bin Structure Optimization
A structural overview of the genetic algorithm was developed to identify bin structures capable of verifying objects of the same type but different ages while being resistant to cheating attempts using any combination of radioactive nuclides as a point source.

Results

The algorithm was run ten times (initiated with different random seeds) for bin structures having 3 up to 20 bins for 2,000 generations and successfully determining reliable bin structures.

Since each object's emission characteristics differ, they require distinct bin structures. Thus, for verification procedures specifically designed to confirm plutonium pits, the "pit bin structure" would be appropriate. Conversely, the "all bin structure" could be effectively applied in confirmation processes involving any of the emission models under consideration. Figure 7.4 shows the fitness trajectories for several results found by the genetic algorithm. These results represent the bin structures identified as having the smallest resolution while still achieving a fitness value above one. For the "pit bin structure", 52.7%, the "W78-RV bin structure" II, 48.2%, the "W87-RV bin structure", 80.6%, the "FPS model bin structure", 60.8% and for the "all bin structure" 53.7% of the generations were changing the weights.

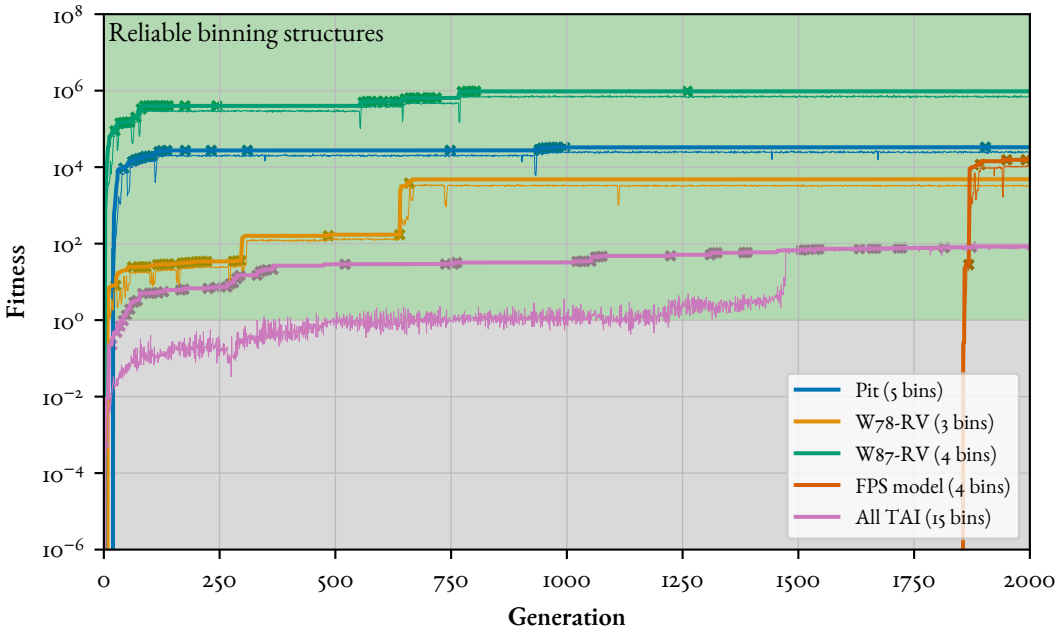

Figure 7.4: Fitness Trajectories Across Generations
The thick line traces the peak fitness of the strongest individual, whereas the thin line delineates the average fitness across the entire generation. Markers indicate shifts from adjusting bins to weights or the other way around. The legend indicates the resolution the genetic algorithm was optimizing for.

In Figure 7.5, these exemplary bin structures are displayed, along with gamma emissions associated with nuclear weapons already presented in Table 5.5. Energy bins with a weight

of zero are depicted in black. For comparison also, the bin structures of IBX II and TRIS are presented.[3]

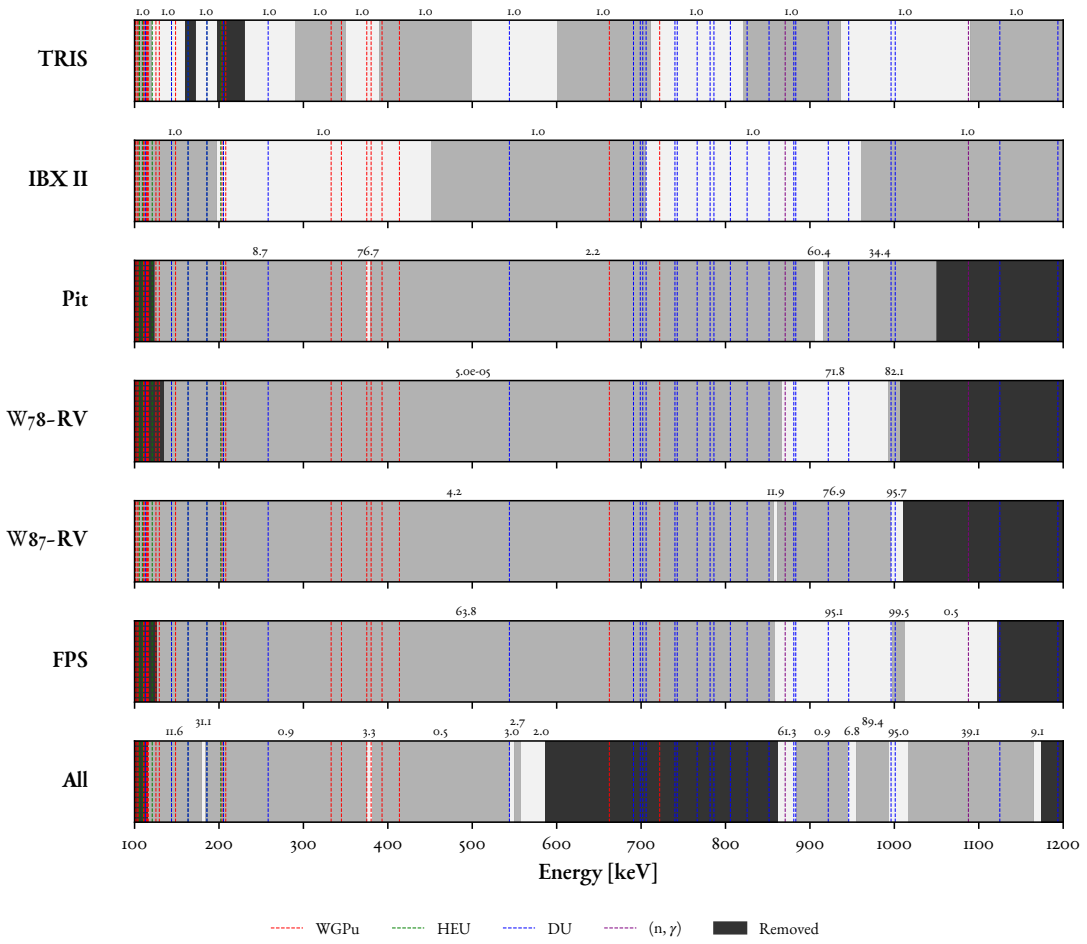

Figure 7.5: Exemplary Found Bin Structures
Bin structures are displayed alongside the nuclear weapons-related photon emission. For comparison, the bin structures of TRIS and IBX II are shown in the 100–1,200 keV energy region. Energy bins are displayed in white and gray for distinction, with their weight on top. The black background of an energy bin indicates its weighting with zero, signifying its removal.

Understanding the Bin Structures

The genetic algorithm yields a variety of reliable bin structures. Still, many of the solutions remain incomprehensible — they work, but it is hard to understand why — a typical problem from solutions obtained by "black-box" artificial intelligence methods. Nevertheless, some

distinct patterns emerge across the solutions. For instance, all bin structures except the "FPS model bin structure" assign minimal weights to bins in lower energy regions, where WGPu emits numerous γ-rays. These nuclides show significant temporal variations, mainly through the decay of plutonium-241 to americium-241. Therefore, reducing emphasis on these regions could enhance the system's ability to consistently identify objects of varying ages as equivalents. In the FPS model, temporal variations do not affect the emission spectrum because the uranium tamper absorbs all photon emissions from the pit.
The "pit bin structure" and "all bin structure" developed a bin targeting the 375.1 and 380.2 keV γ-rays of WGPu. Similarly, several bin structures include a bin to capture the two DU γ-rays at 996.1 and 1001.0 keV.
It can be seen that the genetic algorithm successfully identified operational bin structures by not only focusing on the critical photon emissions related to nuclear weapons but also creating bins that target specific hoax nuclides. Specific nuclides that could be used to create a hoax were targeted by additional bins capturing their supplementary photon emissions. For example, in the "pit bin structure", the bin spanning from 905.7 to 916.0 keV does not capture any weapon-related line, but the 914.0 keV γ-ray of barium-131. Barium-131 has a substantial γ-ray at 373.0 keV, which could be used to imitate the plutonium 375.1 keV line. Similarly, the bin structure for the W78-RV that targets the region from 856.7 to 862.2 keV, does not capture any weapon-related line, but the 856.7 keV γ-ray of antimony-126, which further has gamma emissions at 414.7 keV, 666.5 keV, and 720.7 keV, which are very close at the plutonium gamma emissions at 413.7 keV, 662.4 keV, and 722.0 keV. As a last example, the energy bin from 179.3 to 184.4 keV in the "all bin structure" captures the 181.0 keV γ-ray of europium-154. Another γ-ray of europium-154 is at 723.0 keV, which is very close to plutonium's γ-ray at 722.0 keV.[4]

Stability Analysis

The bin structures were optimized based on the underlying probability distribution of the gamma spectrum. However, in practical measurements, only a limited number of counts are recorded which could lead to a wrong attribution by measurement statistics. I assume 2^{18} recorded counts — leading to measurements times from approximately 6.5 hours for a FPS model, to 1.5 minutes for a W78-RV model.[5] High-weight bins may capture only a few counts, resulting in unreliable performance of the bin structures due to strong fluctuations. I conducted a stability analysis for each identified bin structure. This involved simulating over 1,000,000 measurements for valid emission models of different ages and measurements, assuming a malicious actor would try to sabotage the confirmation process by presenting the best isotopic hoax. An example of these distributions for measurements of the W87-RV is given in Figure 7.6. All the bin structures provided here are stable — none of the measurements were misidentified.[6]

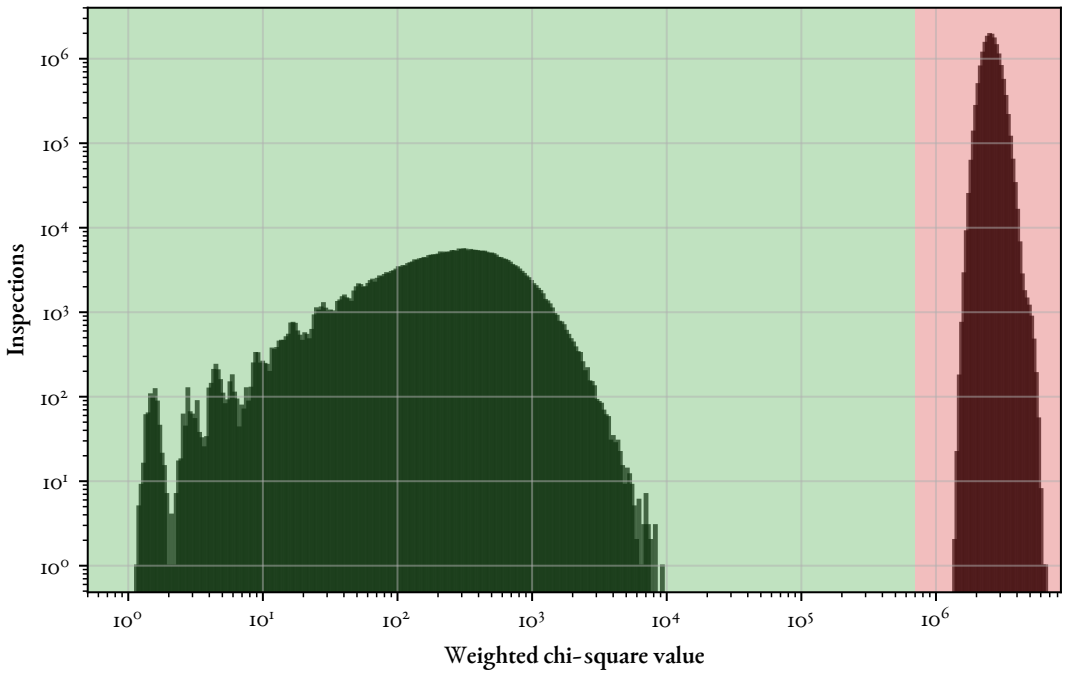

Figure 7.6: Stability Analysis for the W87-RV New Bin Structure
The χ^2_w-test result of over 1,000,000 measurements between different aged W87-RV warheads with each other and between them and their best hoax, assuming 2^{18} recorded counts have been determined. The background indicates which weighted χ^2-test results are still accepted and which are discarded. None of the simulated measurements was misidentified.

7.2 Potential Treaty Implementation and Information Content*

Potential Treaty Implementation

A practical warhead confirmation procedure based on the reliable signatures of determined weighted bin structures could proceed as follows: The host state initially agrees to dismantle

*Parts of this section are based on the following publications, which primarily build upon my own work and have been further expanded here:

- **C. Fichtlscherer**, M. Kütt. "Uniqueness, Reproducibility and Discrimination of Nuclear Warhead Gamma Signatures". In: *Science & Global Security* 32.1–3 (2024). DOI: 10.1080/08929882.2024.2387966
- **C. Fichtlscherer**, M. Kütt. "Improving Warhead Authentication using Gamma Spectroscopy". In: *65th Annual Meeting of the Institute of Nuclear Materials Management (INMM)*. 2024. URL: https://cdn.fourwaves.com/static/media/formdata/b12613f9-28b7-4568-a069-5c7cfeff3c8e/21b15233-1c7f-4a44-a2e5-bf980042b9e5.pdf (visited on 02/25/2025)

specified warheads and consents to verification based solely on their passive gamma emissions. Inspectors define photon sources such as isolated isotopes, shielded isotopes, or photon emissions from reactor-grade plutonium that are not allowed to produce the signal of the warhead in any combination. By defining these exclusion scenarios upfront, inspectors ensure that the measured signatures can distinguish genuine warheads from plausible hoax objects.

The host state employs the genetic algorithm described in the previous section to determine one or several bin structures. These structures are explicitly optimized to ensure that none of the predetermined photon sources could produce the signature of genuine warheads — the system is capable of detecting all hoax objects predefined by the inspectors — while at the same time giving consistent signals for the warheads of different ages. During this process, the host can also account for minor manufacturing differences. Importantly, because only the host knows which parts of the gamma spectrum contain classified information, the host alone selects bin structures that do not reveal confidential data.

If multiple suitable bin structures are defined, one is chosen randomly. To confirm that these bin structures are meaningfully distinct — and not trivially different by slightly shifting one spectral bin — the host can present comparative χ^2_{w}-test results obtained from unrelated radioactive sources. After selecting and sharing the bin structure with the inspectors, the host and inspectors jointly measure emissions from a representative "golden sample," randomly chosen from the host's active arsenal. For this measurement the new bin structure could be implemented in verification hardware like IBX II or TRIS. This template warhead's gamma spectrum is measured following a background measurement. The measurement can be performed on-site due to the relative insensitivity of gamma measurements to the surrounding compared to neutrons measurements that are often strongly scattered and reflected by the surrounding.

After the measurement, inspectors possess the bin structure and the measured counts within each bin, containing only information that has been released by the host. Using the provided optimization algorithm, inspectors verify that the measured spectrum cannot result from any defined photon source combination. Satisfied with this outcome, inspectors can confidently measure and confirm warheads intended for dismantlement, ensuring each passes the χ^2_{w}-test. Ideally, the host will have already conducted these verification measurements independently to validate the effectiveness of their chosen bin structures.

This verification method effectively reconciles two competing interests: it preserves the sensitive warhead information while allowing inspectors to conclusively verify that there was no hoax from other photon sources that can produce the measured spectrum. Unlike conventional methods (e.g., IBX, IBX II, TRIS, MCTM), which require the measurement of potentially classified spectral details, this approach reverses the problem — inspectors need only verify that measured emissions do not match predefined hoax scenarios. Thus, the host maintains complete control over the released information, while inspectors fulfill their primary objective of no hoax object instead of an actual warhead is dismantled.

Information Content

The underlying argument of low-resolution gamma spectroscopy is that it reduces the amount of the revealed information to a level that no longer contains sensitive information (see Chapter 2). The TRIS developers also note in a 2020 conference paper "*if the number of bins in the histogram is limited and the bin definitions are strategically chosen, the amount of information contained in the data available to the processor is also limited*" [277]. Even though they also denote that an ongoing effort is still to "*determine ... the ideal binning structure to be implemented*" [277]. However, there is still the question of how much information is revealed by low-resolution gamma spectroscopy, and future research could target the information content of low-resolution gamma spectroscopy [40].

Therefore, the TRIS measured counts in the 14 spectral bins are hidden behind an information barrier (IB), providing an extra layer of security. Inspectors see only a green or red light from the measurement. IBs have often been criticized for only shifting the problem of trust onto the technology (see Section 6.1), which is why it is usually assumed that IB-based systems will hardly generate the necessary trust needed for these processes.
The IBX II developers describe their system as having an option to combine this system with an information barrier [278], implying that inspectors may also be allowed to view count-rates of the spectral bins directly. This openness could raise privacy concerns, as the host country may fear sophisticated reverse engineering — only from these twelve spectral bins — could uncover sensitive weapon details.

The genetic algorithm developed in this study resolves these challenges by eliminating the need for an information barrier as the host maintains control over released information by strategically selecting an appropriate binning structure. At the same time the inspectors needs are satisfied by assuring that isotopic hoaxes are not present.
To exclude other hoax scenarios my research showed that the measurement of passive photon and neutron emissions is not sufficient and more intrusive methods would be required. No verification technology will serve as a definitive solution, as "*verification is too fragile to serve as the foundation for disarmament*" [29]. Thus, while verification technologies can enhance trust in a process and provide a platform for discussions, they remain secondary to the political will to disarm, as "*a verification regime only can reduce the likelihood of cheating by making it costly and risky, and by diminishing the magnitude of cheating that could go undetected. It cannot make undetected cheating impossible*" [280].

Notes

[1]Later, however, sometimes the algorithm assign bins a weight of zero, thus reducing the number of effectively used bins.

[2]For constraint 2, I run all simulations with already cut gamma spectra.

[3]Detailed bin structure results referenced in Figures 7.4 and 7.5:

Pit: Borders [keV]: 123.6, 373.9, 379.5, 905.7, 916.0, 1050.5; Weights: 8.71, 76.67, 2.21, 60.44, 34.39; Critical value C: 43898476.46; Fitness: 33205.67; Seed: 22; Generation found in: 1906.

W78RV: Borders [keV]: 134.7, 867.4, 993.0, 1007.2, 1034.7; Weights: 4.98e-05, 71.81, 82.13, 0.0; Critical value C: 491316632.73; Fitness: 4830.90; Seed: 25; Generation found in: 1113.

W87RV: Borders [keV]: 100.0, 856.7, 862.2, 996.0, 1010.0; Weights: 4.2, 11.91, 76.92, 95.73; Critical value C: 711853.04; Fitness: 962589.26; Seed: 27; Generation found in: 1262.

FPS: Borders [keV]: 126.8, 858.6, 998.2, 1012.7, 1122.3; Weights: 63.77, 95.09, 99.45, 0.49; Critical value C: 4451.59; Fitness: 16015.05; Seed: 26; Generation found in: 1994.

All: Borders [keV]: 116.4, 179.3, 184.4, 375.1, 380.7, 544.3, 549.9, 557.7, 585.9, 862.4, 884.2, 945.2, 954.8, 993.8, 1015.6, 1164.8, 1174.5; Weights: 11.57, 31.14, 0.91, 3.33, 0.53, 2.97, 2.74, 2.02, 0.0, 61.27, 0.91, 6.82, 89.38, 95.02, 39.14, 9.11; Critical values C: Pit: 3540898.16; W78RV: 30665106.01; W87RV: 2847572.93; FPS: 49304422.87; Fitness: 84.82; Seed: 24; Generation found in: 1876.

Critical values (C) determined from simulations of 1,000,000 measurements, taking the midpoint between the highest weighted χ^2-test result among true objects and the smallest weighted χ^2-test result between any hoax and a true object. Genetic algorithm utilizes Python's `random` and `numpy` packages, both seeded with the same value.

[4]This insight could also help create these bin structures manually in the future by not only focusing on the photon emissions from the emission model, but also the additional photon emissions of potential hoax nuclides.

[5]The FPS and W78-RV model are assumed to be 30 years old, the detector is placed 1 meter from the weapon, and it is assumed the detector has a 10% efficiency for the detection of γ-rays between 100–1,200 keV.

[6]This probability of correct assignment significantly exceeds the threshold deemed sufficient by existing literature [279].

Chapter 8

Conclusion and Outlook

The next generation of nuclear arms-control and disarmament treaties will benefit from viable verification measures confirming the authenticity of a warhead before dismantlement, if not require such measures. Such a verification regime, never before implemented, will require novel methods and technologies.

Many proposed systems — four of them are analyzed in this work — confirm warheads based on their passive photon and neutron emission signatures which allows for quick, simple, and portable measurements. However, substantial concerns about these emission signatures have been raised but not yet been addressed in the open literature. First, the completeness of the nuclear signature — the system's ability to correctly accept authentic warheads, even though they may have minor variations, such as those caused by warhead aging. Secondly, the soundness of the nuclear signature — the system's ability to reject hoax objects by ensuring the signature is unique.

The nuclear signature depends on the detector system and the warhead under inspection. As identified, "*to demonstrate the capabilities of a proposed system, a widely accepted reference item would be extremely helpful*" [213]. This thesis proposes eight such reference items, derived from an extensive review of available literature. These reference items could be used in future studies to test the capabilities of a proposed system.

Based on the notional warhead emission models, I analyzed the completeness and uniqueness of the nuclear signatures. To do so, it was necessary to develop new open-source capabilities:

- I implemented and validated a pulse-height tally functionality in OpenMC, which became an official part of the code.

- I developed a subcritical nuclide evolution tool capable of accurately modeling systems with non-negligible subcriticality, such as deployed nuclear warheads or warhead com-

ponents. This tool further determines an arbitrary material composition's photon and neutron emissions based on the ENSDF data.

Using extensive simulations, I find that most systems fail to correctly confirm two different-age-same-type warheads. Such incomplete nuclear signatures could lead to international tensions if inspectors mistakenly suspect a state of non-compliance. I further demonstrated that all analyzed systems have significant vulnerabilities to four different hoax objects, implying the non-uniqueness of the warhead emission signatures. The non-uniqueness of the signatures has significant implications for future verification regimes as they show that states could pretend to disarm nuclear weapons while presenting hoax objects to inspectors, while hiding their actual nuclear arsenal.

Sophisticated hoax objects — as the partial replacement of the fissile material with a californium-252 source — are not detectable by the confirmation systems. In this case measuring the passive neutron emissions in addition to the objects passive photon emissions will not lead to a better detection rate. To detect such hoax objects more intrusive measurements would be needed.

My results show that particularly low-resolution systems are vulnerable to cheating by hoaxes of a combination of radioactive nuclides. A simple increase in the measurement resolution (using more energy bins) would prevent these hoaxes. Still, it would also increase the risk of revealing sensitive information about the warhead and worsen the system's capability to confirm same-type-different-age warheads.

Finally, I explored how a genetic algorithm is capable of finding improved bin structures that overcome the analyzed vulnerabilities of nuclear signatures — allow for confirmation of same-type different-age objects in a template approach while at the same time being robust against hoaxes made from radioactive nuclides and assuring privacy as the host has full control over the disclosed information.

The results of this thesis provide insights into vulnerabilities and offer improvements on the signatures used for warhead confirmation. The framework developed here could be used to analyze additional confirmation systems, warhead models, and cheating scenarios. Due to its open-source nature, such analyzes transparent and accessible to researchers worldwide. Beyond additional models, it could be beneficial to study the effects of the environment in which the confirmation process takes place and manufacturing variations in the weapon itself. Future studies could also analyze neutron-multiplicity measurements as an additional passive neutron emission signature.

Focusing on verification technologies can reinforce the false narrative that technological barriers

hinder disarmament. In reality, there are no such barriers. If a state chooses to redefine its national security strategy — moving away from the belief that it must be prepared to inflict mass destruction for its protection — it can dismantle its nuclear weapons and publicly declare this action. The complete disarmament of South Africa, achieved through political decision-making and transparency, is a compelling example of this possibility.

This page intentionally blank

Bibliography

[1] **C. Fichtlscherer** et al. "Modeling gamma detectors in OpenMC: Validation of a newly implemented pulse-height tally". In: *Progress in Nuclear Energy* 172 (2024), p. 105186. DOI: 10.1016/j.pnucene.2024.105186.

[2] **C. Fichtlscherer**, M. Kütt. "Uniqueness, Reproducibility and Discrimination of Nuclear Warhead Gamma Signatures". In: *Science & Global Security* 32.1–3 (2024), pp. 5–41. DOI: 10.1080/08929882.2024.2387966.

[3] **C. Fichtlscherer**, M. Göttsche, M. Kütt. "Can We Fake Gamma Emissions of Nuclear Warheads? An Exploratory Study". In: *Institute of Nuclear Materials Management (INMM) and European Safeguards Research and Development Association (ESARDA) Joint Annual Meeting*. 2021. URL: https://resources.inmm.org/sites/default/files/2021-09/a337.pdf (visited on 02/25/2025).

[4] M. Kütt, J. Elfes, **C. Fichtlscherer**. "Fetter Model Revisited: Detecting Nuclear Weapons 30 Years Later". In: *Institute of Nuclear Materials Management (INMM) and European Safeguards Research and Development Association (ESARDA) Joint Annual Meeting*. 2021. URL: https://resources.inmm.org/sites/default/files/2021-09/a215.pdf (visited on 02/25/2025).

[5] **C. Fichtlscherer** et al. "Implementation and Validation of the Pulse-Height Tally in OpenMC". In: *Institute of Nuclear Materials Management (INMM) and European Safeguards Research and Development Association (ESARDA) Joint Annual Meeting*. 2021. URL: https://resources.inmm.org/sites/default/files/2021-09/a267.pdf (visited on 02/25/2025).

[6] M. Kütt, **C. Fichtlscherer**. "Hoax or Real? On the Uniqueness of Nuclear Radiation Signatures". In: *Alva Myrdal Centre for Nuclear Disarmament (AMC) Annual Conference*. 2022.

[7] **C. Fichtlscherer**, M. Kütt. "Improving Warhead Authentication using Gamma Spectroscopy". In: *65th Annual Meeting of the Institute of Nuclear Materials Management (INMM)*. 2024. URL: https://cdn.fourwaves.com/static/media/formdata/b12613f9-28b7-4568-a069-5c7cfeff3c8e/21b15233-1c7f-4a44-a2e5-bf980042b9e5.pdf (visited on 02/25/2025).

[8] **C. Fichtlscherer**, M. Kütt. "On the Uniqueness of Nuclear Warhead Signatures". In: *65th Annual Meeting of the Institute of Nuclear Materials Management (INMM)*. 2024. URL: https://cdn.fourwaves.com/static/media/formdata/b12613f9-28b7-4568-a069-5c7cfeff3c8e/ed30cb5f-3b30-4f83-a82c-d252987db431.pdf (visited on 02/25/2025).

[9] **C. Fichtlscherer** et al. "Modeling Spontaneous Fission-Driven Isotopic Change in Subcritical Nuclear Systems". In: *66th Annual Meeting of the Institute of Nuclear Materials Management (INMM) (Submitted)*. 2025.

[10] *Transparency and Verification Options: An Initial Analysis of Approaches for Monitoring Warhead Dismantlement*. U.S. Department of Energy (DOE), Office of Arms Control and Nonproliferation, 1997. URL: https://sgp.fas.org/othergov/doe/dis/transparency.pdf (visited on 02/25/2024).

[11] *Dismantlement of Nuclear Weapons by the Department of Energy*. U.S. Department of Energy (DOE), Sandia National Laboratories. n.d. URL: https://www.youtube.com/watch?v=SOajFJIzQew (visited on 12/20/2024).

[12] *Dismantling the Bomb and Managing the Nuclear Materials*. OTA-O-572. U.S. Congress, Office of Technology Assessment, 1993. URL: https://govinfo.library.unt.edu/ota/Ota_1/DATA/1993/9320.PDF (visited on 02/24/2024).

[13] *Pantex Plant Pit Inventory Review*. Staff Report. Defense Nuclear Facilities Safety Board, 2021. URL: https://www.dnfsb.gov/sites/default/files/document/25061/Pantex%20Pit%20Inventory%20[2022-100-011].pdf (visited on 02/24/2024).

[14] S. J. Paltrow. "America's nuclear headache: old plutonium with nowhere to go". In: *Reuters* (Apr. 23, 2018). URL: https://www.reuters.com/article/world/americas-nuclear-headache-old-plutonium-with-nowhere-to-go-idUSKBN1HR1JT/ (visited on 01/30/2025).

[15] M. Kütt, Z. Mian. "Setting the Deadline for Nuclear Weapon Destruction under the Treaty on the Prohibition of Nuclear Weapons". In: *Journal for Peace and Nuclear Disarmament* 2.2 (2019), pp. 410–430. DOI: 10.1080/25751654.2019.1674471.

[16] *The US Nuclear Weapons Complex: Major Facilities*. Union of Concerned Scientists, 2012. URL: https://www.ucsusa.org/resources/us-nuclear-weapons-complex (visited on 01/28/2025).

[17] *Transparency in the U.S. Nuclear Weapons Stockpile*. U.S. Department of Energy (DOE), National Nuclear Security Administration (NNSA), n.d. URL: https://www.energy.gov/nnsa/transparency-us-nuclear-weapons-stockpile (visited on 10/30/2024).

[18] M. Göttsche, J. Schirm, A. Glaser. "Low-resolution gamma-ray spectrometry for an information barrier based on a multi-criteria template-matching approach". In: *Nuclear Instruments and Methods in Physics Research Section A: Accelerators, Spectrometers, Detectors and Associated Equipment* 840 (2016), pp. 139–144. DOI: 10.1016/j.nima.2016.10.013.

[19] M. Kütt, M. Göttsche, A. Glaser. "Information barrier experimental: Toward a trusted and open-source computing platform for nuclear warhead verification". In: *Measurement* 114 (2018), pp. 185–190. DOI: 10.1016/j.measurement.2017.09.014.

[20] M. Kütt, A. Glaser. "Vintage electronics for trusted radiation measurements and verified dismantlement of nuclear weapons". In: *PLOS ONE* 14.10 (2019), e0224149. DOI: 10.1371/journal.pone.0224149.

[21] M. Hamel et al. "Third Generation Trusted Radiation Identification System (3G-TRIS)". In: *65th Annual Meeting of the Institute of Nuclear Materials Management (INMM)*. 2024.

[22] T. B. Cochran, S. Fetter. "Verifying the Authenticity of Nuclear Warheads Without Revealing Sensitive Design Information". In: *Proceedings of the Third International Workshop on Verified Storage and Destruction of Nuclear Warheads*. 1991. URL: https://fetter.it-prod-webhosting.aws.umd.edu/sites/default/files/fetter/files/1991-Cochran-Fingerprint.pdf (visited on 02/25/2025).

[23] *Phase I Summary Report: Creating the Verification Building Blocks for Future Nuclear Disarmament*. International Partnership for Nuclear Disarmament Verification (IPNDV), 2017. URL: https://www.ipndv.org/wp-content/uploads/2017/12/IPNDV-Phase-I-Summary-Report_Final.pdf (visited on 12/11/2023).

[24] J. Mattingly. *Polyethylene-Reflected Plutonium Metal Sphere: Subcritical Neutron and Gamma Measurements*. SAND2009-5804, Revision 1. U.S. Department of Energy (DOE), Sandia National Laboratories, 2009. DOI: 10.2172/974870. URL: http://www.osti.gov/servlets/purl/974870-qMgTgX/ (visited on 03/01/2024).

[25] S. Fetter et al. "Detecting nuclear warheads". In: *Science & Global Security* 1.3–4 (1990), pp. 225–253. DOI: 10.1080/08929889008426333.

[26] *Confidence, Security and Verification, The challenge of global nuclear weapons arms control*. AWE/TR/2000/001. U.K. Ministry of Defence, Atomic Weapons Establishment, 1998. URL: https://fissilematerials.org/library/awe00.pdf (visited on 02/14/2024).

[27] D. Cliff, H. Elbahtimy, A. Persbo. *Verifying Warhead Dismantlement, Past, Present, Future*. 9. Verification Research, Training and Information Centre (VERTIC), 2010. URL: https://www.files.ethz.ch/isn/132416/VM9.pdf (visited on 02/25/2024).

[28] J. Franck et al. *The "Franck Report", A Report to the Secretary of War, June 1945*. Atomic Heritage Foundation. 1945. URL: https://ahf.nuclearmuseum.org/ahf/key-documents/franck-report/ (visited on 02/14/2024).

[29] A. S. Krass. *Verification: How Much Is Enough?* Taylor & Francis, 1985.

[30] S. Plath. *The Bell Jar*. Heinemann, 1963.

[31] A. Schaper. *Looking for a Demarcation - between Nuclear Transparency and Nuclear Secrecy*. 68. Peace Research Institute Frankfurt (PRIF), 2004. URL: https://www.files.ethz.ch/isn/28862/prifrep68.pdf (visited on 02/25/2025).

[32] J. Russell. *On-Site Inspections Under the INF Treaty: A Post-Mortem*. Verification Research, Training and Information Centre (VERTIC) Briefing Paper, 2001. URL: https://www.vertic.org/media/Archived_Publications/Briefing_Papers/Briefing_Paper_01_2.pdf (visited on 02/25/2025).

[33] R. I. Ewing, K. W. Marlow. "A fast-neutron detector used in verification of the INF Treaty". In: *Nuclear Instruments and Methods in Physics Research Section A: Accelerators, Spectrometers, Detectors and Associated Equipment* 299.1–3 (1990), pp. 559–561. DOI: 10.1016/0168-9002(90)90843-U.

[34] *Radiation Detection Equipment, An Arms Control Verification Tool*. 211P. U.S. Department of Defense (DoD), Defense Threat Reduction Agency (DTRA), 2011.

[35] H. Müller, A. Schaper. *Nuclear Transparency and Registers of Nuclear Weapons and Fissile Materials*. 97. Peace Research Institute Frankfurt (PRIF), 2010. URL: https://www.prif.org/fileadmin/Daten/Publikationen/Prif_Reports/2010/prif97.pdf (visited on 02/26/2025).

[36] D. Kimball. *The START III Framework at a Glance*. Arms Control Association, n.d. URL: https://www.armscontrol.org/factsheets/start3 (visited on 05/17/2024).

[37] E. Immerman. "Direct Verification of Nuclear Weapons and the Secrecy-Certainty Spectrum". Massachusetts Institute of Technology, 2016. URL: https://dspace.mit.edu/bitstream/handle/1721.1/104829/959239642-MIT.pdf?sequence=1&isAllowed=y (visited on 02/20/2024).

[38] T. B. Taylor. "Verified Elimination of Nuclear Warheads". In: *Science & Global Security* 1.1–2 (1989), pp. 1–26. DOI: 10.1080/08929888908426321.

[39] S. Fetter et al. "Gamma-Ray Measurements of a Soviet Cruise-Missile Warhead". In: *Science* 248.4957 (1990), pp. 828–834. DOI: 10.1126/science.248.4957.828.

[40] R. R. Macdonald, R. S. Kemp. *Quantifying Privacy in Nuclear Warhead Authentication Protocols*. 2018. arXiv: 1811.10375. Pre-published.

[41] J. Yan, A. Glaser. "The Challenge of Nuclear Warhead Verification For Arms Control and Disarmament: A Review of Attribute and Template Systems". In: *Science & Global Security* 23.3 (2015), pp. 157–170. DOI: 10.1080/08929882.2015.1087221.

[42] *U.S. May Face Challenges in Verifying Future Treaty Goals (Accessible Version)*. GAO-23-105698. U.S. Government Accountability Office (GAO), 2023. URL: https://www.gao.gov/assets/870/861758.pdf (visited on 10/24/2024).

[43] S. Sonder et al. “Simulating the Passive Neutron and Gamma Signatures of Containerized Nuclear Warheads for Disarmament Verification”. In: *Science & Global Security* 31.1–2 (2023), pp. 16–40. DOI: 10.1080/08929882.2023.2223832.

[44] M. R. Smith. “Overview of Information Barrier Concepts”. International Partnership for Nuclear Disarmament Verification, Working Group 3. 2016. URL: https://www.ipndv.org/wp-content/uploads/2017/11/WG3-Overview-Info-Barrier_Smith-Sept-2016.pdf (visited on 02/25/2025).

[45] M. Kütt. “Arms-control lessons from the Volkswagen scandal”. In: *Bulletin of the Atomic Scientists* (2015). URL: https://thebulletin.org/2015/11/arms-control-lessons-from-the-volkswagen-scandal/ (visited on 05/21/2024).

[46] A. Wellerstein. “The Virtues of Nuclear Ignorance”. In: *The New Yorker* (2016).

[47] A. Glaser, B. Barak, R. J. Goldston. “A zero-knowledge protocol for nuclear warhead verification”. In: *Nature* 510.7506 (2014), pp. 497–502. DOI: 10.1038/nature13457.

[48] R. S. Kemp et al. “Physical cryptographic verification of nuclear warheads”. In: *Proceedings of the National Academy of Sciences (PNAS)* 113.31 (2016), pp. 8618–8623. DOI: 10.1073/pnas.1603916113.

[49] P. Marleau et al. “Zero Knowledge Protocol: Challenges and Opportunities”. In: *60th Annual Meeting of the Institute of Nuclear Materials Management (INMM)*. 2015.

[50] J. J. Hecla, A. Danagoulian. “Nuclear disarmament verification via resonant phenomena”. In: *Nature Communications* 9.1 (2018), p. 1259. DOI: 10.1038/s41467-018-03680-4.

[51] *Field Test FT-34 Demonstraed Destruction of Nuclear Weapons, Final Report - Volume 1, Annex D*. SAB20000124A001. U.S. Arms Control and Disarmament Agency (ACAD), 1969. URL: https://nuke.fas.org/guide/usa/cloudgap/ft-34v3-annexd.pdf (visited on 03/04/2025).

[52] F. Von Hippel. “The 1969 ACDA study on warhead dismantlement”. In: *Science & Global Security* 2.1 (1990), pp. 103–108. DOI: 10.1080/08929889008426351.

[53] *Historique de l’armement nucléaire du Mirage IV A Premiere Traversee Oceanique Effectue Par Un Avion De Combat a Reaction Français*. Association Nationale des Forces Aériennes Stratégiques (ANFAS). n.d. URL: http://anfas.free.fr/anm/historique_anm.html (visited on 05/16/2024).

[54] *Espionage and the Manhattan Project (1940-1945)*. U.S. Department of Energy (DOE), Office of History and Heritage Resources. n.d. URL: https://www.osti.gov/opennet/manhattan-project-history/Events/1942-1945/espionage.htm (visited on 11/13/2024).

[55] S. Leskov. “Dividing the Glory of the Fathers”. In: *Bulletin of the Atomic Scientists* 49.4 (May 1993), pp. 37–39. DOI: 10.1080/00963402.1993.11456343.

[56] *Voices of the Manhattan Project, J. Carson Mark's Interview*. The National Museum of Nuclear Science & History. 1983. URL: https://ahf.nuclearmuseum.org/voices/oral-histories/j-carson-marks-interview/ (visited on 09/03/2024).

[57] C. McGreal. "Revealed: how Israel offered to sell South Africa nuclear weapons". In: *The Guardian. World news* (May 24, 2010). ISSN: 0261-3077. URL: https://www.theguardian.com/world/2010/may/23/israel-south-africa-nuclear-weapons (visited on 08/20/2024).

[58] C. Sublette. *The Nuclear Weapon Archive, A Guide to Nuclear Weapons*. n.d. URL: https://nuclearweaponarchive.org/ (visited on 03/04/2025).

[59] M. A. Kilpatrick. *Declassification Determination*. U.S. Department of Energy (DOE), Aug. 16, 2006. URL: https://sgp.fas.org/othergov/doe/decl/w88-prc.pdf (visited on 03/03/2025).

[60] D. Samuels. "Atomic John." In: *The New Yorker* (Dec. 7, 2008). URL: https://www.newyorker.com/magazine/2008/12/15/atomic-john (visited on 03/12/2024).

[61] M. Hamel. "Next-Generation Arms-Control Agreements based on Emerging Radiation Detection Technologies". In: *59th Annual Meeting of the Institute of Nuclear Materials Management (INMM)*. 2018. URL: https://www.osti.gov/servlets/purl/1526354 (visited on 03/04/2025).

[62] *Strategic Offensive Reductions Treaty (SORT)*. Nuclear Threat Initiative (NTI). n.d. URL: https://www.nti.org/education-center/treaties-and-regimes/strategic-offensive-reductions-treaty-sort/ (visited on 12/09/2024).

[63] H. S. Lew, M. Stranahan. "Decoy Deploying ICBM Warhead". U.S. pat. 4829905A. 1989. URL: https://patentimages.storage.googleapis.com/b7/ea/3d/f5280f3dae517c/US4829905.pdf (visited on 03/04/2025).

[64] *Ballistic and Cruise Missile Threat*. NASIC-1031-0985-17. Defense Intelligence Ballistic Missile Analysis Committee, 2017. URL: https://www.nasic.af.mil/Portals/19/images/Fact%20Sheet%20Images/2017%20Ballistic%20and%20Cruise%20Missile%20Threat_Final_small.pdf (visited on 11/13/2024).

[65] N. Zarimpas, ed. *Transparency in Nuclear Warheads and Materials The Political and Technical Dimensions*. Oxford University Press, 2003.

[66] R. C. Connick. "Assessing differential scanning calorimetry as a retrospective dosimetry method for the verification of uranium enrichment activities". Massachusetts Institute of Technology, 2022. URL: https://dspace.mit.edu/handle/1721.1/144794 (visited on 03/04/2025).

[67] K. Bethge, G. Walter, B. Wiedemann. *Kernphysik*. 3rd ed. Springer, 2008.

[68] T. Mayer-Kuckuk. *Kernphysik*. 7th ed. Teubner. Wiesbaden: Teubner, 2002.

[69] J. M. Blatt, V. F. Weisskopf. *Theoretical Nuclear Physics*. 1st ed. Springer, 1979.

[70] W. Demtröder. *Experimentalphysik 4, Kern-, Teilchen- und Astrophysik*. 5. Aufl. Springer, 2017.

[71] *Nuclear Wallet Cards Search*. National Nuclear Data Center (NNDC). n.d. URL: https://www.nndc.bnl.gov/walletcards/search.html (visited on 11/26/2024).

[72] *DOE Explains...Isotopes*. U.S. Department of Energy (DOE), Office of Science. n.d. URL: https://www.energy.gov/science/doe-explainsisotopes (visited on 02/14/2024).

[73] *Evaluated Nuclear Structure Data File (ENSDF)*. National Nuclear Data Center (NNDC). URL: https://www.nndc.bnl.gov/ensdfarchivals/ (visited on 01/30/2024).

[74] H. J. Rose, G. A. Jones. "A new kind of natural radioactivity". In: *Nature* 307.5948 (1984), pp. 245–247. DOI: 10.1038/307245a0.

[75] N. Bohr, J. A. Wheeler. "The Mechanism of Nuclear Fission". In: *Physical Review* 56.5 (1939), pp. 426–450. DOI: 10.1103/PhysRev.56.426.

[76] G. N. Flerov, K. A. Petrjak. "Spontaneous Fission of Uranium". In: *Physical Review* 58.1 (1940), pp. 89–89. DOI: 10.1103/PhysRev.58.89.2.

[77] L. Qi et al. "An improved Gamow-like formula for cluster radioactivity". In: *Nuclear Physics A* 1050 (Oct. 2024), p. 122929. DOI: 10.1016/j.nuclphysa.2024.122929.

[78] J. M. Verbeke, C. Hagmann, D. Wright. *Simulation of Neutron and Gamma Ray Emission from Fission and Photofission. LLNL Fission Library 2.0.2.* UCRL-AR-228518-REV-1. Lawrence Livermore National Laboratory, 2016. URL: https://nuclear.llnl.gov/simulation/fission.pdf (visited on 05/03/2024).

[79] N. Ensslin et al. *Application Guide to Neutron Multiplicity Counting*. LA-13422-M. Los Alamos National Laboratory, 1998. URL: https://cdn.lanl.gov/files/m-app-to-neutron-multiplicity-counting_9ea55.pdf (visited on 03/03/2025).

[80] M. R. Snowden. "Nuclear Warhead Monitoring a Study of Photon Emissions from Fission Neutron Interactions with High Explosives as a Tool in Arms Control Verification". Massachusetts Institute of Technology, 2017. URL: https://dspace.mit.edu/handle/1721.1/113723 (visited on 03/03/2025).

[81] H. Meng et al. "A Passive Method for the Detection of Explosives and Weapons-Grade Plutonium in Nuclear Warheads". In: *Science & Global Security* 26.2–3 (Sept. 2, 2018), pp. 57–69. DOI: 10.1080/08929882.2018.1517431.

[82] L. Dommelen. *Quantum Mechanics for Engineers*. 5.55 alpha. 2012. URL: https://websites.umich.edu/~ners312/CourseLibrary/Dommelen.pdf (visited on 03/04/2025).

[83] G. F. Knoll. *Radiation Detection and Measurement*. 3rd ed. John Wiley & Sons, 2000.

[84] *How Do Sodium Iodide (Scintillation) Detectors Work?* Nevada Technical Associates, Inc. 2015. URL: https://www.ntanet.net/how-do-sodium-iodide-scintillation-detectors-work (visited on 01/13/2025).

[85] K. D. Seager et al. "Trusted Radiation Identification System". In: *43th Annual Meeting of the Institute of Nuclear Materials Management (INMM)*. 2001. URL: https://media.nti.org/pdfs/SNL-12_SAND2001-1866C.pdf (visited on 03/04/2025).

[86] M. Hamel. *The Trusted Radiation Identification System (TRIS): Designed to Encourage Trust*. SAND2019-2623C. Institute of Nuclear Materials Management (INMM), Just Trust Me Workshop. Sandia National Laboratories, 2019. URL: https://www.osti.gov/servlets/purl/1639365 (visited on 03/04/2025).

[87] K. Allen et al. *Selection and Deployment of Verification Technologies, Lessons learned from the Quad Nuclear Verification Partnership and the LETTERPRESS Simulation*. 2019. URL: https://quad-nvp.info/wp-content/uploads/2020/06/QUAD-Selection-and-deployment-of-verification-technologies_-March-2019.pdf (visited on 02/20/2022).

[88] P. B. Merkle et al. "Next Generation Trusted Radiation Identification System". In: *51th Annual Meeting of the Institute of Nuclear Materials Management (INMM)*. 2010. URL: https://media.nti.org/pdfs/SNL-1_FINAL_INMM_2010_Next_Generation_Trusted_Radiation_System.pdf (visited on 03/04/2025).

[89] M. Kütt, A. Glaser. *IBX II Software & Hardware*. 2019. URL: https://github.com/sgs-lab/ibxII (visited on 01/15/2025).

[90] *Trusted Radition Identification System (TRIS), 3G TRIS*. SAND2023-10878PE. Sandia National Laboratories, n.d. URL: https://www.sandia.gov/app/uploads/sites/239/2023/05/3G_TRIS_SAND2023-10878PE.pdf (visited on 07/04/2024).

[91] P. K. Romano et al. "OpenMC: A state-of-the-art Monte Carlo code for research and development". In: *Annals of Nuclear Energy* 82 (2015), pp. 90–97. DOI: 10.1016/j.anucene.2014.07.048.

[92] A. Sood et al. "Neutronics Calculation Advances at Los Alamos: Manhattan Project to Monte Carlo". In: *Nuclear Technology* 207 (sup1 2021), S100–S133. DOI: 10.1080/00295450.2021.1956255.

[93] T. E. Booth. "Common misconceptions in Monte Carlo particle transport". In: *Applied Radiation and Isotopes* 70.7 (2012), pp. 1042–1051. DOI: 10.1016/j.apradiso.2011.11.037.

[94] *OpenMC: Random Number Generation*. URL: https://docs.openmc.org/en/stable/methods/random_numbers.html (visited on 02/04/2025).

[95] N. Metropolis. "The Beginning of the Monte Carlo Method". In: *Los Alamos Science* 15 (1987), pp. 125–130. URL: https://library.lanl.gov/cgi-bin/getfile?00326866.pdf (visited on 03/15/2019).

[96] T. E. Hull, A. R. Dobell. "Random Number Generators". In: *SIAM Review* 4.3 (1962), pp. 230–254. DOI: 10.1137/1004061. URL: http://epubs.siam.org/doi/10.1137/1004061.

[97] C. Werner et al. *MCNP Version 6.2 Release Notes*. LA-UR–18-20808. Los Alamos National Laboratory, 2018. DOI: 10.2172/1419730. URL: https://www.osti.gov/servlets/purl/1419730/ (visited on 07/06/2024).

[98] *Geant, Detector Description and Simulation Tool*. CERN, 1994. URL: https://cds.cern.ch/record/1073159/files/cer-002728534.pdf (visited on 07/06/2024).

[99] D. E. G. Barroso. "Equation of State of Uranium and Plutonium, v4". In: *arXiv* (2015). DOI: 10.48550/arXiv.1502.00497.

[100] T. R. England. *Cinder - a One-Point Depletion and Fission Product Program*. WAPT-TM-334. Bettis Atomic Power Laboratory Pittsburgh, 1962. URL: https://www.osti.gov/servlets/purl/4765256 (visited on 11/26/2024).

[101] M. J. Bell. *Origen - The ORNL Isotope Generation and Depletion Code*. ORNL-4628. Oak Ridge National Laboratory, 1973. URL: https://www.osti.gov/servlets/purl/4480214 (visited on 11/25/2024).

[102] J. Troullioud de Lanversin, M. Kütt, A. Glaser. "ONIX: An open-source depletion code". In: *Annals of Nuclear Energy* 151 (2021), p. 107903. DOI: 10.1016/j.anucene.2020.107903.

[103] P. K. Romano et al. "Depletion capabilities in the OpenMC Monte Carlo particle transport code". In: *Annals of Nuclear Energy* 152 (2021), p. 107989. DOI: 10.1016/j.anucene.2020.107989.

[104] S. Agostinelli et al. "Geant4—a simulation toolkit". In: *Nuclear Instruments and Methods in Physics Research Section A* 506.3 (2003), pp. 250–303. DOI: 10.1016/S0168-9002(03)01368-8.

[105] M. Kreutle et al. "Validating Geant4 with Monte Carlo simulations in the context of nuclear disarmament verification". In: *Nuclear Instruments and Methods in Physics Research Section A* 1057 (2023), p. 168774. DOI: 10.1016/j.nima.2023.168774.

[106] S. Zhang et al. *Evaluation of Applicability of Geant4 and Openmc in Tritium Breeding Calculation for Fusion Blanket*. 2024. DOI: 10.2139/ssrn.4954474. Pre-published.

[107] G. Varignier et al. "Comparison between GEANT4 and MCNP for well logging applications". In: *EPJ Web of Conferences* 288 (2023), p. 01002. DOI: 10.1051/epjconf/202328801002.

[108] M. Kütt, M. Gottsche. "Neutron Multiplicity Simulations: Geant4 versus MCNPX-PoliMi". In: *57th Annual Meeting of the Institute of Nuclear Materials Management (INMM)*. 2016. URL: https://d-nb.info/1240614934/34 (visited on 03/03/2025).

[109] D. E. Cullen et al. *Static and Dynamic Criticality: Are They Different?* UCRL-TR-201506. Lawrence Livermore National Laboratory, 2003. URL: https://www.osti.gov/servlets/purl/15009756/ (visited on 10/11/2024).

[110] J. Tuli. *Evaluated nuclear structure data file*. BNL-NCS-51655-01/02-Rev. National Nuclear Data Center, Brookhaven National Laboratory, 2001. URL: https://linkinghub.elsevier.com/retrieve/pii/S0168900296800404 (visited on 11/26/2024).

[111] J. K. Tuli. *Evaluated Nuclear Structure Data File and Related Products*. BNL-73538-2005-CP. National Nuclear Data Center, Brookhaven National Laboratory, 2005. URL: https://pubs.aip.org/aip/acp/article/769/1/265-267/665996 (visited on 11/26/2024).

[112] O. Schwerer, P. Obloinský. "Overview of nuclear data libraries and online services". In: *Radiochimica Acta* 89.4–5 (2001), pp. 197–202. DOI: 10.1524/ract.2001.89.4-5.197.

[113] Nuclear Energy Agency (NEA). *Specifications for the Generalised Nuclear Database Structure (GNDS), Version 2.0*. No. 7647. OECD, 2023.

[114] *NNDC Databases, Nuclear Structure and Decay Databases*. National Nuclear Data Center (NNDC). n.d. URL: https://www.nndc.bnl.gov/databases/ (visited on 11/26/2024).

[115] *Experimental Unevaluated Nuclear Data List, XUNDL*. National Nuclear Data Center (NNDC). n.d. URL: https://www.nndc.bnl.gov/ensdf/xundl/index.jsp (visited on 11/26/2024).

[116] *ENDF/B-VIII.0*. National Nuclear Data Center (NNDC). n.d. URL: https://www.nndc.bnl.gov/endf-b8.0/download.html (visited on 11/26/2024).

[117] E. Levy. "A matrix exponential approach to radioactive decay equations". In: *American Journal of Physics* 86.12 (2018), pp. 909–913. DOI: 10.1119/1.5064446.

[118] M. Pusa. "Higher-Order Chebyshev Rational Approximation Method and Application to Burnup Equations". In: *Nuclear Science and Engineering* 182.3 (2016), pp. 297–318. DOI: 10.13182/NSE15-26.

[119] M. Enghauser. *Uranium gamma spectroscopy training, Revision 00*. SAND2018-3370PE. Sandia National Laboratories, 2018. URL: https://www.osti.gov/biblio/1525592 (visited on 03/03/2025).

[120] M. Enghauser. *Independent Gamma Spectroscopy Analysis of a Plutonium Oxide Sample*. SAND2021-10372R. Sandia National Laboratories, 2021. DOI: 10.2172/1815344. URL: https://www.osti.gov/servlets/purl/1815344/ (visited on 05/09/2023).

[121] **C. Fichtlscherer**. *Pull request #1881, Pulse height tally*. Sept. 17, 2021. URL: https://github.com/openmc-dev/openmc/pull/1881 (visited on 01/07/2025).

[122] S. Horne et al. *GADRAS-DRF 18.6 User's Manual*. SAND2016-4345. Sandia National Laboratories, 2016. URL: https://www.osti.gov/servlets/purl/1431293/ (visited on 08/07/2024).

[123] T. Böhlen et al. "The FLUKA Code: Developments and Challenges for High Energy and Medical Applications". In: *Nuclear Data Sheets* 120 (2014), pp. 211–214. DOI: 10.1016/j.nds.2014.07.049.

[124] A. Ferrari et al. *FLUKA: A multi-particle transport code*. CERN-2005-10. Cern, 2005. URL: https://slac.stanford.edu/pubs/slacreports/reports16/slac-r-773.pdf (visited on 03/03/2025).

[125] I. Kawrakow et al. *EGSnrc toolkit for Monte Carlo simulation of ionizing radiation transport*. 2000. URL: https://github.com/nrc-cnrc/EGSnrc.

[126] *The EGS5 Code System*. SLAC-R-730. U.S. Department of Energy (DOE), 2005. URL: https://www.slac.stanford.edu/pubs/slacreports/reports16/slac-r-730.pdf (visited on 01/07/2025).

[127] F. Salvat, J. M. Fernández-Varea, J. Sempau. *PENELOPE-2014: A Code System for Monte Carlo Simulation of Electron and Photon Transport. Issy-les-Moulineaux*. NEA/NSC/DOC(2015)3. Nuclear Energy Agency (NEA), 2011. URL: https://www.oecd-nea.org/upload/docs/application/pdf/2020-01/nsc-doc2015-3.pdf (visited on 03/03/2025).

[128] V. Scot, J. E. Fernandez. "The Monte Carlo code MCSHAPE: Main features and recent developments". In: *Spectrochimica Acta Part B* 108 (2015), pp. 53–60. DOI: 10.1016/j.sab.2015.02.005.

[129] K. Saito, S. Moriuchi. "Monte Carlo calculation of accurate response functions for a NaI(Tl) detector for gamma rays". In: *Nuclear Instruments and Methods in Physics Research* 185.1–3 (1981), pp. 299–308. DOI: 10.1016/0029-554X(81)91225-8.

[130] S. S. Nayak, G. Mukherjee. "SIMSPEC-G: a simple code for the simulation of HPGe detectors for gamma rays up to 1 MeV". In: *Journal of Instrumentation* 17.07 (2022), P07030. DOI: 10.1088/1748-0221/17/07/P07030.

[131] M. Drissi El-Bouzaidi et al. "Simulation of a NaI(Tl) detector model using OpenMC modified on code source and validation using experimental and simulated results". In: *Radiation Physics and Chemistry* 206 (2023), p. 110777. DOI: 10.1016/j.radphyschem.2023.110777.

[132] L. Boltzmann. "Weitere Studien über das Wärmegleichgewicht unter Gasmolekülen". In: *Kinetische Theorie II: Irreversible Prozesse* 166 (1872). DOI: 10.1515/9783112596760-011.

[133] T. E. Booth. "A Monte Carlo Variance Reduction Approach for Non-Boltzmann Tallies". In: *Nuclear Science and Engineering* 116.2 (1994), pp. 113–124. DOI: 10.13182/NSE94-A21487.

[134] A. L. Lund, P. K. Romano. *Implementation and Validation of Photon Transport in OpenMC*. ANL/MCS-TM-381. Argonne National Laboratory, 2018. URL: http://www.osti.gov/servlets/purl/1490825/ (visited on 11/01/2021).

[135] D. Cullen, J. H. Hubbell, L. Kissel. *EPDL97: The Evaluated Photon Data Library '97 Version*. UCRL-LR-50400 Vol 6 Rev 5. Lawrence Livermore National Laboratory, 1997. URL: https://www.osti.gov/servlets/purl/295438 (visited on 12/07/2024).

[136] M. Miah. "Analytical Validation of the Pulse Height Tally". RWTH Aachen, 2022. URL: https://www.nvd.rwth-aachen.de/global/show_document.asp?id=aaaaaaaabkgyonx (visited on 03/03/2025).

[137] T. Shuttleworth. "The Verification of Monte Carlo Codes in Middle Earth". In: *Proceedings of 8th International Conference on Radiation Shielding*. 1994, p. 1148.

[138] A. Sood et al. "Verification of the pulse height tally in MCNP 5". In: *Nuclear Instruments and Methods in Physics Research Section B* 213 (2004), pp. 167–171. DOI: 10.1016/S0168-583X(03)01598-2.

[139] A. Sood, M. S. Reed, R. A. Forster. *New Results for Pulse Height Tally Verification in MCNP5*. LA-UR-03-4271. Los Alamos National Laboratory, 2003. URL: https://mcnp.lanl.gov/pdf_files/TechReport_2003_LANL_LA-UR-03-4271_SoodReedEtAl.pdf (visited on 12/07/2024).

[140] *802 Scintillation Detectors*. Mirion Technologies, 2017. URL: https://mirionprodstorage.blob.core.windows.net/prod-20220822/cms4_mirion/files/pdf/spec-sheets/csp0232_802_super_spec_2.pdf (visited on 01/25/2024).

[141] C. J. Tichacek et al. "A Monte Carlo Method for Determining the Response Relationship between Two Commonly Used Detectors to Indirectly Measure Alpha Particle Radiation Activity". In: *Molecules* 24.18 (2019), p. 3397. DOI: 10.3390/molecules24183397.

[142] M. C. Han et al. "First Assessment of ENDF/B-VIII and EPICS Atomic Data Libraries". In: *IEEE Transactions on Nuclear Science* 65.8 (2018), pp. 2268–2278. DOI: 10.1109/TNS.2018.2849328.

[143] P. Romano. *LANL-Based Data Libraries*. n.d. URL: https://openmc.org/lanl-data-libraries/ (visited on 01/08/2025).

[144] F. J. Massey Jr. "The Kolmogorov-Smirnov Test for Goodness of Fit". In: *Journal of the American Statistical Association* 46.253 (1951), pp. 68–78. DOI: 10.2307/2280095.

[145] R. L. Heath. *Scintilation Spectrometry Gamma-Ray Spectrum Catalogue*. U.S. Atomic Energy Commission, 1964. URL: https://www.osti.gov/servlets/purl/4033555 (visited on 03/24/2024).

[146] N. Karmalitsyn et al. "Standardization of 65Zn". In: *Applied Radiation and Isotopes* 60.2–4 (2004), pp. 391–395. DOI: 10.1016/j.apradiso.2003.11.047.

[147] L. Li, Q. Alexander, B. Ende. "A Method for Coincidence Summing Compensation of Simulation Results Using MCNP on Co60 Volume Source". In: *CNL Nuclear Review* (2016), pp. 1–5. DOI: 10.12943/CNR.2015.00053.

[148] G. T. Emery. "Perturbation of Nuclear Decay Rates". In: *Annual Review of Nuclear Science* 22.1 (1972), pp. 165–202. DOI: 10.1146/annurev.ns.22.120172.001121.

[149] S. Sonder, C. Prünte, G. Kirchner. "Neutron Signature of a Two-Stage Nuclear Warhead before Dismantlement". In: *Alva Myrdal Centre's annual conference*. 2022.

[150] J. W. Toevs, C. A. Beard. *Gallium in Weapons-Grade Plutonium and MOX Fuel Fabrication*. LA-UR-96-4764. Los Alamos National Laboratory, 1996. URL: https://www.ieer.org/latest/gallium.html (visited on 03/03/2025).

[151] J. Coster-Mullen. *Atom Bombs, The Top Secret Inside Story of Little Boy and Fat Man*. Self-Published, 2020.

[152] S. Hecker. *Challenges in Plutonium Science*. LA-UR-00-4100. Los Alamos National Laboratory, 2000.

[153] L. Hoddeson et al. *Critical Assembly: A Technical History of Los Alamos during the Oppenheimer Years, 1943–1945*. 1st ed. Cambridge University Press, 1993.

[154] F. Weigel. *Plutonium handbook – A guide to the technology*. 1st ed. American Nuclear Society, 1980.

[155] *Materials: Plutonium*. International Panel on Fissile Materials. 2024. URL: https://fissilematerials.org/materials/plutonium.html (visited on 09/02/2024).

[156] *Reactor-Grade and Weapons-Grade Plutonium in Nuclear Explosives*. Canadian Coalition for Nuclear Responsibility. n.d. URL: http://www.ccnr.org/plute.html (visited on 09/02/2024).

[157] J. C. Mark, F. Von Hippel, E. Lyman. "Explosive Properties of Reactor-Grade Plutonium". In: *Science & Global Security* 17.2–3 (2009), pp. 170–185. DOI: 10.1080/08929880903368690.

[158] *IAEA safeguards glossary*. International Atomic Energy Agency, 2022.

[159] *Compendium of Material Composition Data for Radiation Transport Modeling*. 200-DMAMC-128170, PNNL-15870, Rev. 2. U.S. Department of Homeland Security, Pacific Northwest National Laboratory, 2021. URL: https://www.osti.gov/servlets/purl/1782721 (visited on 03/03/2025).

[160] B. Maiorov et al. “Elastic moduli of delta-Pu239 reveal aging in real time”. In: *Journal of Applied Physics* 121.12 (2017), p. 125107. DOI: 10.1063/1.4978509.

[161] D. E. Cullen. *Defintion of K-eff*. 2009. URL: http://redcullen1.net/homepage.new/Papers/K-eff/K-eff.pdf (visited on 03/03/2025).

[162] E. U. Condon, R. Serber. *Los Alamos Primer*. University of California, 1992.

[163] *Manhattan District History, Project Y, The Los Alamos Project*. LAMS-2532. United States of America War Department, Los Alamos Laboratories, 1961. URL: https://www.osti.gov/biblio/1087644 (visited on 03/03/2025).

[164] *Pit production explained*. Los Alamos National Laboratory. 2021. URL: https://discover.lanl.gov/publications/national-security-science/2021-winter/pit-production-explained/ (visited on 09/09/2024).

[165] *Neutron Generator Enterprise at Sandia National Laboratories (U)*. SAND2015-10850PE. Sandia National Laboratories, 2015. URL: https://www.osti.gov/servlets/purl/1339208 (visited on 10/30/2024).

[166] *Why No One Will Ever Build Another Nagasaki Type Bomb*. Arms Control Wonk. 2014. URL: https://www.armscontrolwonk.com/archive/604623/why-no-one-will-ever-build-another-nagasaki-type-bomb/ (visited on 09/06/2024).

[167] T. A. Tomberlin. “Beryllium – A Unique Material In Nuclear Applications”. In: *36th International SAMPE Technical Conference*. 2004. URL: https://inldigitallibrary.inl.gov/sites/sti/sti/2808485.pdf (visited on 03/03/2025).

[168] A. P. Weston-Dawkes. *Declassification Determination*. U.S. Department of Energy (DOE), Mar. 8, 2010. URL: https://sgp.fas.org/othergov/doe/decl/beryl.pdf (visited on 09/03/2024).

[169] L. Arnold. *Britain and the H-Bomb*. U.K. Ministry of Defence (MOD), 2001.

[170] J. L. Sapir, R. Kidman, R. W. Brewer. *235U(94%) Spheres Surrounded by Natural-Uranium Reflectors*. LA-UR-98-1664. Los Alamos National Laboratory, n.d. URL: https://sgp.fas.org/othergov/doe/lanl/lib-www/la-pubs/00418688.pdf (visited on 03/03/2025).

[171] A. Gsponer, J. P. Hurni. *The physical principles of thermonuclear explosives, inertial confinement fusion, and the quest for fourth generation nuclear weapons, 7th ed.* Independent Scientific Research Institute, 2009. URL: https://cryptome.org/2014/06/wmd-4th-gen-quest.pdf (visited on 03/03/2025).

[172] T. M. Semkow, P. P. Parekh, D. K. Haines. “Modeling the Effects of the Trinity Test”. In: *American Chemical Society (ACS) series* (2006). DOI: 10.1021/bk-2007-0945.ch011.

[173] *Technological Issues Related to the Proliferation of Nuclear Weapons*. Nonproliferation Policy Education Center (NPEC). 1998. URL: https://npolicy.org/technological-issues-related-to-the-proliferation-of-nuclear-weapons/ (visited on 08/27/2024).

[174] J. A. McPhee. *The Curve of Binding Energy: A Journey Into the Awesome and Alarming World of Theodore B. Taylor*. 1st ed. Farrar, Straus and Giroux, 1974.

[175] *Restricted Data Declassification Decisions 1946 to the Present (RDD-7)*. U.S. Department of Energy (DOE). 2001. URL: https://sgp.fas.org/othergov/doe/rdd-7.html (visited on 02/13/2023).

[176] *Атомный проект СССР II: Атомная бомба 1945–1954*. Наука. Физматлит, 2006.

[177] P. A. Goetz. *A Technical History of America's Nuclear Weapons, Their Design, Operation, Delivery, and Deployment*. 2nd ed. Self-Published, 2018.

[178] "The B61 family of bombs". In: *Bulletin of the Atomic Scientists, Nuclear Notebook* 59.1 (2003), pp. 74–76. DOI: 10.1080/00963402.2003.11460650.

[179] S. J. Voelkel et al. "Effect of lot microstructure variations on detonation performance of the triaminotrinitrobenzene (TATB)-Based insensitive high explosive PBX 9502". In: *Combustion and Flame* 246 (2022), p. 112373. DOI: 10.1016/j.combustflame.2022.112373.

[180] B. T. Godwin. *Nuclear Weapons Technology 101 For Policy Wonks*. LLNL-MI-823628. Center for Global Security Research, Lawrence Livermore National Laboratory, 2021. URL: https://cgsr.llnl.gov/content/assets/docs/CGSR_NW101_Policy_Wonks_11-04-21_WEB_v5.pdf (visited on 02/07/2023).

[181] T. B. Cochran. *Hydronuclear Testing or a Comprehensive Test Ban? Draft*. Natural Resources Defense Council, Inc., 1994. URL: https://nuke.fas.org/cochran/nuc_04109401a_122.pdf (visited on 03/03/2025).

[182] D. MacKenzie, G. Spinardi. "Tacit Knowledge, Weapons Design, and the Uninvention of Nuclear Weapons". In: *American Journal of Sociology* 101.1 (1995), pp. 44–99. DOI: 10.1086/230699.

[183] J. Goldblat and D. Cox, eds. *Nuclear Weapon Tests: Prohibition or Limitation?* Oxford University Press, 1993.

[184] T. Johnston. *Database of nuclear tests, United States: part 1, 1945-1963*. 2006. URL: https://www.johnstonsarchive.net/nuclear/tests/USA-ntests1.html (visited on 09/06/2024).

[185] R. S. Norris et al. *Nuclear Weapons Databook 5: British, French and Chinese Nuclear Weapons*. Westview Press, 1994.

[186] G. A. Goncharov. "Thermonuclear Milestones: (1) The American Effort". In: *Physics Today* 49.11 (1996), pp. 45–48. DOI: 10.1063/1.2807828.

[187] E. Teller, S. N. Ulam. *On Heterocatalytic Detonations I. Hydrodynamic Lenses and Radiation Mirrors*. SAA200131150000. Los Alamos National Laboratory, 1951. URL: https://nsarchive2.gwu.edu/nukevault/ebb507/docs/doc%204%20%2051.03.09%20LAMS-1225.pdf (visited on 09/03/2024).

[188] R. Rhodes. *Dark Sun, The Making of the Hydrogen Bomb*. Touchstone, 1995.

[189] *Castle Bravo*. The National Museum of Nuclear Science & History. 2017. URL: https://ahf.nuclearmuseum.org/ahf/history/castle-bravo/ (visited on 09/05/2024).

[190] A. George. "Pulsierendes Deuterium-Lithium Kernkraftwerk II". Pat. DT2401488A1 (German Patent). 1975. URL: https://patents.google.com/patent/DE2400274A1/de (visited on 03/03/2025).

[191] D. Kramer. "DOE prepares major upgrade of its lithium-6 operations". In: *Physics Today* 71.5 (2018), pp. 29–31. DOI: 10.1063/PT.3.3919.

[192] D. Holloway. *Stalin and the Bomb, The Soviet Union and Atomic Energy, 1939-1956*. Yale University Press, 1994.

[193] *Justification for Restricted Data or Formerly Restricted Data Classification or Declassification Decisions*. U.S. Department of Energy (DOE), 2003. URL: https://sgp.fas.org/othergov/doe/decl/rd-2002.pdf (visited on 03/03/2025).

[194] A. Pritzker, W. Hälg. "Radiation dynamics of a nuclear explosion". In: *ZAMP Zeitschrift für angewandte Mathematik und Physik* 32.1 (1981), pp. 1–11. DOI: 10.1007/BF00953545.

[195] "The H-bomb secret, How we got it - why we're telling it". In: *The Progressive* (1979). URL: https://biotech.law.lsu.edu/blog/1179.pdf (visited on 09/03/2024).

[196] *Minuteman III*. Center for Strategic and International Studies (CSIS) Missile Defense Project. 2024. URL: https://missilethreat.csis.org/missile/minuteman-iii/ (visited on 09/06/2024).

[197] J. N. Gibson. *Nuclear Weapons of the United States: An Illustrated History*. Schiffer military history. Schiffer Military History, 1996.

[198] *LGM-30G Minuteman III*. Air Force. n.d. URL: https://www.af.mil/About-Us/Fact-Sheets/Display/Article/104466/lgm-30g-minuteman-iii/https%3A%2F%2Fwww.af.mil%2FAbout-Us%2FFact-Sheets%2FDisplay%2FArticle%2F104466%2Flgm-30g-minuteman-iii%2F (visited on 09/06/2024).

[199] D. K. Stumpf. "Reentry Vehicle Development Leading to the Minuteman Avco Mark 5 and 11". In: *Air Power History* (2017). JSTOR: 26571038. URL: https://www.jstor.org/stable/26571038?seq=8 (visited on 03/03/2025).

[200] W. Garcia et al. *Composite Material Application to the MK12A RV Midbay Substructure.:* CASD/ASC-76-001A. Army Materials and Mechanics Research Center, 1979. DOI: 10.21236/ADA076485. URL: http://www.dtic.mil/docs/citations/ADA076485 (visited on 02/05/2023).

[201] L. Gronlund, D. C. Wright. "Depressed trajectory SLBMS: A technical evaluation and arms control possibilities". In: *Science & Global Security* 3.1–2 (1992), pp. 101–159. DOI: 10.1080/08929889208426380.

[202] D. Reilly et al. *Passive Nondestructive Assay of Nuclear Materials*. NUREG/CR-5550 LA-UR-90-732. Springfield, VA: Office of Nuclear Regulatory Research; Los Alamos National Lab, 1991. URL: https://cdn.lanl.gov/files/passive-nondestructive-assay-of-nuclear-materials_68e9a.pdf (visited on 03/03/2025).

[203] T. Sampson, G. Nelson, T. Kelley. *FRAM: A Versatile Code for Analyzing the Isotopic Composition of Plutonium from Gamma-Ray Pulse Height Spectra*. LA-11720-MS, DE90 00452. Los Alamos National Laboratory, 1989. URL: https://www.osti.gov/servlets/purl/5333902/ (visited on 03/25/2024).

[204] N. Syed et al. "Testing and verifying information barrier methodology on spent fuel assemblies". In: *Institute of Nuclear Materials Management (INMM) and European Safeguards Research and Development Association (ESARDA) Joint Annual Meeting*. 2021.

[205] S. J. Luke, D. E. Archer. "Gamma Attribute Measurements - Pu-300, Pu600, Pu900". In: *41th Annual Meeting of the Institute of Nuclear Materials Management (INMM)*. 2000. URL: https://www.osti.gov/servlets/purl/792530 (visited on 03/03/2025).

[206] M. Litz, C. Waits, J. Mullins. *Neutron-Activated Gamma-Emission: Technology Review:* ARL-TR-5871. Army Research Laboratory, 2012. URL: http://www.dtic.mil/docs/citations/ADA554870 (visited on 11/16/2022).

[207] S. Lesher et al. *The Black Sea Experiment*. Stanley Center for Peace and Security. 2024. URL: https://mynuclearlife.com/episode/the-black-sea-experiment-data-taking-and-legacy (visited on 09/23/2024).

[208] *Global Fissile Material Report 2022, Fifty Years of the Nuclear Non-Proliferation Treaty: Nuclear Weapons, Fissile Materials, and Nuclear Energy*. International Panel on Fissile Materials (IPFM), 2022. URL: https://fissilematerials.org/library/gfmr22.pdf (visited on 09/02/2024).

[209] A. Makhijani, H. Hu, and K. Yih, eds. *Nuclear Wastelands: A Global Guide to Nuclear Weapons Production and Its Health and Environmental Effects*. 1st ed. MIT Press, 2000.

[210] J. Hutchinson et al. *Analysis of the BERP Ball: an Alpha-Phase Plutonium Sphere*. LA-UR-09-03130. Los Alamos National Laboratory, 2009.

[211] S. Walston et al. *Benchmark Measurements of the BeRP Ball in Various Reflectors*. LLNL-TR-661297. Lawrence Livermore National Laboratory, 2014. URL: https://www.osti.gov/servlets/purl/1165823/ (visited on 03/01/2024).

[212] C. Percher. *LLNL Preliminary Design for BeRP Ball with Composite Polyethylene and Nickel Reflection*. LLNL-TR-652601. Lawrence Livermore National Laboratory, 2014. URL: https://www.osti.gov/biblio/1149051 (visited on 03/03/2025).

[213] J. Yan, A. Glaser. "Nuclear Warhead Verification: A Review of Attribute and Template Systems". In: *Science & Global Security* 23.3 (2015), pp. 157–170. DOI: 10.1080/08929882.2015.1087221.

[214] T. B. Cochran et al. *Nuclear Weapons Databook 3: U. S. Nuclear Warhead Facility Profiles*. Ballinger Publishing Company, 1984.

[215] *Actions Needed to Improve Integration of Production Modernization Programs and Projects*. GAO-24-106342. U.S. Government Accountability Office (GAO), 2024. URL: https://www.gao.gov/assets/gao-24-106342.pdf (visited on 01/28/2025).

[216] C. Hansen. *US Nuclear Weapons: The Secret History*. Orion Books, 1988.

[217] *W87-1 Modification Program*. National Nuclear Security Administration (NNSA), 2023. URL: https://www.energy.gov/sites/default/files/2023-11/W87-1_1123.pdf (visited on 03/03/2025).

[218] C. Hansen. *Swords of Armageddon, Version 2*. Chukelea Publications, 2007.

[219] C. Wallner et al. "Supernova produced and anthropogenic 244Pu in deep sea manganese encrustations". In: *New Astronomy Reviews* 48.1–4 (2004), pp. 145–150. DOI: 10.1016/j.newar.2003.11.020.

[220] L. Zetterström. *Oklo, A review and critical evaluation of literature*. TR-00-17. Laboratory for Isotope Geology, Swedish Museum of Natural History, 2000. URL: https://www.skb.com/publication/17620 (visited on 03/03/2025).

[221] S. Fetter et al. "Appendix A, Fissile Materials and Weapon Design". In: *Science & Global Security* 1.3–4 (1990), pp. 225–302. DOI: 10.1080/08929889008426334.

[222] R. J. Hamley et al. *Pit Lifetime*. JSR-06-335. The MITRE Corporation, 2007. URL: https://irp.fas.org/agency/dod/jason/pit.pdf (visited on 09/02/2024).

[223] *NNSA completes subcritical experiment at PULSE facility in Nevada*. National Nuclear Security Administration (NNSA). 2024. URL: https://www.energy.gov/nnsa/articles/nnsa-completes-subcritical-experiment-pulse-facility-nevada (visited on 09/02/2024).

[224] R. L. Garwin. *Reactor-Grade Plutonium Can be Used to Make Powerful and Reliable Nuclear Weapons: Separated plutonium in the fuel cycle must be protected as if it were nuclear weapons.* The Garwin Archive. 1998. URL: https://rlg.fas.org/980826-pu.htm (visited on 05/25/2023).

[225] J. E. Medalia. *U.S. Nuclear Weapon "Pit" Production Options for Congress*. R43406. Congressional Research Service, 2014.

[226] P. Podvig. *Interesting document about Soviet nuclear tests in 1953*. Russian Strategic Nuclear Forces. 2012. URL: https://russianforces.org/blog/2012/10/interesting_document_on_soviet.shtml (visited on 11/13/2024).

[227] *W38*. Weapons of Mass Destruction (WMD). n.d. URL: https://www.globalsecurity.org/wmd/systems/w38.htm (visited on 01/29/2025).

[228] B. Burnell. *Nuclear Weapons, a guide to British nuclear weapon projects*. 2023. URL: http://www.nuclear-weapons.info/vw.htm (visited on 02/07/2025).

[229] *Controllable Document N0 A / 1171*. 1964. URL: http://nuclear-weapons.info/images/tna-ab16-4675p63.jpg (visited on 02/07/2025).

[230] T. Cochran, C. E. Paine. *The Amount of Plutonium and Highly-Enriched Uranium Needed for Pure Fission Nuclear Weapons*. Natural Resources Defense Council, 1995. URL: https://www.ambienteparco.it/pdf/fissionweapons.pdf (visited on 02/02/2023).

[231] W. Stoll. *Plutonium in Hanau*. 1st ed. Fontaine-Verlag, 2014.

[232] *Neutron Source: Iran's Uranium Deuteride Neutron Initiator*. Institute for Science and International Security, 2019. URL: https://isis-online.org/isis-reports/detail/neutron-source-irans-uranium-deuteride-neutron-initiator-1/ (visited on 03/03/2025).

[233] S. C. Schmidt, J. N. Johnson, and S. C. Schmidt, eds. *Shock compression of condensed matter - 1989: Proceedings of the American Physical Society Topical Conference Held in Albuquerque, New Mexico, August 14-17, 1989*. Amsterdam: Elsevier Science Ltd, 1990.

[234] *Health and Environmental Consequences of Depleted Uranium Use in the U.S. Army: Technical Report*. U.S. Army Environmental Policy Institute, 1995.

[235] *Atomic Accidents*. The National Museum of Nuclear Science & History. 2014. URL: https://ahf.nuclearmuseum.org/ahf/history/atomic-accidents/ (visited on 12/07/2024).

[236] *Challenges Remain for Successful Implementation of DOE's Tritium Supply Decision*. GAO/RCED-00-24. U.S. Government Accountability Office (GAO), 2000. URL: https://www.gao.gov/assets/rced-00-24.pdf (visited on 10/30/2024).

[237] R. P. Johnson et al. "Production and Collection of He-3 and Other Valuable Isotopes using Mu*STAR". In: *9th International Particle Accelerator Conference*. 2018. DOI: 10.18429/JACOW-IPAC2018-MOPML054.

[238] *Memorandum for Members of the Nuclear Weapons Council, Nuclear Wapons Council Strategic Plan for Fiscal Years 2017-2042*. National Nuclear Security Administration (NNSA), 2016. URL: https://www.esd.whs.mil/Portals/54/Documents/FOID/Reading%20Room/NCB/17F1109_DOC_1_Memo_for_Members_of_the_Nuclear_Council.pdf (visited on 10/30/2024).

[239] *Savannah River Tritium Enterprise*. U.S. Department of Energy (DOE), Savannah River Site (SRS), n.d. URL: https://www.srs.gov/general/news/factsheets/srs_srte.pdf (visited on 10/30/2024).

[240] J. Von Las. "The Fog War". In: *Washington Examiner* (May 18, 2009).

[241] "Fogbank: Lost Knowledge Regained". In: *Nuclear Weapons Journal* 2 (2009).

[242] A. P. Weston-Dawkes. *Declassification of a Material in a Specified Weapon*. U.S. Department of Energy (DOE), Mar. 12, 2008. URL: https://sgp.fas.org/othergov/doe/decl/thorium.pdf (visited on 03/03/2025).

[243] *Plutonium Pit Production*. U.S. Department of Energy (DOE), National Nuclear Security Administration (NNSA). n.d. URL: https://www.energy.gov/nnsa/plutonium-pit-production (visited on 10/02/2024).

[244] S. Ji et al. *Using Physics Simulations to Find Targeting Strategies in Competitive Bowling*. 2022. arXiv: 2210.06753 [physics]. Pre-published.

[245] *Pantex Plant, Pit Dismantlement*. n.d. URL: https://www.reddit.com/r/nuclearweapons/comments/us5vk8/is_anyone_able_to_identify_this_weapon_pit_the/ (visited on 10/30/2024).

[246] *Vanunu's Photos of Dimona*. The US Campaign to Free Mordechai Vanunu. URL: https://www.vanunu.com/uscampaign/photos.html (visited on 03/17/2025).

[247] *Fiscal Year 2023, Stockpile Stewardship and Management Plan - Biennial Plan Summary*. U.S. Department of Energy (DOE), National Nuclear Security Administration (NNSA), 2023. URL: https://www.energy.gov/sites/default/files/2023-04/FY23%20SSMP_FINAL.pdf (visited on 11/05/2024).

[248] M. L. Adams. "NNSA Defense Programs Overview". National Nuclear Security Administration (NNSA) Transparency Demonstration. 2023.

[249] *Extending the Life, W78 Life-Extension Program*. Lawrence Livermore National Laboratory, 2012. URL: https://www.llnl.gov/sites/www/files/2020-05/W78-STR-Mar-12.pdf (visited on 10/03/2024).

[250] M. Kütt, A. Glaser. *IBX II Measurements*. 2019. URL: https://github.com/sgs-lab/ibxII-measurements (visited on 03/03/2025).

[251] A. B. Pohl, D. E. Archer. *133Ba as a gamma-ray surrogate source for 1kg HEU and 10g 239Pu and 252Cf as a Neutron Surrogate for Pu*. UCRL-TR-202871. Lawrence Livermore National Laboratory, 2004. URL: https://www.osti.gov/servlets/purl/15009812/ (visited on 10/24/2024).

[252] L. I. Rudin, S. Osher, E. Fatemi. "Nonlinear total variation based noise removal algorithms". In: *Physica D* 60.1–4 (1992), pp. 259–268. DOI: 10.1016/0167-2789(92)90242-F.

[253] P. Virtanen et al. "SciPy 1.0: fundamental algorithms for scientific computing in Python". In: *Nature Methods* 17.3 (2020), pp. 261–272. DOI: 10.1038/s41592-019-0686-2.

[254] M. Tarokh. "Solving a Class of Nonlinear Inverse Problems Using a Feedback Control Approach". In: *Mathematical Problems in Engineering* 2017 (2017), pp. 1–11. DOI: 10.1155/2017/6843614.

[255] R. E. Korf. "Depth-first iterative-deepening: An optimal admissible tree search". In: *Artificial intelligence* 27.1 (1985), pp. 97–109. DOI: 10.1016/0004-3702(85)90084-0.

[256] W. Wilson et al. "Sources: A code for calculating (alpha, n), spontaneous fission, and delayed neutron sources and spectra". In: *Progress in Nuclear Energy* 51.4–5 (2009), pp. 608–613. DOI: 10.1016/j.pnucene.2008.11.007.

[257] J. Kang et al. "Spent Fuel Standard as a Baseline for Proliferation Resistance in Excess Plutonium Disposition Options". In: *Journal of Nuclear Science and Technology* 37.8 (2000), pp. 691–696. DOI: 10.1080/18811248.2000.9714945.

[258] *Plutonium Pit Production*. National Nuclear Security Administration (NNSA), 2019. URL: https://www.energy.gov/nnsa/articles/plutonium-pit-production-mission (visited on 03/03/2025).

[259] *A Complete Guide to Californium*. Frontier Technology Corp. n.d. URL: https://frontier-cf252.com/blog/complete-guide-californium/ (visited on 10/27/2024).

[260] M. Kütt. "Simulation of Neutron Multiplicity Measurements using Geant4, Open Source Software for Nuclear Arms Control". TU Darmstadt, 2016. URL: https://tuprints.ulb.tu-darmstadt.de/5621/ (visited on 03/03/2025).

[261] Z. Qi et al. "The Advancement of Neutron-Shielding Materials for the Transportation and Storage of Spent Nuclear Fuel". In: *Materials* 15.9 (2022), p. 3255. DOI: 10.3390/ma15093255.

[262] F. Rosenblatt. "The Perceptron: A Probabilistic Model for Information Storage and Organization in the Brain." In: *Psychological Review* 65.6 (1958), pp. 386–408. DOI: 10.1037/h0042519.

[263] M. D. DeChaine, M. A. Feltus. "Nuclear Fuel Management Optimization Using Genetic Algorithms". In: *Nuclear Technology* 111.1 (1995), pp. 109–114. DOI: 10.13182/NT95-A35149.

[264] J. E. Yang et al. "Application of genetic algorithm for reliability allocation in nuclear power plants". In: *Reliability Engineering & System Safety* 65.3 (1999), pp. 229–238. DOI: 10.1016/S0951-8320(98)00103-3.

[265] C. M. N. A. Pereira, R. Schirru, A. S. Martinez. "Genetic Algorithms Applied to Nuclear Reactor Design Optimization". In: *Fuzzy Systems and Soft Computing in Nuclear Engineering*. Ed. by D. Ruan. Red. by J. Kacprzyk. Vol. 38. Physica-Verlag HD, 2000, pp. 315–334.

[266] C. M. Pereira, C. M. Lapa. "Coarse-grained parallel genetic algorithm applied to a nuclear reactor core design optimization problem". In: *Annals of Nuclear Energy* 30.5 (2003), pp. 555–565. DOI: 10.1016/S0306-4549(02)00106-8.

[267] I. Rechenberg. *Evolutionsstrategie, Optimierung technischer Systeme nach Prinzipien der biologischen Evolution*. Friedrich Frommann Verlag, 1975.

[268] H. P. Schwefel. *Numerische Optimierung von Computer-Modellen mittels der Evolutionsstrategie*. Birkhäuser Basel, 1977.

[269] J. H. Holland. *Adaptation in Natural and Artificial Systems*. MIT Press, 2010.

[270] M. Gendreau and J. Y. Potvin, eds. *Handbook of Metaheuristics*. Springer International Publishing, 2019.

[271] S. Forrest. "Genetic Algorithms". In: *ACM Computing Surveys* 28.1 (1996), pp. 77–80. DOI: 10.1145/234313.234350.

[272] K. De Jong. "Learning with Genetic Algorithms: An Overview". In: *Machine Learning* 3.2–3 (1988), pp. 121–138. DOI: 10.1007/BF00113894.

[273] G. E. Liepins, M. R. Hilliard. "Genetic algorithms: Foundations and applications". In: *Annals of Operations Research* 21.1 (1989), pp. 31–57. DOI: 10.1007/BF02022092.

[274] D. Whitley. "A genetic algorithm tutorial". In: *Statistics and Computing* 4.2 (1994), pp. 65–85. DOI: 10.1007/BF00175354.

[275] D. Simon. *Evolutionary Optimization Algorithms*. 1st ed. Wiley, 2013.

[276] O. Kramer. *Genetic Algorithm Essentials*. Springer International Publishing, 2017.

[277] J. K. Polack et al. "A Modular Approach to Trusted System Design for Arms Control Treaty Verification". In: *61th Annual Meeting of the Institute of Nuclear Materials Management (INMM)*. 2020. URL: https://www.osti.gov/servlets/purl/1807446 (visited on 03/28/2025).

[278] M. Kütt, A. Glaser. "Vintage Verification, For Trusted Radiation Measurements and a World Free of Nuclear Weapons". 34th Chaos Communication Congress (34c3). 2017. URL: https://www.princeton.edu/~aglaser/IT075-34c3-Vintage-Verification.pdf (visited on 03/29/2025).

[279] M. Kütt et al. "Authenticating Nuclear Warheads With High Confidence". In: *55th Annual Meeting of the Institute for Nuclear Materials Management*. 2014. URL: http://www.princeton.edu/~aglaser/PU081-Kuett-Glaser-2014.pdf (visited on 03/03/2025).

[280] S. Fetter. "Verifying Nuclear Disarmament". In: *Nuclear Weapons, The Road to Zero*. Ed. by J. Rotblat. 1st ed. Routledge, 1998.